

Computational Fluid Dynamics Analysis of the Combustion Process for the TJT-  
3000 Micro Jet Turbine Engine

by

Marcus A. Harden

Submitted in Partial Fulfillment of the Requirements for the Degree of

Master of Science in Engineering

in the Mechanical Engineering Program

YOUNGSTOWN STATE UNIVERSITY

December, 2021

Computational Fluid Dynamic Analysis of the TJT-3000 Micro Turbine Engine

Marcus A. Harden

I hereby release this thesis to the public. I understand that this thesis will be made available from the OhioLINK ETD Center and the Maag Library Circulation Desk for public access. I also authorize the University or other individuals to make copies of this thesis as needed for scholarly research.

Signature:

\_\_\_\_\_  
*Marcus A. Harden, Student* Date

Approvals:

\_\_\_\_\_  
*Stefan Moldovan, Thesis Advisor* Date

\_\_\_\_\_  
*Hazel Marie, Committee Member* Date

\_\_\_\_\_  
*Kyosung Choo, Committee Member* Date

\_\_\_\_\_  
Dr. Salvatore A. Sanders, Dean of Graduate Studies Date

## **ABSTRACT**

The TJT-3000 on the campus of Youngstown State University is like one of many micro turbine engines used in UAV and other large RC aircraft. This project aims to analyze and propose improvements to the combustion chamber of micro turbine engines using the TJT-3000 as a baseline. These improvements would include an overall increase in the combustion chamber without heavily increasing the overall temperature reaching the turbine inlet. To analyze these criteria, the feasibility of using a handheld Creaform scanner for the purpose of scanning small turbine engine components is tested. The scanner was found to be viable, but a finer resolution was desirable as the scanned data from these scanned components would be refined and turned in to CFD capable models. The created CFD models in this project required a considerable amount of post processing to prepare. With a baseline model to compare to experimental data of the turbine engine, hypothesized geometric changes were applied to the turbine engine where the impact of each change would be considered and summarized.

Based on the CFD models and literature review it was found that the geometric changes of the combustion chamber should be focused on improving the flow rate through the engine without extinguishing the produced flame while as much of the initial relatively cold flow coming from the compressor should be directed towards the back of the combustion chamber to cool the turbine inlet. Restricting the amount of flow through the combustion chamber leads to a higher pressure drop and an increase in combustion efficiency at the cost of unmanageable chamber wall temperatures, while geometry modifications that force flow through the inner most sections of the combustion chamber first will increase the cooling of the turbine stator inlet with a manageable increase in combustion chamber wall temperatures.

# TABLE OF CONTENTS

ABSTRACT.....	iii
TABLE OF CONTENTS.....	iv
LIST OF FIGURES .....	vi
LIST OF TABLES .....	xi
NOMENCLATURE .....	xii
CHAPTER 1 INTRODUCTION & PROBLEM IDENTIFICATION.....	1
1. Introduction.....	1
1.1. Combustion Chamber Efficiency .....	2
1.2. Project Description.....	4
1.3. Turbojet Engines.....	5
1.4. The Brayton Cycle.....	7
1.5. The TJT-3000 Microturbine Engine .....	7
1.6. Engine Experimental Run & Results .....	11
2. Modeling .....	13
2.1. Engine Disassembly.....	13
2.2. Engine Scanning .....	17
2.3. Engine Modeling.....	22
3. COMPUTATIONAL MODEL.....	37
3.1. Meshing.....	39
3.2. Simulation Setup.....	44
3.3. Modeling, Boundary, & Initial Conditions .....	47
4. Results .....	51
4.1. Simulation Results – Base Model .....	53
4.2. Simulation Results – Compared Models.....	62
4.3. Additional Observations – Turbulent Kinetic Energy .....	87
4.4. Model Comparison – Overview & Analytical Results .....	90

5. Conclusions & Comments .....	95
References.....	97
APPENDIX.....	101

## LIST OF FIGURES

Figure 1-1: The Brayton Cycle .....	7
Figure 1-2: TJT-3000 Intake .....	8
Figure 1-3: TJT-3000 Compressor & Diffuser .....	9
Figure 1-4: TJT-3000 Combustion Chamber .....	9
Figure 1-5: TJT-3000 Turbine .....	10
Figure 1-6: Nozzle Fluid Domain Area .....	10
Figure 1-7: TJT-3000 Exhaust .....	11
Figure 1-8: TJT-3000 Experimental Setup .....	12
Figure 2-1: Start of Engine Disassembly .....	14
Figure 2-2: Removal of Sensors .....	15
Figure 2-3: Exposed Compressor and Diffuser .....	15
Figure 2-4: Turbine Removal .....	16
Figure 2-5: Disassembled Engine in Line .....	16
Figure 2-6: Disassembled Engine with Removed Compressor .....	17
Figure 2-7: Creaform HANDYSCAN 300 .....	18
Figure 2-8: Displayed and Scanned Turbine Rotor. ....	19
Figure 2-9: Cleaned Turbine Rotor Model .....	21
Figure 2-10: Import of Turbine Rotor with Separated Points .....	21
Figure 2-11: Two Blades of Turbine Rotor. ....	22
Figure 2-12: Plane Slice of Turbine Rotor Blade and Resulting Intersection Sketch. .....	24
Figure 2-13: Smoothed and Sliced Sketch of Turbine Blade Section .....	25
Figure 2-14: Smoothed Surface Construction Frame .....	26
Figure 2-15: Turbine Rotor with Split and Solid Body Contour. ....	27
Figure 2-16: Modeled Compressor Rotor and Stator. ....	28
Figure 2-17: Modeled Turbine Rotor and Stator. ....	29
Figure 2-18: Fully Modeled TJT-3000 Micro Turbine Engine.....	29

Figure 2-19: Section View of Fully Modeled TJT-3000 Micro Turbine Engine.....	30
Figure 2-20: Simplified Fully Modeled TJT-3000 Micro Turbine Engine.....	31
Figure 2-21: Simplified Section View of Fully Modeled TJT-3000 Micro Turbine Engine. ....	31
Figure 2-22: Simplification of Combustion Chamber .....	32
Figure 2-23: Combustion Chamber Three-body Domain .....	33
Figure 2-24: Combustion Chamber Fluid Domain Breakdown .....	34
Figure 2-25: Original Combustion Chamber .....	35
Figure 2-26: Combustion Chamber Geometry Change 1.....	36
Figure 2-27: Combustion Chamber Geometry Change 2.....	37
Figure 3-1: Inner Combustion Chamber .....	38
Figure 3-2: Outer Combustion Chamber .....	39
Figure 3-3: Overall Engine Mesh .....	41
Figure 3-4: Section View of Engine.....	41
Figure 3-5: Polyhexcore Elements .....	42
Figure 3-6: PDF Table for Non-Premixed Combustion.....	46
Figure 3-7: Boundary Conditions on Simplified Model.....	50
Figure 3-8: Boundary Conditions Related to Full Model .....	50
Figure 4-1: Cross Section Planes for Results.....	52
Figure 4-2: Engine Velocity Contour.....	53
Figure 4-3: Accelerated Flow Offshoot.....	54
Figure 4-4: Flow Rotation in to Vaporizing Tube.....	55
Figure 4-5: Side Profile Temperature Contour .....	56
Figure 4-6: Side Profile Oxygen Contour .....	56
Figure 4-7: Head on Temperature Contour .....	57
Figure 4-8: Head on Oxygen Contour .....	57
Figure 4-9: Combustion Chamber Pressure Contour.....	59
Figure 4-10: High Pressure Close-up .....	59
Figure 4-11: Velocity Vector & Temperature Overlay .....	60

Figure 4-12: Velocity Vector & Temperature Overlay Close-Up .....	61
Figure 4-13: Velocity Vector & Temperature Overlay Close-Up .....	61
Figure 4-14: Velocity Vector & Pressure Overlay Close-Up.....	62
Figure 4-15: Velocity Contour Model Comparison: (a) baseline model, (b) larger flowpath model, (c) closed flowpath model .....	64
Figure 4-16: Larger Flowpath Model – Redirected Flow.....	66
Figure 4-17: Larger Flowpath Model – Vorticity .....	66
Figure 4-18: Larger Flowpath Model – Less Directional Flow.....	67
Figure 4-19: Closed Flowpath Model – Redirected Flow .....	68
Figure 4-20: Closed Flowpath Model – Flow Divergence .....	68
Figure 4-21: Closed Flowpath Model – More Directional Flow.....	69
Figure 4-22: Pressure Contour Model Comparison: (a) baseline model, (b) larger flowpath model, (c) closed flowpath model .....	70
Figure 4-23: Larger Flowpath Model – Pressure Zone.....	71
Figure 4-24: Larger Flowpath Model – Lower Pressure Inner Combustion Chamber .....	72
Figure 4-25: Closed Flowpath Model – High Pressure Zone.....	73
Figure 4-26: Closed Flowpath Model – High Pressure Inner Combustion Chamber .....	73
Figure 4-27: Temperature Contour Model Comparison – Side Profile: (a) baseline model, (b) larger flowpath model, (c) closed flowpath model .....	75
Figure 4-28: Oxygen Mass Fraction Contour Model Comparison – Side Profile: (a) baseline model, (b) larger flowpath model, (c) closed flowpath model.....	76
Figure 4-29: Temperature Contour Model Comparison – Front Profile: (a) baseline model, (b) larger flowpath model, (c) closed flowpath model .....	77
Figure 4-30: Oxygen Mass Fraction Contour Model Comparison – Front Profile: (a) baseline model, (b) larger flowpath model, (c) closed flowpath model.....	78
Figure 4-31: Temperature Contour Penetrating Flow.....	79
Figure 4-32: Oxygen Contour Penetrating Flow.....	79
Figure 4-33: Distributed Temperatures.....	81
Figure 4-34: Open Flowpath Oxygen Distribution.....	81



Figure 4-35: Closed Flowpath Model – Temperature Concentration .....	82
Figure 4-36: Closed Flowpath Model – Temperature Concentration.....	82
Figure 4-37: Temperature and Velocity Vector Overlay Comparison: (a) baseline model, (b) larger flowpath model, (c) closed flowpath model .....	83
Figure 4-38: Open Flowpath Model – Circulation Temperatures .....	84
Figure 4-39: Closed Flowpath Model – Cold Flow Circulation .....	85
Figure 4-40: Pressure and Velocity Vector Overlay Comparison: (a) baseline model, (b) larger flowpath model, (c) closed flowpath model.....	86
Figure 4-41: Larger Flowpath Model – Flow Interference .....	87
Figure 4-42: Turbulent Kinetic Energy Comparison: (a) baseline model, (b) larger flowpath model, (c) closed flowpath model .....	88
Figure 4-43: Turbulent Kinetic Energy Comparison Front View: (a) baseline model, (b) larger flowpath model, (c) closed flowpath model.....	90
Figure 5-1: Combustion Chamber in Fluid Domain Cavity .....	101
Figure 5-2: Engine Inlet Scan.....	102
Figure 5-3: Engine Inlet Model .....	102
Figure 5-4: Compressor Stator Scan .....	103
Figure 5-5: Compressor Stator Fins Import .....	103
Figure 5-6: Compressor Stator Fin Import.....	104
Figure 5-7: Compressor Stator Model .....	104
Figure 5-8: Turbine Stator Scan.....	105
Figure 5-9: Turbine Stator Fin Import .....	105
Figure 5-10: Engine Shroud Scan.....	106
Figure 5-11: Engine Nozzle Scan.....	106
Figure 5-12: Turbine Rotor Blades Import.....	107
Figure 5-13: Turbine Rotor Blade - SolidWorks Boundary Surface.....	107
Figure 5-14: Fluent Meshing Spark Domain.....	108
Figure 5-15: Non-Premixed Combustion – Boundary Mass Fraction.....	109
Figure 5-16: Non-Premixed Combustion – Chemistry.....	109
Figure 5-17: Non-Premixed Combustion – Table Parameters .....	110

Figure 5-18: Pressure Contour Limits .....	110
Figure 5-19: Temperature Contour Limits .....	110
Figure 5-20: Velocity Contour Limits.....	111
Figure 5-21: Viscous Model Parameters .....	111
Figure 5-22: Closed Flowpath CFD Model Residuals .....	112
Figure 5-23: Kerosene Fuel Concentration Contour – Baseline Model .....	112
Figure 5-24: Kerosene Fuel Concentration Contour – Open Flowpath Model .....	113
Figure 5-25: Kerosene Fuel Concentration Contour – Closed Flowpath Model .....	113
Figure 5-26: Baseline CFD Model Fuel Concentration Pathlines .....	114
Figure 5-27: Baseline Model Velocity Pathlines.....	114
Figure 5-28: Closed Flowpath CFD Model Fuel Concentration Pathlines .....	115
Figure 5-29: Closed Flowpath CFD Model Velocity Pathlines .....	115
Figure 5-30: RPM vs Fuel Flow Rate - (Campbell, Latimer, & Scholes, 2006).....	116
Figure 5-31: Expected Pressure to RPM - (Krampf, 1992).....	116
Figure 5-32: BMT 120 KS Experimental Run Values - (Large & Pesyridis, 2019) .....	117
Figure 5-33: BMT 120 KS Data Collection Points - (Large & Pesyridis, 2019) .....	117

## LIST OF TABLES

Table 1-1: TJT-3000 Engine Characteristics .....	11
Table 1-2: New Make Experimental Results .....	13
Table 2-1: Handyscan 300 vs Handyscan 700 Specifications .....	18
Table 2-2: Model Geometry Changes .....	36
Table 3-1: Local Sizing Table .....	40
Table 3-2: Overall Mesh Criteria .....	42
Table 3-3: Mesh Convergence Criteria .....	43
Table 3-4: Modeling Parameters.....	45
Table 3-5: Non-Premixed Combustion Setup .....	46
Table 3-6: PDF Table Characteristics .....	47
Table 3-7: Outlet Condition Findings .....	48
Table 3-8: Combustion Model Boundary Conditions.....	49
Table 3-9: Model Solution Methods .....	51
Table 4-1: Model Results – Velocity.....	64
Table 4-2: Model Results – Pressure .....	70
Table 4-3: Model Results – Temperature .....	74
Table 4-4: Model Results – Turbulent Kinetic Energy .....	88
Table 4-5: TJT-3000 Engine Characteristics.....	92
Table 4-6: New Make Experimental Results vs Baseline Model .....	92
Table 4-7: Combustion Efficiency .....	93

## NOMENCLATURE

<u>Variable</u>	<u>Meaning</u>
$W_{in}$	Work In
$W_{out}$	Work Out
$Q_{in}$	Heat In
$Q_{out}$	Heat Out
$T_{avg}$	Average Temperature
$T_{max}$	Maximum Combustion Temperature
$T_{min}$	Minimum Temperature
$T_{out}$	Outlet Temperature
$y^+$	Non-Dimensional Wall Distance
$N$	Number of Elements
$u_*$	Friction Velocity
$y$	Element Distance to Wall
$\nu$	Kinematic Viscosity
$\eta_{th,Brayton}$	Thermal Efficiency
$k$	Specific Heat Ratio
$r_p$	Pressure Ratio

# CHAPTER 1

## INTRODUCTION & PROBLEM IDENTIFICATION

### 1. INTRODUCTION

The focus of this project is a CFD analysis of a TJT-3000 micro turbojet engine. To talk about a micro turbojet engine, one must first understand a turbine engine. As stated by Collins, A turbine engine utilizes a moving fluid to convert kinetic energy to mechanical (Collins, 2020). The engine does this in a series of steps explained in Section 1.5

The history of the turbine engine is something disputed in many avenues. Due to contributions from several countries as well as the separation between land and air-based turbine engines. Development of the gas turbine engine can be found as far back as the early 1900's. Some of these early engines being built by Holzwarth, who developed a series of models between 1908 and 1933 (Soares, 2013).

A turbine engine can take on many forms, the most basic being a turbojet. More advanced versions of the turbine engine have a turbojet as their core component and add or modify that base characteristic to fit another need and/or increase efficiency in some other aspect. The turbofan for example, is what you find on the wing of commercial airliners. This turbofan has a turbo-jet core whose primary purpose is to drive a large fan. This large fan is placed in front of the core, and a shroud is built around this entire system. Due to the size of the fan, there is some space between the engine core and the shroud. The air driven by the fan, that passes in this gap is called bypass air. This version of the engine is much more efficient for longer flights and is the dominant form of the turbine engine today.

The engine that is of focus for this research is a miniature version of what lies in the core of the turbo-fan engine, a miniature version of a turbojet. The fundamentals of a turbojet is seen in section 1.2.

This turbojet micro-turbine engine is not to be confused with a stationary micro turbine. These are a relatively new technology being used for stationary power generation applications. For small scale power generation, they offer multiple benefits regarding their ability to maintain efficiencies of over 80% with a limited number of moving parts, small size, and lower emissions according to Capehart. These types of engines are used to have additional power in the case of an outage

as well as a backup source of power to alleviate any power peaks or dips. (Capehart, 2016).

These types of turbine engines are more akin to a turbo-shaft engine. These engines are not focused on thrust like a turbojet or turbo-fan engine. Instead, these are focused solely on driving a shaft for power generation. These are also used in helicopters to drive the spinning blades and specialize in areas where thrust is not the goal.

Over the years, several improvements have been made consistently to raise the efficiency of turbine engines. The focus of this project is on the increase in engine efficiency via changes in the combustion chamber geometry without modification to the other components.

### 1.1. Combustion Chamber Efficiency

During the research phase of this project, focus was directed mostly at the previous modeling of other micro turbine engines. Initially a search for any analysis of the TJT-3000 was sought after but after extensive search there appears to be no published research regarding this model. However, as stated in the manufacturer manual, (Williams, 2016) the TJT-3000 is heavily inspired by the KJ-66 micro turbine engine. This engine was very popular in the previous years before the TJT-3000 was built and is still used today for the enthusiast RC aircraft scene. As the KJ-66 was a much more widely used micro turbine engine, there was previous research done and due to the similarities between the designs of the engines, it allowed for some insight.

This problem also persisted when it came to available Computer Aided Design (CAD) of said engines. There are no available CAD models of the TJT-3000 whereas full CAD models of the KJ-66 microturbine engine are plenty. Although when modeling the TJT-3000 the methods and techniques for modeling other micro turbine engines could be utilized. Some of the more robust studies would utilize stationary scanners for the small engine components, but the use of a handheld scanner was proven to be viable when it was used (Valigi, Logozzo, & Affatato, 2017).

Of the CFD models that focused on the KJ-66 engine, here were a few that included fully coupled CFD models, meaning they would model the entirety of the engine. The focus of this project is specifically the combustion chamber, but this fully coupled simulation proved to be a great baseline for boundary conditions where the model for this project would not encompass. The performance of the KJ-66 engine when running at 80,000 RPM was found to have a thrust of 270.95N. Temperatures

reaching up to 2300K, with an average of 950K. 8% pressure loss and a mass flow rate of 0.14 kg/s. (Wang, et al., 2020).

When the viewpoint is expanded beyond nearly identical engines, the number of comparable models increases. There were several CFD models of other micro turbine engines which were of use. An analysis of the BMT 120 KS gas turbine was found. This is a larger, more powerful micro turbine engine, but still fell under the category of a micro turbine engine as classified by the NATO and UK government (NATO, 2021). The application for this engine fell outside of the scope of this project, as the recommendation was to turn the engine in to a turbofan engine with the BMT 120 KS as the core for better performance. Although, the analysis of the engine proved to be useful as they had an in-depth analysis of the pressure along the engine both numerically and via experimentation. At the same boundary conditions as the model run for this project the turbine inlet pressure was found to be 174Kpa (Large & Pesyridis, 2019)

To improve the combustion chamber geometry specifically, a similar analysis was done on the same type of annular combustion chamber that the KJ-66 uses. This research looked at the geometric constraints of the annular combustion chamber and optimized them. Unfortunately for a majority of these constraints to be implemented, other aspects of the engine beyond just the combustion chamber would have to be changed as well. For this project, the constraints of which were capable of being done only to the combustion chamber were considered. This would include the holes of the combustion chamber where cold flow was meant to enter, as well as the vaporizing tubes of which fuel would be injected. (Habibi, 2019).

To compare the efficiency of the micro turbine engine, an analysis was done regarding the overall, thermal, propulsive efficiency. The study found there is a propulsive efficiency increase when mass flow rate is increased in the engine. This effect carried over to overall efficiency as the flow rate increased, the maximum velocity of the engine approached Mach 1 but to a lesser extent. (Chauhan & Wessley, 2019).

On a similar basis as Chauhan & Wessley, research done to predict the performance of advanced power cycles stated that in order to find the optimal turbine inlet temperature cooling flow augmentation is required through an increase in the amount of cold flow running through the engine to aid in cooling and the development of materials able to resist the increased heat within the engine. Due to the area of focus for this project being specifically the combustion chamber the focus will be on improving the flow through the engine. For this scenario as an uncooled engine, the most critical impact on efficiency is the thermodynamic considerations.

(Chiesa, Consonni, Lozza, & Macchi, 2015). Improvement of flow running through the combustion chamber will likely lead to an improved thermal efficiency but will require more expensive materials (Aminov, 2018).

For experimental comparison, previous students at Youngstown State University had run the TJT-3000 when newly manufactured and collected data including the temperature at four locations of the engine. These areas included the inlet, compressor, combustion chamber, and exhaust. (Campbell, Latimer, & Scholes, 2006) These temperatures would serve as great comparison values for the CFD analysis in addition to the previously mentioned KJ-66 CFD modeling research.

## 1.2. Project Description

Micro turbine engines like the TJT-3000 are often used in applications such as remote-controlled airplanes and unmanned aerial vehicles. While the down scaling of gas turbine technology negatively impacts the heat and combustion processes, these engines have multiple benefits including their compact size and low weight per unit power. One of the specified engines resides on Youngstown State's University's campus and is the engine to be analyzed. As the combustion process is one of the negatively affected processes, the combustion chamber of this engine is the primary focus for this project. Improvements to the combustion chamber of a micro turbine engine look to fall under the NASA Aeronautics Research Mission Directorate (ARMD), as improvements to these engines will lead to improvements in UAV applications.

The goals of this project include:

- Reverse Engineering & Building a 3D CAD Model of the Existing Engine.
- Optimize Combustion Chamber to Allow for Higher Flame Temperatures inside the Combustion Chamber while Maintaining Lower Temperatures at the Turbine Inlet.
- Improve the Cooling of the Engine to Withstand the New Temperatures.
- Create a Detailed Computational Fluid Dynamics (CFD) Model to Analyze the Original and New Operating Parameters.

To verify the CFD results, an experimental setup must be utilized and built to measure the original operating parameters. The engine is currently instrumented with thermocouples and pressure transducers to measure the temperature and pressure both before and after the combustion chamber. In addition, a load cell is used to measure the thrust from the engine. Once an accurate model has been made and verified, it can then be improved upon. Since detailed CAD models of the engine do not exist, part of the project includes taking detailed measurements of the



internal components of the engine. This will be accomplished by using 3D scanning tools that are available in the manufacturing laboratory in the Mechanical Engineering Department. To complete the analysis of the engine, ANSYS Software is to be utilized.

The outcomes of this project include:

- Completed CAD Models of all Components of the Engine
- Completed CFD Model of the Engine Combustion Chamber.
- Applied Improvements to the Simulated Combustion Chamber and Operating Conditions of the Engine.

The programs required for this project include:

- 3D CAD (SolidWorks) Modeling.
- CFD (ANSYS Fluent).
- 3D Scanning (Creaform VXElements).

### 1.3. Turbojet Engines

The basic sections of the turbine engine can be described by five major sections.

- Intake
- Compressor
- Combustion Chamber
- Turbine
- Exhaust

Beyond these five primary sections, there are variants to the basic turbine engine that expand on this basic principle to adapt to different conditions or uses. The most common and likely to be the type of engine that comes to mind when thinking of turbine engines is the Turbofan. This is the engine that is commonly used on commercial airliners and what you'd see looking out the window on your next flight. This engine takes the five major sections and adds a large fan to the front, now making the traditional turbine engine (a turbojet) the "core" that powers the large fan. This additional fan that is many times larger in diameter than the turbine engine now forces air down two paths, one path feeding the core of the engine and the other passing over the core creating what is called "bypass air". The micro turbine engine is not a turbofan, it is a miniature version of the traditional turbojet. The differences between these distinctions of turbine engine will be further elaborated on as the sections of the turbine engine are described.

As the project in question is focused on the latter of the two types of engine, Figure I-1 is elaborated on to further describe these sections. Each component is described in the following paragraphs. (Benson & Shaw, 2021)

**Intake:** The intake directs air from the free stream towards the compressor of the engine. This intake begins the compression process as it directs this air.

- The air taken in from the free stream is directed towards the compressor
- The type of turbojet will determine the type of intake the engine has, for subsonic turbojet engines like the TJT-3000 the intake is rounded.

**Compressor:** The compressor of the engine compresses the air it's receiving from the inlet, the compressor is often set up with stages of rotors and stators that will press the flow in stages.

- Two main types of compressors, Axial and Centrifugal.
- Centrifugal compressors are now often used on smaller turbojet engines.
- Axial compressors can be stacked to give a greater factor of pressure increase, while centrifugal compressors are much more difficult to stack and require a larger circumference causing more drag. Centrifugal is better for small simple engines. Axial is better for high performance larger engines.

**Diffuser:** A critical component between the compressor and the combustion chamber. Used for designs with radial compressors due to its function being to turn the high velocity radial flow into high velocity axial flow. Doing this transformation causes a large amount of energy to be lost, making the diffuser design critical

**Combustion Chamber:** Where the compressed air is forced in and mixed with fuel. The mixture ignites, temperature increases, and the airflow develops high energy. The lining of this chamber is often ceramic materials to withstand the 2700°+ temperatures. There are several types of combustion chambers including Can, Cannular, and Annular. Most micro turbine engines use an Annular type combustion chamber.

**Turbine:** This now high energy airflow coming from the combustion chamber forces the turbine blades to rotate. The blades in the turbine are linked to the shaft which drives the compressor. Because of this connection as long as there is flow running through the engine at a sufficient speed and fuel is being supplied to the combustion chamber to maintain combustion, the engine will be self-sustaining.

**Exhaust:** The exhaust, usually encompassed with a convergent nozzle is the part that produces the thrust for the engine.

- The combination of the cold bypass air and the hot air leaving the turbine create an exhaust which propels the engine forward.
- Sometimes a mixer accompanies the exhaust in order to reduce the noise of the engine by combining bypass air and combustion gases.

#### 1.4. The Brayton Cycle

To describe the thermodynamic process of a micro turbine jet engine, the Brayton Cycle is used. This cycle can be described in four steps as follows (Hall, 2021)

1. Air Moves into the Compressor ( $W_{in}$ ) in an Adiabatic (No Transfer of Heat), Isentropic (Constant Entropy, Adiabatic and Reversible) Process (Pressure & Temperature Increase, Volume Decrease)
2. The Flow Enters the Combustion Chamber, where the fuel is ignited in an Isobaric Process (Volume Increase, Entropy Increase, and Temperature Reaches its Peak) where heat is added ( $Q_{in}$ ),
3. Air is forced out of the Combustion Chamber Through the Turbine ( $W_{out}$ ) in an Isentropic Expansion Process (Pressure Decreases to atm, Volume Increases, Temperature Decreases)
4. Air is Brought to the Intake in an Isobaric Process and the Cycle Repeats ( $Q_{out}$ ).

A visual representation of this cycle can be seen in Figure 1-1.

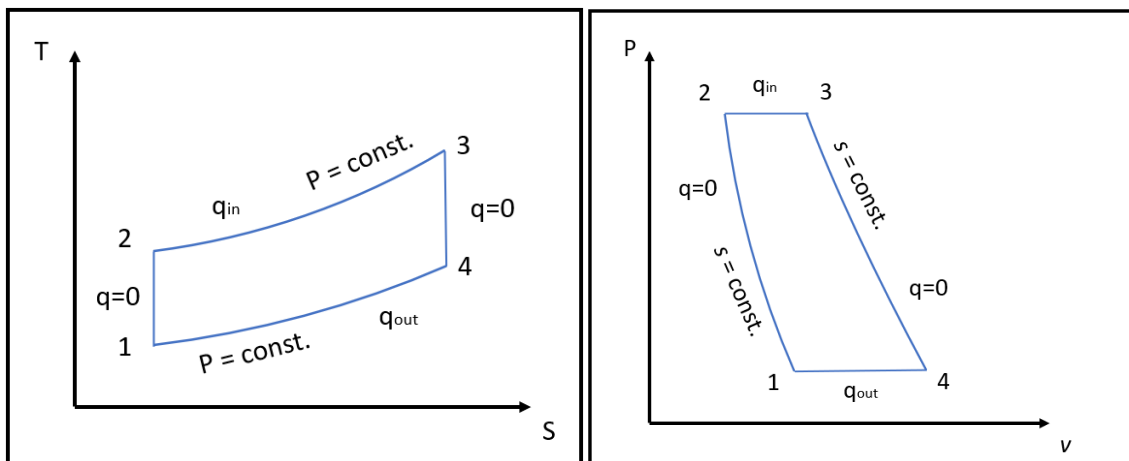


Figure 1-1: The Brayton Cycle

#### 1.5. The TJT-3000 Microturbine Engine

As mentioned in the project description, the engine being used for this analysis is the TJT-3000 micro turbine engine. This engine is a design created by Turbojet Technologies and Artes Jet Microturbines, inspired by the KJ-66 micro turbine

engine developed by Jesus Artes, Kurt Schreckling and Thomas Kamps. To describe the engine, its components can be broken up into the same five sections described before. Each section described will have a corresponding figure with the highlighted area in question for the TJT-3000 Micro Turbine Engine.

**Intake:** The TJT-3000 uses a rounded inlet, typical in subsonic engines.

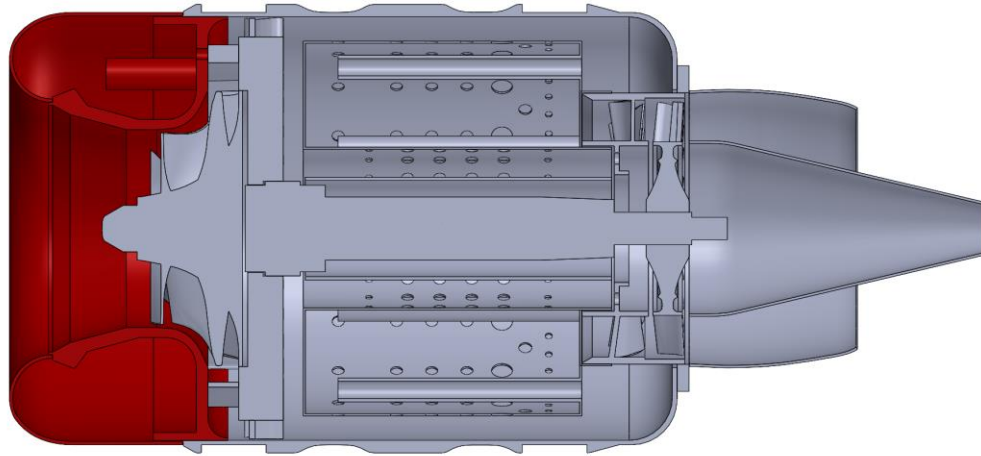


Figure 1-2: TJT-3000 Intake

**Compressor:** A single centrifugal compressor is used, typical in micro turbine engines for their compact nature with a total count of 16 blades.

**Diffuser:** The diffuser of the TJT-3000 Microturbine engine could also be considered the stator of the centrifugal compressor. This is the compressor stator of the compression stage which houses the compressor rotor. The flow is forced through a series of stationary vanes that change the direction of flow from its heavily rotational direction and to a more axial direction. In this process the flow slows down as it enters the combustion chamber.

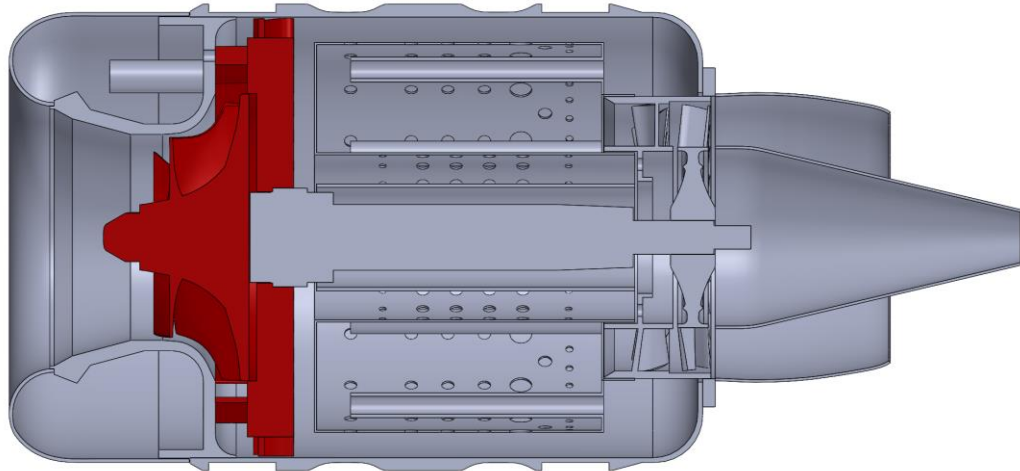


Figure 1-3: TJT-3000 Compressor & Diffuser

**Combustion Chamber:** As with most micro turbine engines. The combustion chamber used is Annular. This annular combustion chamber is setup with three different sized holes to adjust how much flow is entering the combustion chamber. The size of the holes in descending order are 16.702 mm, 9.567 mm, and 5.665 mm.

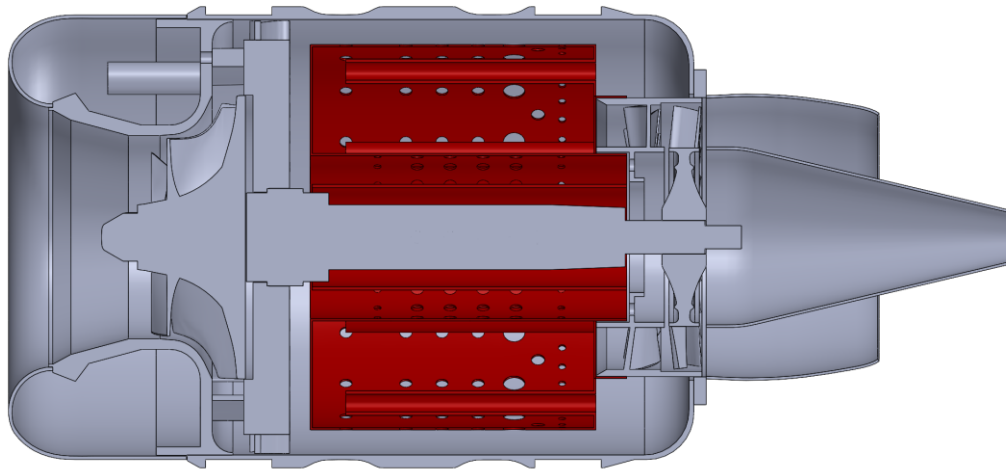


Figure 1-4: TJT-3000 Combustion Chamber

**Turbine:** Turbine includes a single rotor and single stator stage. The rotor captures the energy from the combustion to turn the compressor while the stator redirects the flow once again towards the exhaust.

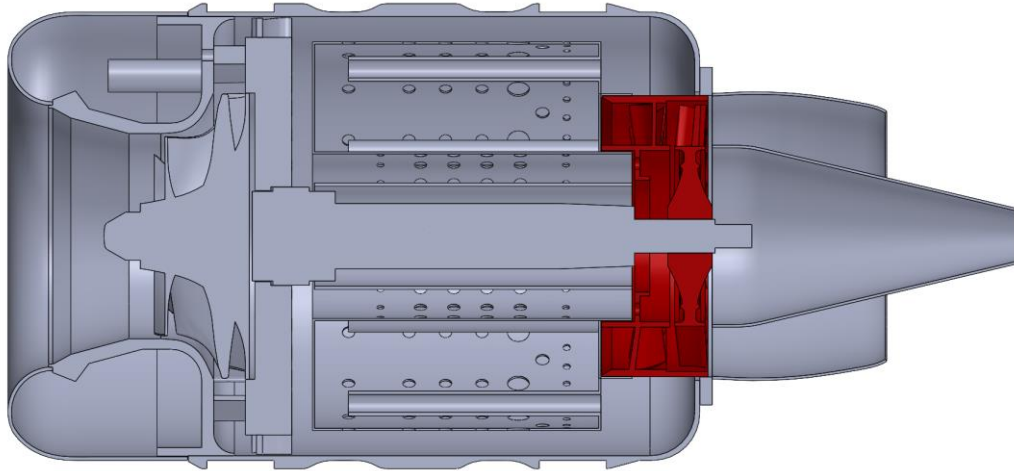


Figure 1-5: TJT-3000 Turbine

**Exhaust:** The exhaust for the TJT-3000 is divergent when leaving the turbine outlet but turns convergent when reaching the rear of the nozzle. A chart showing the area of the fluid domain for the nozzle can be seen in Figure 1-6

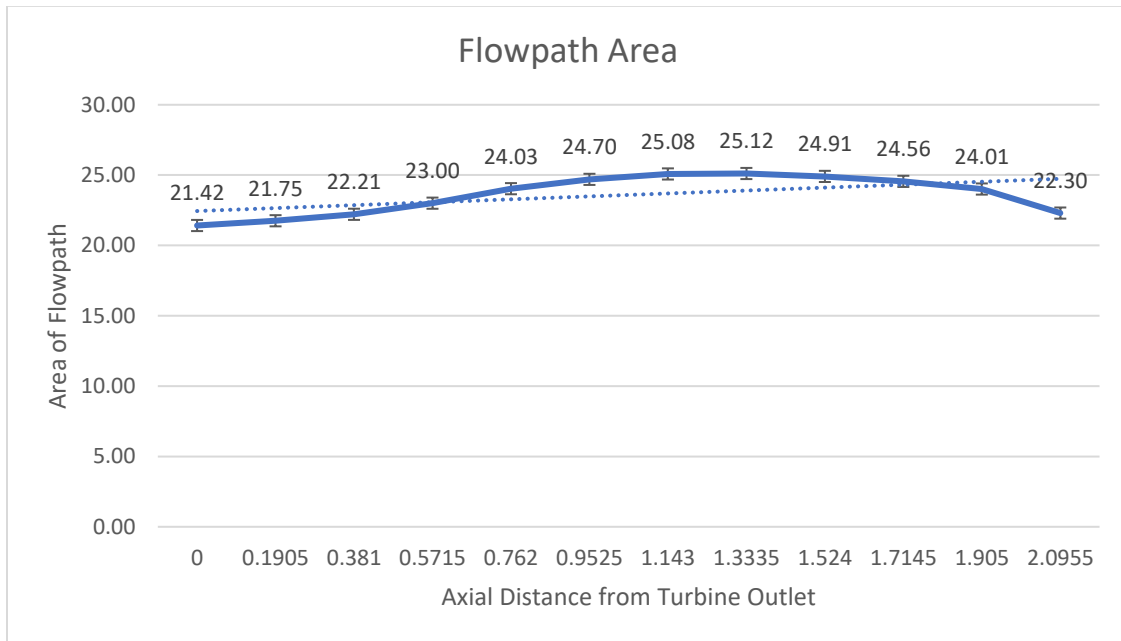


Figure 1-6: Nozzle Fluid Domain Area

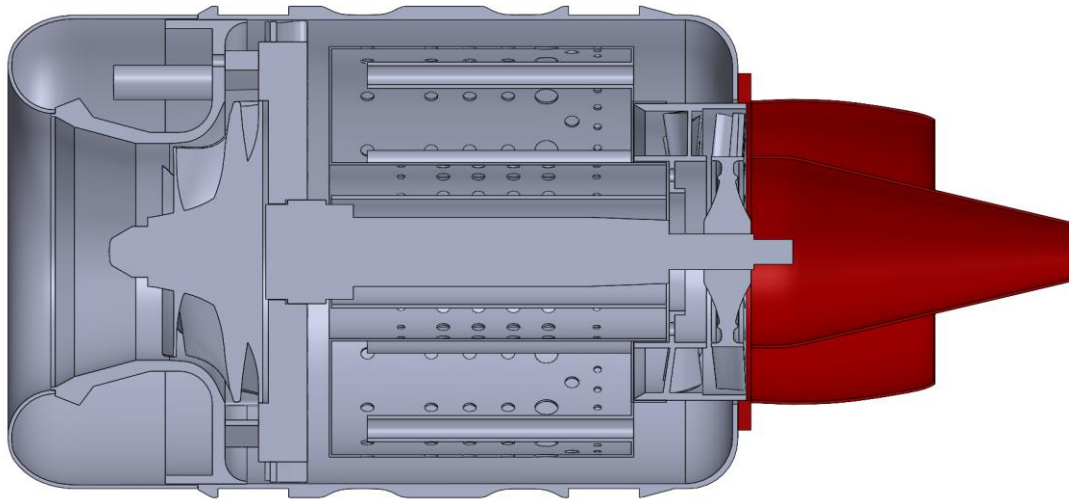


Figure 1-7: TJT-3000 Exhaust

### 1.6. Engine Experimental Run & Results

Prior to the disassembly of the engine, an experiment had to be run in order to have results to compare to. However, due to the condition of the experimental setup at the time the amount of information that could be collected was limited to the exhaust temperature of the turbine, but this experiment proved to be insightful in the operation of the engine in terms of the required fuel for startup, the use of kerosene fuel, potential rotations per minute of the compressor as well as the temperatures expected from the engine. The details of the engine as received from the manual (Williams, 2016) can be seen in Table 1-1.

Table 1-1: TJT-3000 Engine Characteristics

Engine Characteristics	
Maximum Thrust	12.5 kg
Maximum Sustainable Shaft Speed	126,000 RPM
Idle Shaft Speed	33,000 RPM
Max EGT	640°C
Fuel	Kerosene, Jet A1
Fuel Consumption	0.35 (L/min)
Weight	1.65 Kg

The experimental setup of this engine has the engine sitting on a rail to allow the measurement of thrust. As the engine propels itself forward a protruding piece will press in to a strain bridge and allow for this measurement. Multiple thermocouples are inserted in do ports of the engine of which will record data back to a controller

provided with the TJT-3000 engine. The location of these thermocouples includes the exhaust as well as the combustion chamber temperature. An image of the experimental setup can be seen in Figure 1-8.

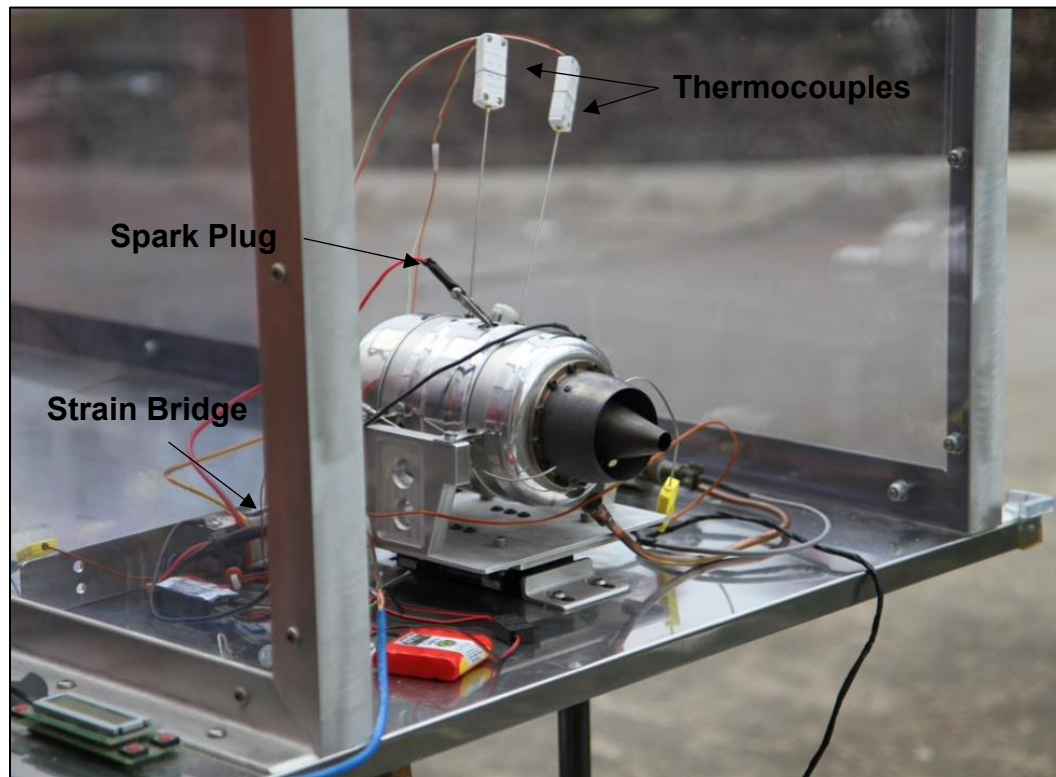


Figure 1-8: TJT-3000 Experimental Setup

While the main fuel of the engine is kerosene, this engine uses propane in order to start the ignition. During the experiment phase, the compressor is brought up manually to a steady speed of around 6000 RPM of which then propane is pushed into the system and ignited using a spark plug seen in Figure 1-8. Once this ignition has started, the propane is closed off and the kerosene is then pumped in to the engine through the vaporizing tubes. The manual spinning of the compressor is continued until the system is self-sustaining and the kerosene fuel is being properly evaporated and consumed. At this point, the engine could then be manipulated and data could be collected.

For additional information, the experimental results of previous Youngstown State University students were used. The students that collected this data (Campbell, Latimer, & Scholes, 2006) had tested this engine at new make condition and collected the appropriate data. The temperature data they had collected can be found in Table 1-2 of which will be used as a comparison in the results section of this project.



Table 1-2: New Make Experimental Results

Experimental Results	
Exhaust Temperature	904.8 K
Compressor Temperature	375.7 K
Combustion Temperature	1541.9471 K

## 2. MODELING

The CAD modeling of the turbine engine is the first crucial step to get accurate results in the CFD analysis. The CAD modeling of the TJT-3000 was done in multiple steps. First of which being the near complete disassembly of the engine. Once the engine was disassembled, each component of the engine was scanned using a HandySCAN 300 from Creaform. After the components were scanned, surface data was imported into SolidWorks. Due to the resolution of the scans, the surface data had to then be smoothed out, and made into a solid part. Each component was then assembled, allowing for a fluid domain to be created and mesh generated.

### 2.1. Engine Disassembly

Engine disassembly started soon after an initial test run to confirm the engine's operation. The process was done while documenting each step-in order to allow for a more streamlined disassembly in the future.

The disassembly process starts exactly as one would expect it to, with the full engine. The engine had to be separated from its testing setup where it was initially housed. An image of the engine in this testing setup can be seen in image (a) of Figure 2-1. Once the engine was separated from the experimental setup the external components could begin to be removed. This would start with the front shroud of the engine which kept the fuel ports and rpm sensor hidden. The engine with this shroud section removed can be seen in image (b) of Figure 2-1.

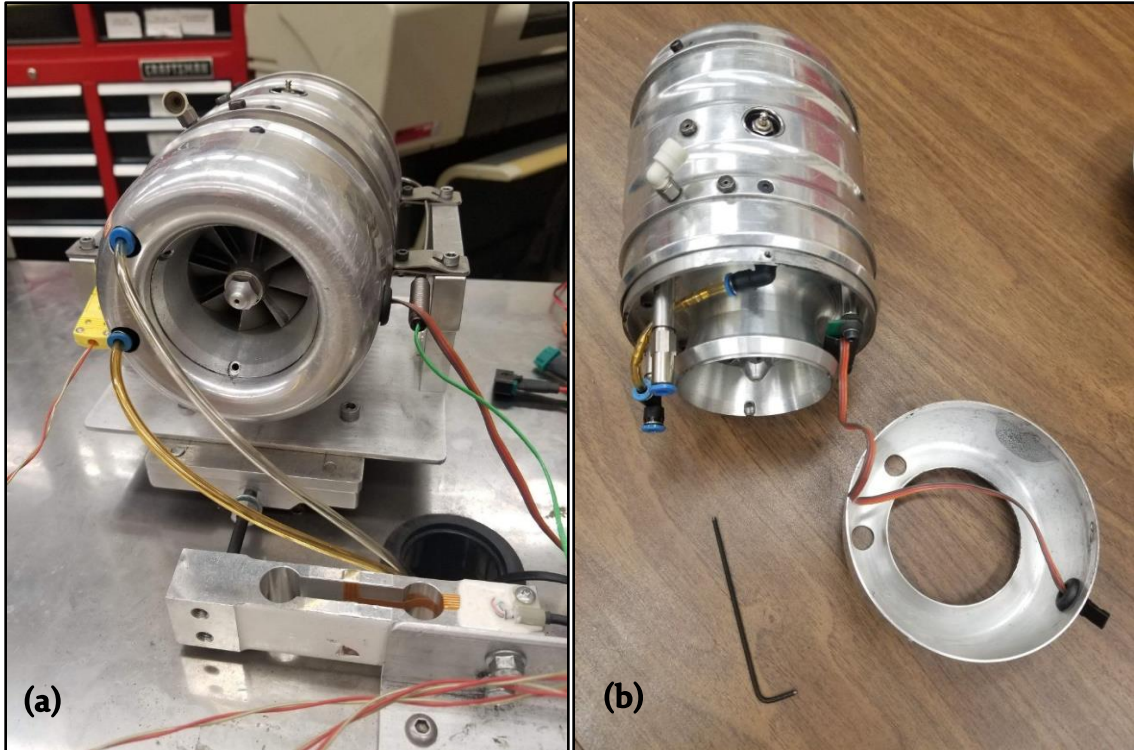


Figure 2-1: Start of Engine Disassembly

The disassembly continues with the removal of the fuel lines, RPM sensor, glow plug and several external screws that were holding the shroud to the internal components of the engine. This can be seen in images (a) and (b) of Figure 2-2. Following this step, the inlet of the engine could be removed from the remaining assembly. This left the compressor and diffuser of the micro turbine engine exposed. This can be seen in images (a) and (b) of Figure 2-3. Moving to the rear of the engine, the nozzle as well as the turbine rotor and stator could be removed. This can be seen in images (g) and (h) of Figure 2-4. Once these items had been removed, most of the components holding the combustion chamber inside of the shroud had been removed. This allowed the separation of the shaft, combustion chamber and shroud of the engine which resulted in the disassembled state of the engine that would allow for scanning of its individual components. This final state can be seen in Figure 2-5 and Figure 2-6.



Figure 2-2: Removal of Sensors



Figure 2-3: Exposed Compressor and Diffuser

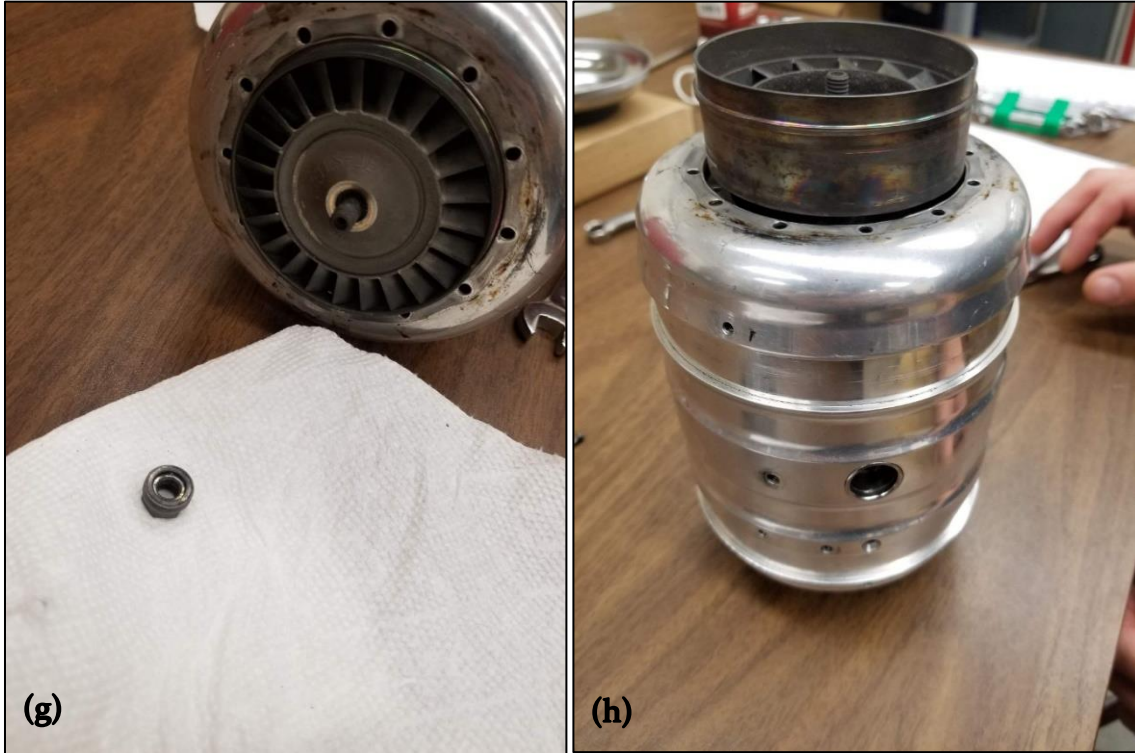


Figure 2-4: Turbine Removal



Figure 2-5: Disassembled Engine in Line



Figure 2-6: Disassembled Engine with Removed Compressor

## 2.2. Engine Scanning

Engine scanning was done using the HandySCAN 300 (Figure 2-7), as mentioned before. This scanner is a handheld scanner from Creaform that is designed to collect point data from an object and insert it into a 3D workspace. As the engine was in a disassembled state from the previous section, the critical geometries of the engine were able to be scanned using this software and hardware. The scanning process of the turbine rotor for the micro turbine engine will be shown as an example of the scanning process.

To get an accurate measurement of the internal components of the turbine engine. 3D scanning was determined to be the most efficient avenue. As described by Valigi, Logozzo and Affatato these devices, specifically confocal laser scanning excel at producing high resolution images. These devices are based off triangulation utilizing an initial calibration of a known pattern before being used to measure the surface in question. These scanners have been used to measure surface wear with great accuracy. Using a HandySCAN 700 a complete image of wear distribution along a blade could be generated but the accuracy of the scan heavily depends on the procedure of the researcher on the computer based clean up of the scanned component (Valigi, Logozzo, & Affatato, 2017). As the model from this study is a more accurate version, this has to be considered when scanning the features of the turbine engine. As seen in Table 2-1 (CREAFORM, 2021), the main consideration will be the resolution and accuracy of the scanners. Due to the limited accuracy of the Handyscan 300, more cleanup will be required which is elaborated on in Section 2.3.

For this reason, the methodology in the scanning of the micro turbine engine is critical moving forward. Details being lost during the scanning process is an important concern



Figure 2-7: Creaform HANDYSCAN 300

Table 2-1: Handyscan 300 vs Handyscan 700 Specifications

Category	Handyscan 300	Handyscan 700
<b>Measurement Rate</b>	205,000 measurements/s	480,000 measurements/s
<b>Scanning Area</b>	225x250 mm	270x250 mm
<b>Laser Class</b>	2M	
<b>Resolution</b>	0.100 mm	0.050 mm
<b>Accuracy</b>	Up to 0.040 mm	Up to 0.030 mm
<b>Volumetric Accuracy</b>	0.020 mm + 0.100 mm/m	0.020 mm + 0.060 mm/m

### **Scanning Setup:**

The setup for scanning the components of the engine was relatively straight forward but had to be done in a very particular way. The Creaform software interacts with the HandySCAN 300 by virtue of collecting point data in reference to a series of physical datums the scanner uses to calibrate. These physical datums are typically stuck to the component that needs to be scanned for larger components, but since the object in question is a micro turbine engine, sticking these datums to the part was not advantageous. Instead, the datums were stuck to a surface of which the components would be placed on. This would scan the surface with the datums but also scan the component sitting on it. An example of a component sitting on this board used for scanning can be seen in Figure 2-8 (a).

The operator would then prepare the HandySCAN 300 for scanning by first calibrating the scanner with a separate series of physical datums on a predefined board pattern. Once this calibration had been done the scanning was ready to be started.

### **Scanning Data:**

Once the scanning had started the scan would take several minutes depending on the operator and the level of detail needed. As this process was to scan complex geometries of a turbine engine for CFD analysis the finest resolution possible was selected. For the HandySCAN 300 this was limited to 0.02 mm. The scanner would pick up point data while the operator would continue to project the scanner on to the part and the board with the physical datums attached. An image of what the collection of this point data looked like on the Creaform software for the micro turbine engine turbine rotor can be seen in Figure 2-8 (b).

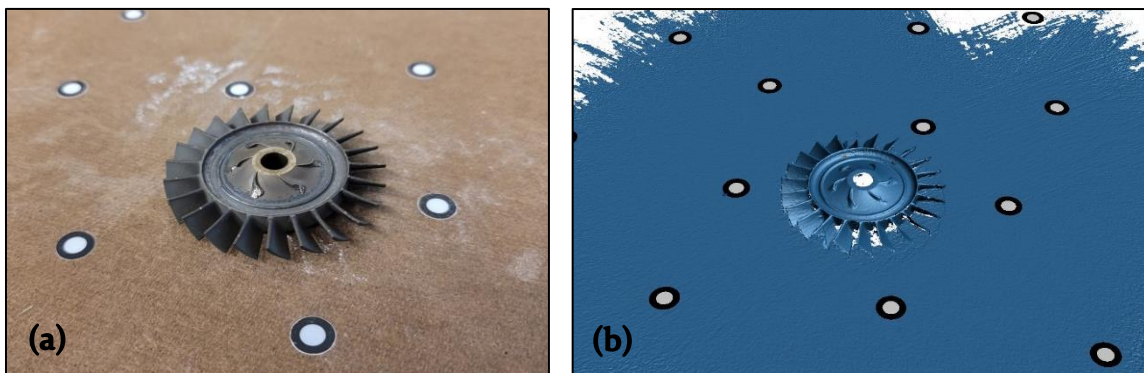


Figure 2-8: Displayed and Scanned Turbine Rotor.

Once a scan had been completed, there was still additional measurements to be done. As the part could not be moved at all during the scanning process, the other side of the component needed a separate scan. For every part that needed to be scanned, several scans were required. Some for the front and back of the part, followed by some additional scans for detail that was not captured by the initial scans.

### **Post Processing:**

The post processing of these scans is where the fully scanned component would come together. As each of the scans created in the previous section are incomplete images of the object, they need to be combined to create the full detail scanned component. This is done within the Creaform software, where a reference point is selected on each of the scans that are to be combined. These reference points are to be located at the same location on the other scanned component. The more reference points added to match up the orientation of the part the closer the software can get to lining up the individual scans for a complete model. This process is done two scans at a time until all of the scans are combined in to one cohesive model.

Due to the method of scanning, particularly the datums being placed on to a board for the part to sit on, the board is also scanned in with the part as one would expect. This unwanted scanned data can be removed with the same software, where a clipping plane can be created by selecting three datums. Since every datum is on the board for scanning this allows for a plane that is ideal for removing the board from the scan. Once the unwanted scanned data from the board is removed as well as the combined scans are processed, the scan is completed.

When reviewing the finished scans, a problem became apparent. The resolution of the HandySCAN 300 was not fine enough to extrapolate a clean profile on the smaller components of the micro turbine engine. During cleanup of the model which included voids as well as scattered data points captured by light reflection from the metallic components there were several parts of the scan that had to be fixed before they would be of any use in a CFD model. Some of the problem areas on the surface of the model turned out for this same model can be seen in Figure 2-9.





Figure 2-9: Cleaned Turbine Rotor Model

In order to remedy this issue, the models would have to be imported into a 3D CAD software for further post processing. The CAD software of choice for this project was SolidWorks. Initially, attempts were made to import entire components into SolidWorks but due to the limitations of the imported model this would result in a host of surface data points too far separated to extrapolate any real data from. The result of this issue can be seen in Figure 2-10. To get a more detailed model there had to be a smaller section exported from the Creaform software. This was done for any of the curved geometries of the engine. Small sections of the highest quality area of the scan were selected and exported into SolidWorks. The scan of two blades of the turbine rotor were selected to move forward, these blades can be seen in Figure 2-11. As the scan for this much more defined section was more detailed, the required post processing could continue.

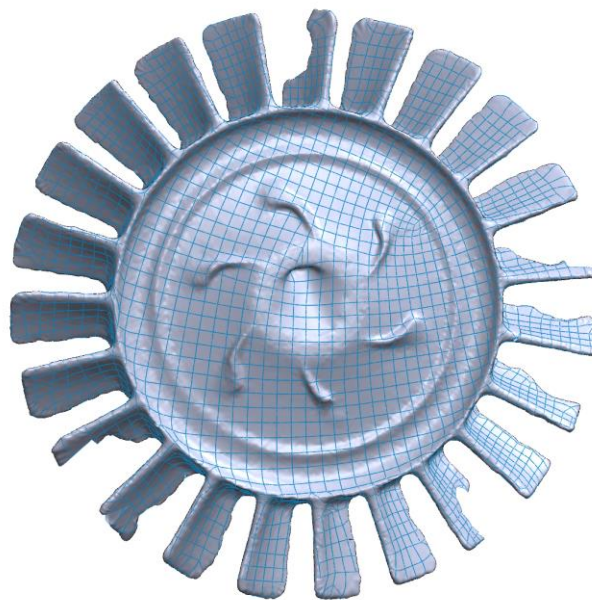


Figure 2-10: Import of Turbine Rotor with Separated Points

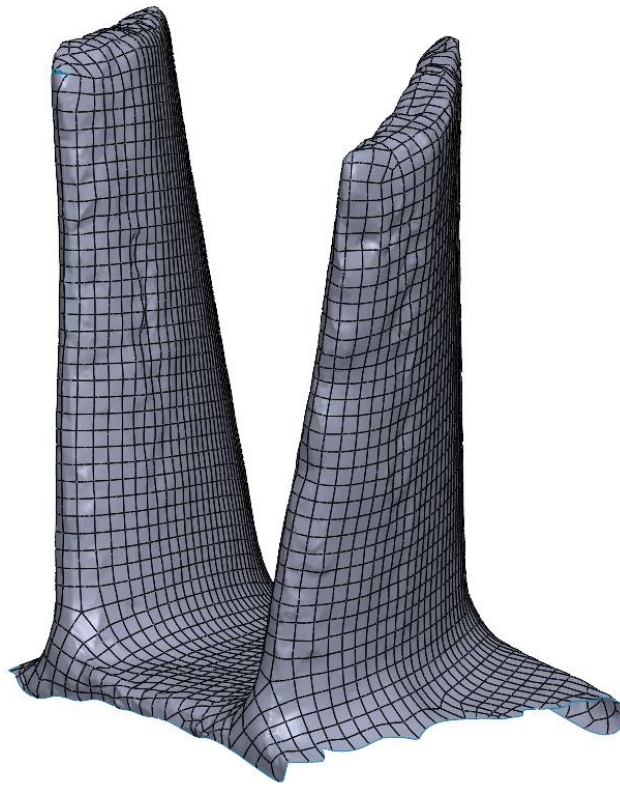


Figure 2-11: Two Blades of Turbine Rotor.

### 2.3. Engine Modeling

As the models were imported into SolidWorks, they still required a fair amount of work. As can easily be seen in the previous Figure 2-10, the imported model still has several imperfections on the surface, where inconsistencies in the several high and low points are visible. This is not present in the actual part in question and had to be smoothed out. Fortunately, SolidWorks did a very good job at importing the point data as a series of tiny surfaces that could be used to generate a much smoother models. This was done with the combination of several commands in SolidWorks. The most important commands for this process were Slice, 3D Sketch, Spline, Surface Knit, and Boundary Surface. A quick overview can be seen below, each of these commands will be explained in more detail later in the section.

**Slice:** The slice command would create multiple planes in a selected direction and distance starting from a reference plane. This would be used to “slice” the modeled blades to create framework for a cleaned-up model.

**3D Sketch:** 3D sketch is exactly as it sounds, instead of creating a sketch on each individual plane, it would allow for a sketch to be created and interact with each of these planes in a 3D space.

**Spline:** The spline would be used to connect multiple points while holding a polynomial curve instead of a straight line as a basic “line” command would.

**Surface Knit:** This command would take several surfaces that are intersected and combine them in to one “knitted” surface. The surfaces in question still held their individual characteristics but the surface knit allowed for a secondary command with which if these surfaces were properly aligned, one would create a solid part. Without this command the connected boundaries would be hollow inside and have no value in a CFD program.

**Boundary Surface:** Boundary surface would create a surface out of a 3D boundary

### **Modeling Process:**

To begin, a surface was created by selecting three points of data from the imported surface. The points of intersection anywhere on the surface of the component could be selected. Three points at the flat top portion of the turbine rotor blade were selected as a starting plane. Once this starting plane was selected, it could be used to generate many projected planes through the part using the slice command. The model with this series of planes running through the part can be seen in Figure 2-12 (a). For this reason, the orientation of the planes was critical. Once the planes were propagated through the part, a sketch could be created on each of these planes. With each of these sketches the intersection command could be used between these planes as well as. A figure showing what this process looked like can be seen in Figure 2-12 (b).

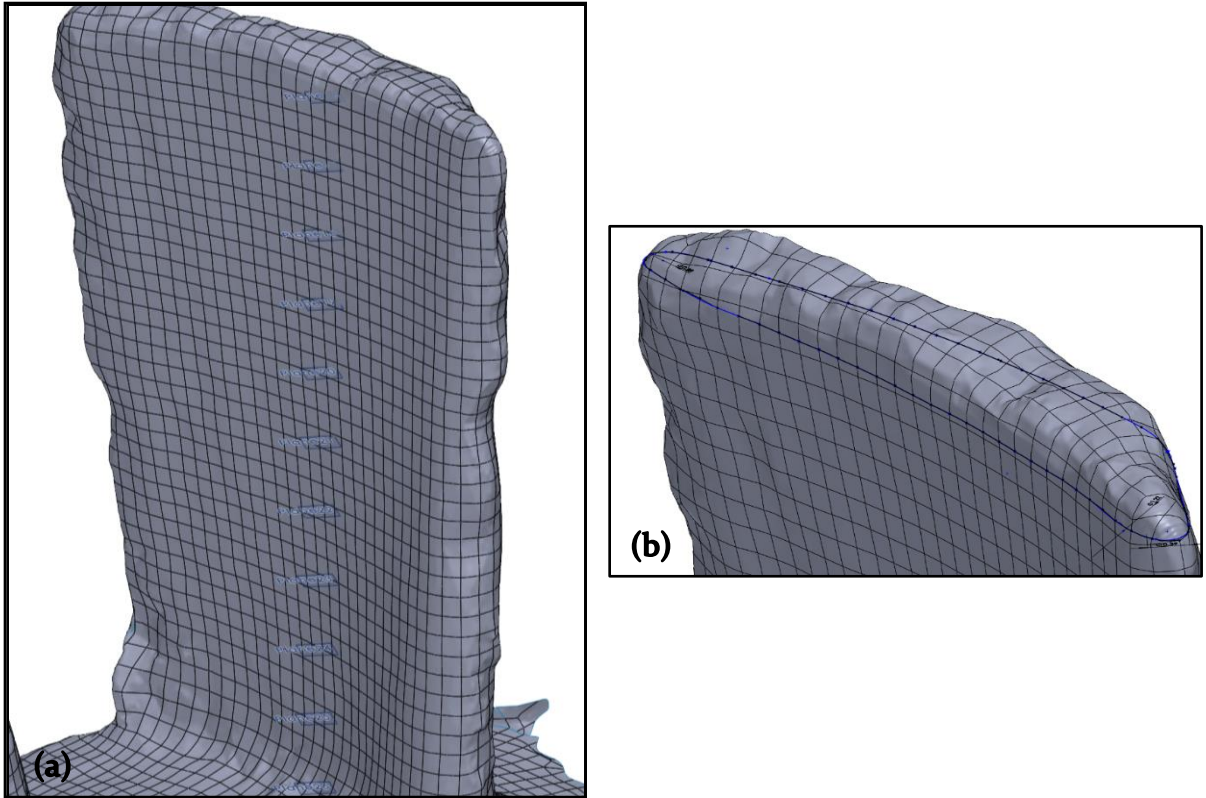


Figure 2-12: Plane Slice of Turbine Rotor Blade and Resulting Intersection Sketch.

Once these planes were created and the sketches had been made from the intersection points, the inconsistent nature of the surface was even more apparent. To achieve a smooth model for CFD this would not be viable. To remedy this, new sketches had to be made on every sketch plane using the original as a guide. To select which point was more accurate to the real-world geometry, measurements were taken at critical locations on the blades. The overall height and thickness at several locations on the blade were recorded along the entire length of the blade. Using these dimensional measurements, a smoothed sketch was created that would closely follow the blade geometry. A view of this newly created sketch can be seen in Figure 2-13.

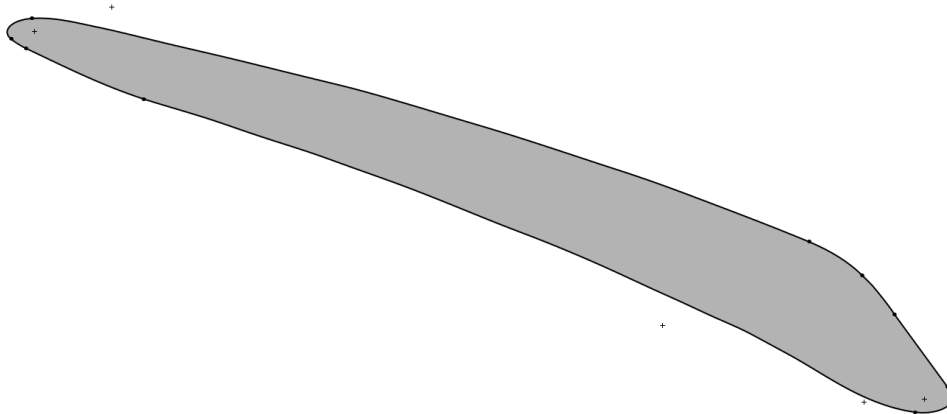


Figure 2-13: Smoothed and Sliced Sketch of Turbine Blade Section

The above process was repeated for every sketch through the part which would vary depending on the blade type, for the centrifugal compressor it would require upwards of 20 sketches to get a satisfactory model. The turbine rotor blade that was used as the modeling example took a total of 14 sketches. Once these sketches were created, the use of SolidWorks 3D sketch mode was required. A new 3D sketch was made that would utilize these previously created sketches. A spline connecting the sketches at designated locations would be created along the entire length of the blade. These selected locations would usually include the widest, longest, thinnest portions of the sketch as well as some additional points for good measure. The connected splines between these sketches can be seen in Figure 2-14 (a) & (b). The second image of Figure 2-14 was included to emphasize the curvature of the blade that needs to be captured using this method. Depending on the number of included sketches this feature could be lost. This is the primary reason for the disparity in the number of surfaces required to capture the different blade geometries. 14 in the case of the turbine rotor, upwards of 20 for the compressor blade.

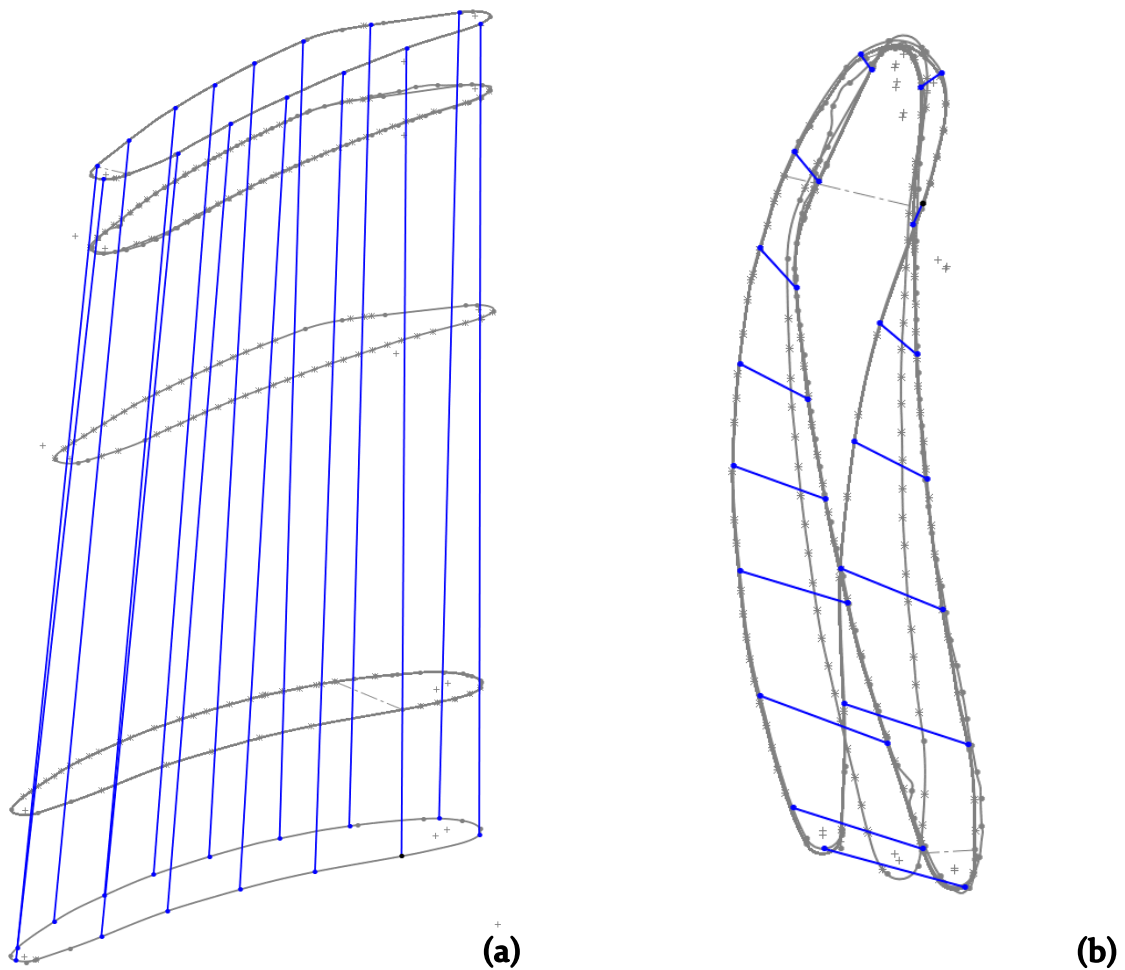


Figure 2-14: Smoothed Surface Construction Frame

What the process up till now had done was effectively make a “frame” for a critical feature in SolidWorks to create the smooth geometry. The feature Boundary Surface would take each of the smoothed sketches and follow the created splines in the 3D sketch to create one continuous surface for the entire blade. After this feature, the part still had several issues depending on how the splines were selected and the sketches were generated. Some of the surfaces would have a split along the length of the blade, these would have to be refined for use in CFD. While these splits in the surface could not be entirely removed, they could be manipulated by modifying the sketch to ensure they were not in a location that would severely inhibit the meshing process in a later section. The smoothed surface created from this process can be seen in Figure 2-15 (a).

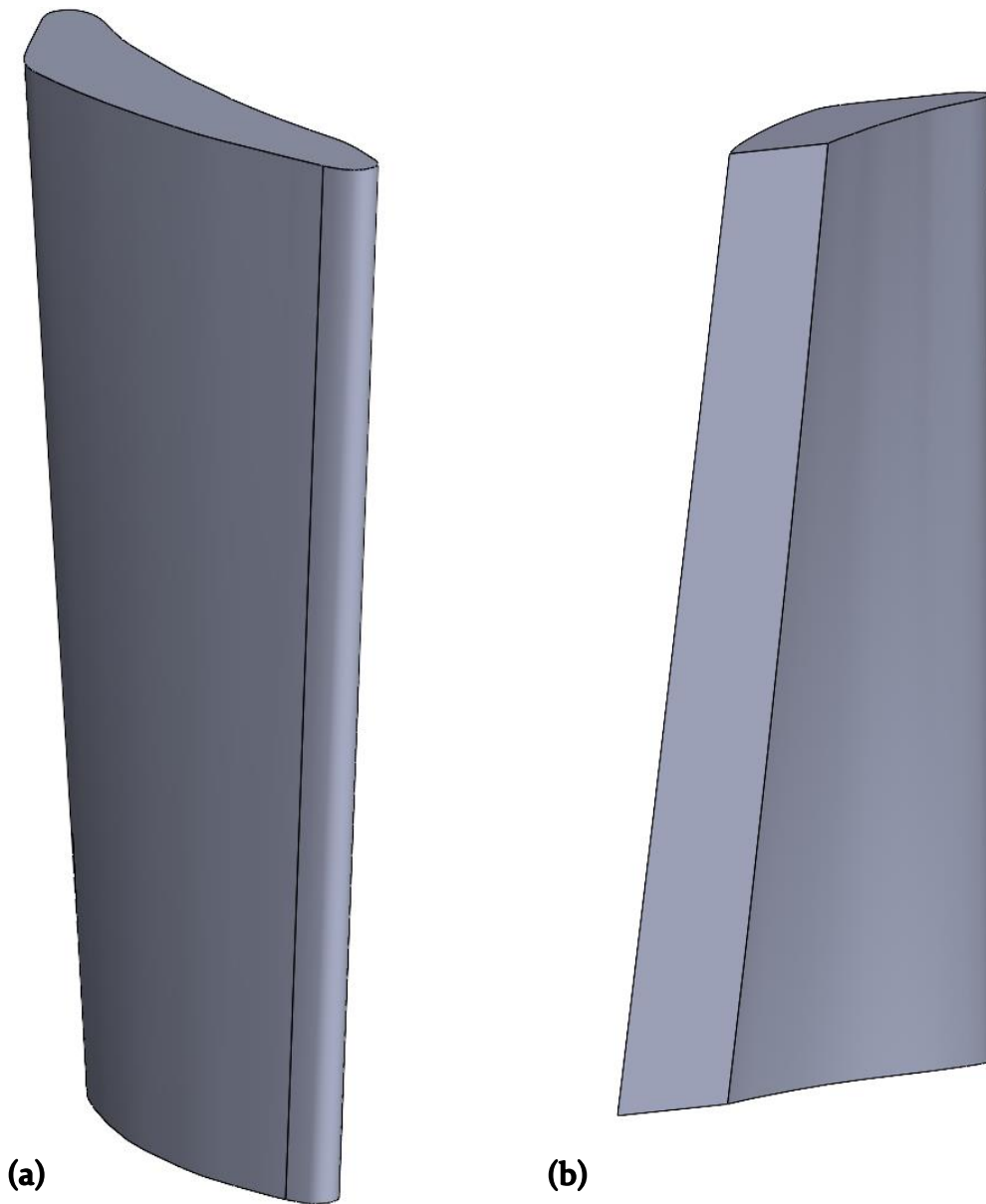


Figure 2-15: Turbine Rotor with Split and Solid Body Contour.

Now that we have a completed and smooth surface of the blade, we need to turn this surface in to a solid component. Leaving the blade as a surface would not allow for creation of the flow domain in later sections. To make this blade into a solid component another SolidWorks tool was used. In this case the Surface Knit SolidWorks tool was used. To use this tool the top and bottom of the blade had to be capped off with another surface. Fortunately, due to the method of modeling this was as easy as selecting the beginning and final surface used to create the blade profile. We could then use the same command to “fill” the enclosed space created

by the surfaces. This would give a completed solid component that can be seen in Figure 2-15 (b).

The explained process was done for the turbine rotor, turbine stator, centrifugal compressor, and the engine shroud. The more simple components of the engine utilized the scanning to confirm measurements but were mostly done by measuring the component directly and then modeled in SolidWorks with standard solid modeling.

Once all of the components had been modeled, they needed to be combined into a full assembly. Due to the method of importing and scanning, several assemblies were created. The initial assemblies were to complete the more complex geometries of the engine where the blades and the base of the components were modeled separately and needed to be combined into one part. The more complex geometries of the engine can be seen as modeled in Figure 2-16 and Figure 2-17. These assemblies could now be brought together to create the full engine model. The full engine model assembly can be seen in Figure 2-18 & Figure 2-19.

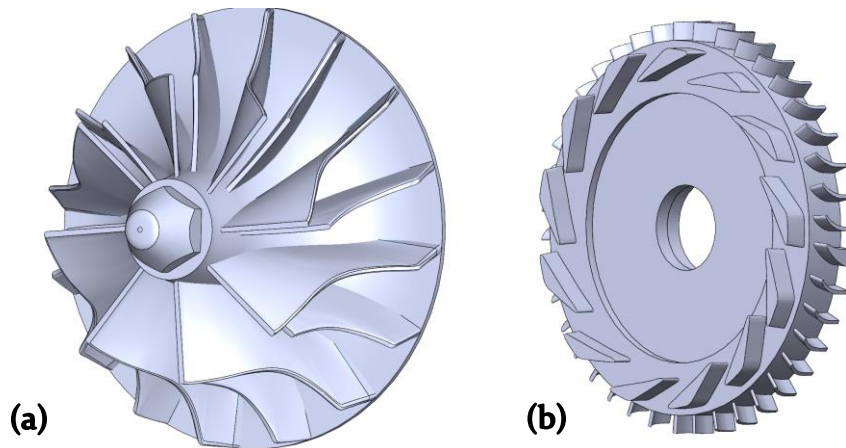


Figure 2-16: Modeled Compressor Rotor and Stator.



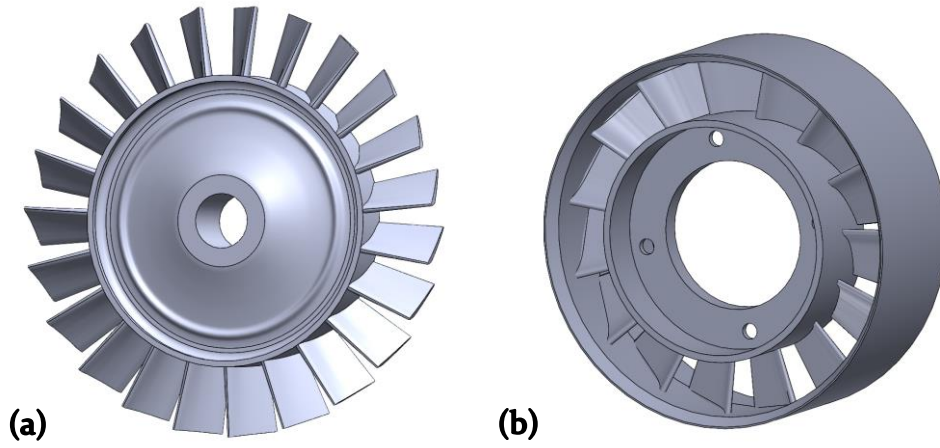


Figure 2-17: Modeled Turbine Rotor and Stator.

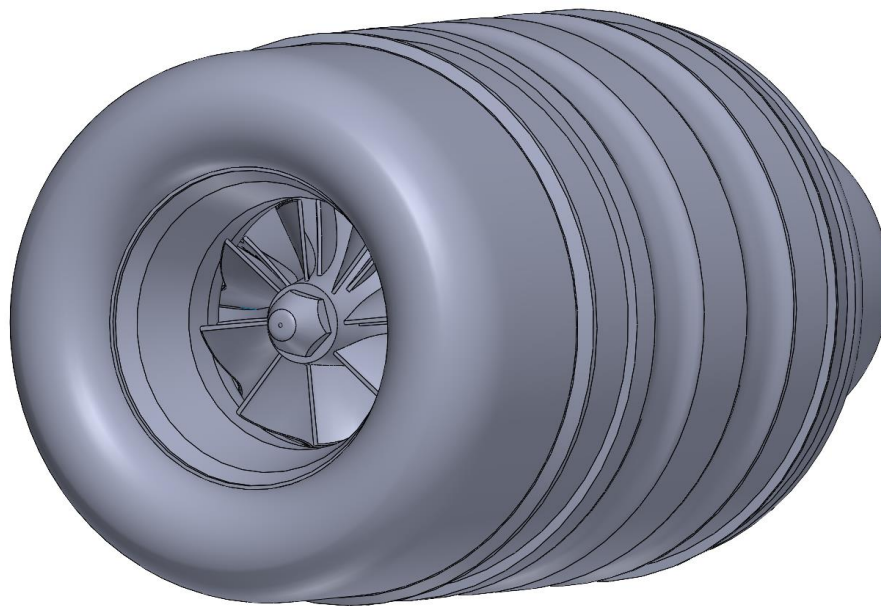


Figure 2-18: Fully Modeled TJT-3000 Micro Turbine Engine.

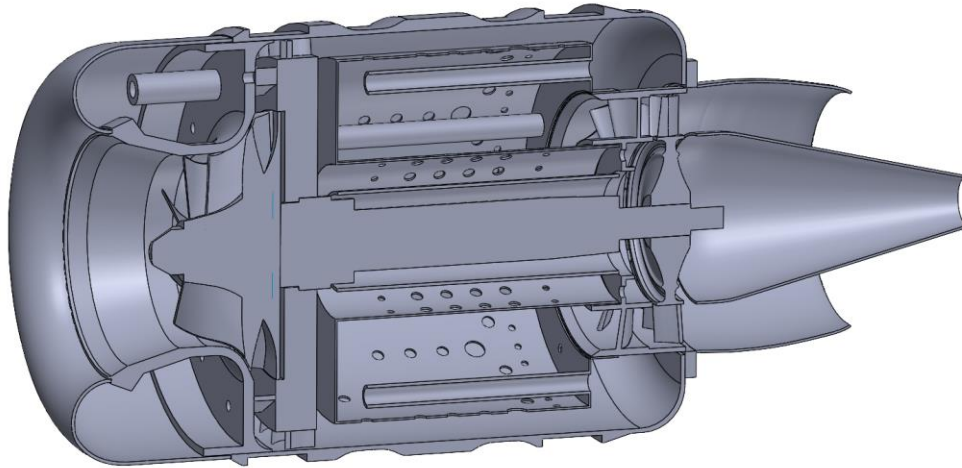


Figure 2-19: Section View of Fully Modeled TJT-3000 Micro Turbine Engine.

**Simplification Process:**

With the completed engine assembly, the model had to be prepared for CFD simulation. The extra details and edges of the engine model would cause issues for meshing and slow down the simulation. The simplification method would involve a few more SolidWorks features which would make use of the decision earlier to make all of the components into solid models.

The first steps were to simplify the model and remove unneeded geometries. This would include features like the shaft that is housed through the center of the engine, the geometry on the outside of the engine shroud, and any details beyond the contour for the bladed components. A simplified engine model can be seen in Figure 2-20 & Figure 2-21.

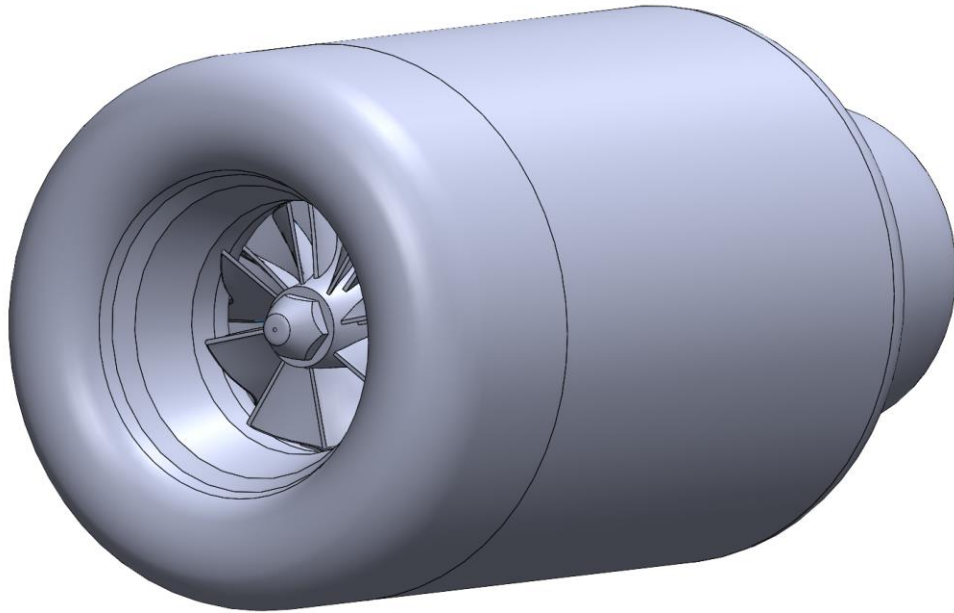


Figure 2-20: Simplified Fully Modeled TJT-3000 Micro Turbine Engine.

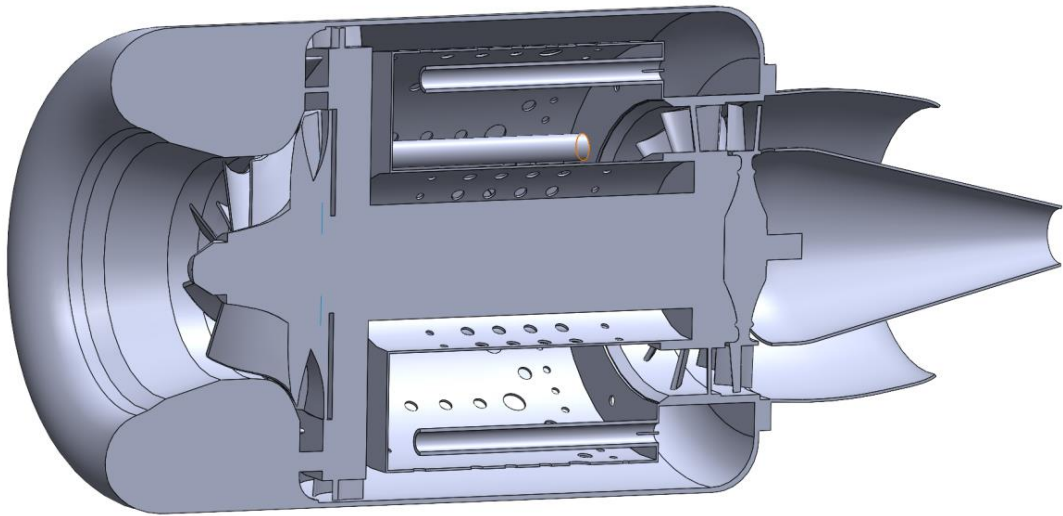


Figure 2-21: Simplified Section View of Fully Modeled TJT-3000 Micro Turbine Engine.

Once the simplification process was complete the model would then be cut down into sections that are advantageous for modeling. The main section here would be the combustion chamber as it was the focus of this project. A view of this combustion chamber as it was simplified can be seen in Figure 2-22.

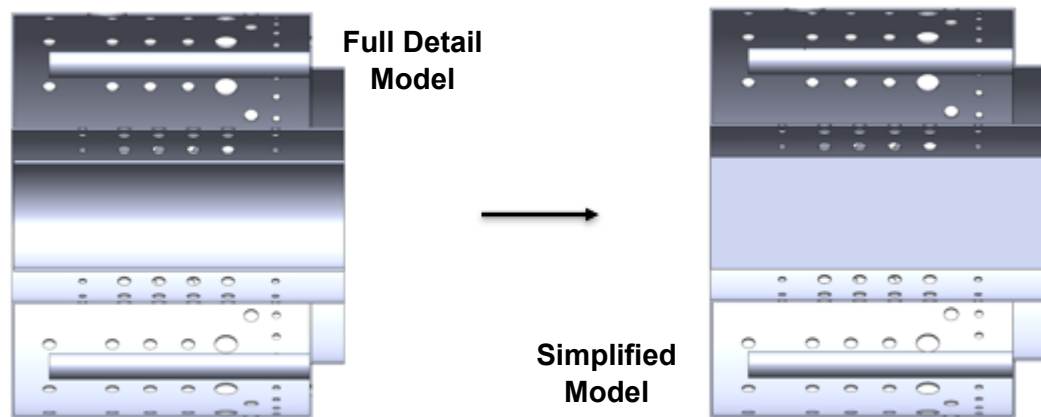


Figure 2-22: Simplification of Combustion Chamber

With the simplified section, there was further refinement to be done to prepare the model for meshing. To get a more accurate simulation, the flow domain as well as the solid domains of the combustion chamber had to be modeled. To get the fluid domain of the combustion chamber as a solid body, the cavity command for SolidWorks was utilized. This was a feature that would allow the combination of two parts, where the component of the operators choosing would remove material from the other. In this case, a solid block would be combined with the simplified combustion chamber geometry to create the flow path of the combustion chamber. The combustion chamber geometry would be placed in a solid block large enough to encompass it, then the cavity command would be used on the combustion chamber. This command would modify the block to now have an empty space where the combustion chamber was. After further refinement to cut the block in line with the engine geometry, this would become the fluid domain.

To also include the solid portions of the engine in the analysis, the simplified combustion chamber geometry and fluid domain were combined once again in an assembly. While combining these two primary domains, a third domain was added within the flow domain of the combustion chamber which will be called the “spark” domain. It was located in the area that the glow plug for the engine would allow for the ignition of fuel inside of the combustion chamber which was critical for the simulation section of this project.

The completed simplified model encompassed three individual bodies. These bodies would be considered the “Fluid Domain” “Solid Walls”, and “Spark”. A Figure of this three bodies model can be seen in Figure 2-23. The flowpath through the engine is the fluid domain, the Solid Walls are the solid Domain and the Spark is another solid domain made for the use of ignition during the CFD phase.

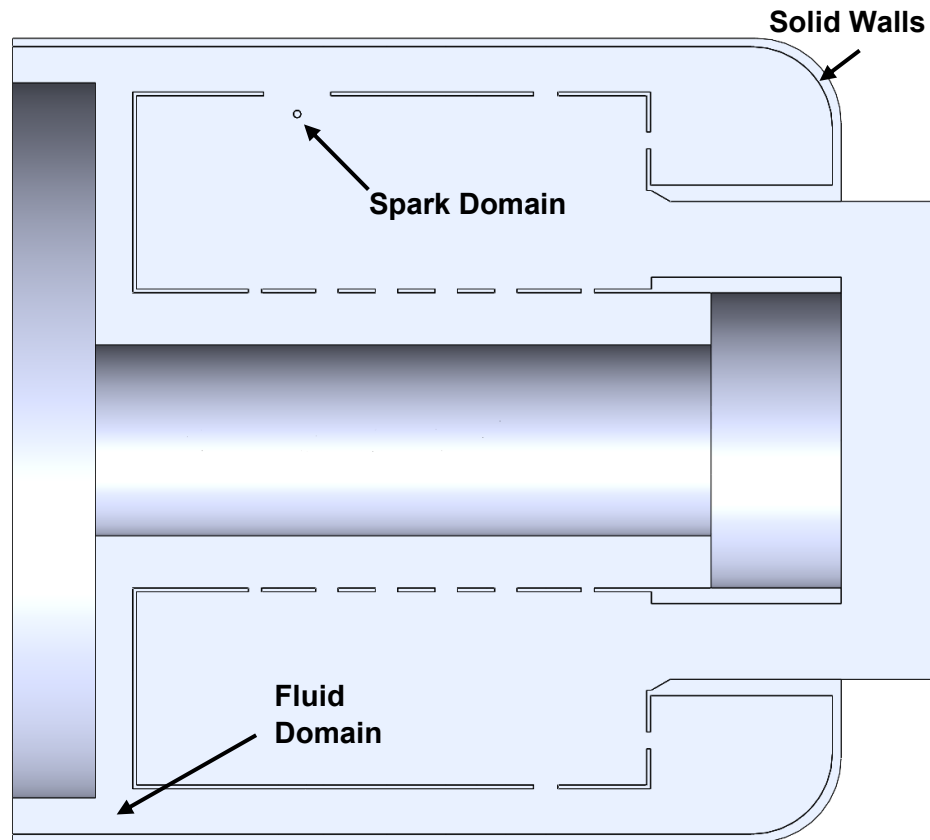


Figure 2-23: Combustion Chamber Three-body Domain

Although the fluid domain is modeled as one connected region, this domain of the combustion chamber is categorized by three categories for clarity. These categories include the “Inner Combustion Chamber”, “Outer Combustion Chamber”, and “Shroud Flow”. Seen in Figure 2-24, the inner combustion chamber is the fluid domain between the shaft and the inner most walls of the combustion chamber. The outer combustion chamber is the area encompassed by the combustion chamber walls while the shroud flow is the area of flow that starts from the inlet and follows the outer shell of the turbine engine.

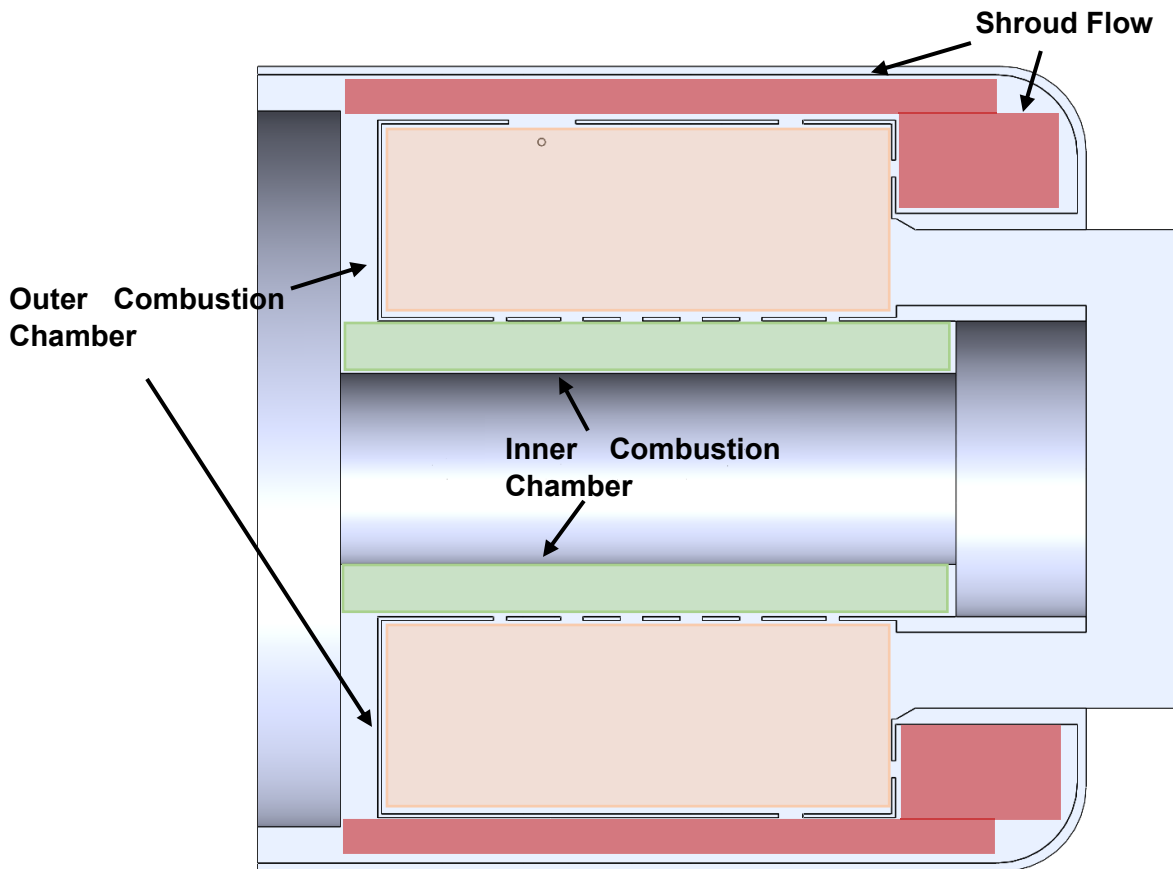


Figure 2-24: Combustion Chamber Fluid Domain Breakdown

**Model Changes:**

With this initial model completed, some additional models would need to be created to alter the geometry and then compare the results of the. To focus on the geometry sections that would be seeing change, an additional Figure of the baseline model can be seen in Figure 2-25. The changed to the model focused on the length of the vaporizing tubes as well as the first set of holes entering the combustion chamber. The first change to the geometry was doubling the combustion chamber hole diameters on the first row as seen in Figure 2-27 while the second change was closing off the first row of holes in the combustion chamber as seen in Figure 2-26 As mentioned in the introduction, the goal of these model changes would be to increase the ease of flow running through the combustion chamber to improve thrust and thermal efficiency. Taking in to account the prior research to predict the ultimate performance of advanced power cycles (Chauhan & Wessley, 2019) and the improvements to thermodynamic considerations (Chiesa, Consonni, Lozza, &

Macchi, 2015) the enlarged holes from the first set of combustion chamber holes would allow this condition. However, care had to be taken not to enlarge the holes excessively as there had been previous literature that indicated that too much flow running through the engine would lead to flame instability and even push the process to the point of extinguishing the flame. (He, Guo, Xu, & Jin, 2021)

Both changed models would also include an additional shortening of the vaporizing tubes, guided by initial modeling results that made it apparent that the flow of fuel into the combustion chamber was hindered when it would leave the vaporizing tubes so close to the back wall of the combustion chamber. These models would have to go through the same process of creating a fluid domain, solid domain, and spark domain. A table explaining the differences between each model can be seen in Table 2-2.

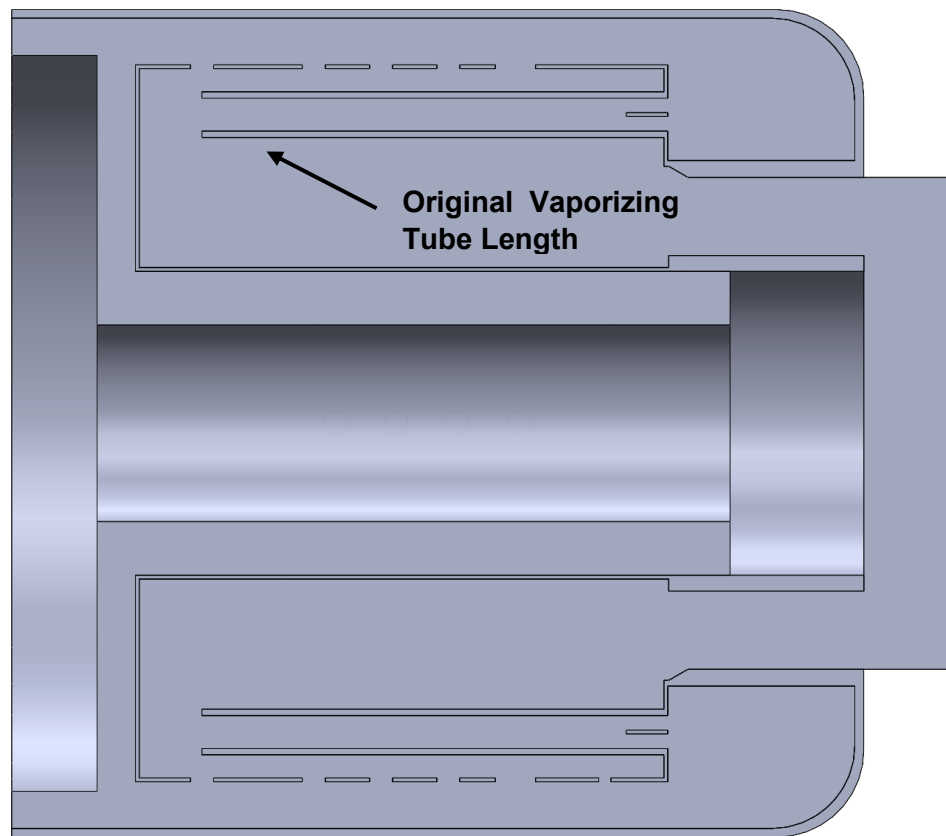


Figure 2-25: Original Combustion Chamber

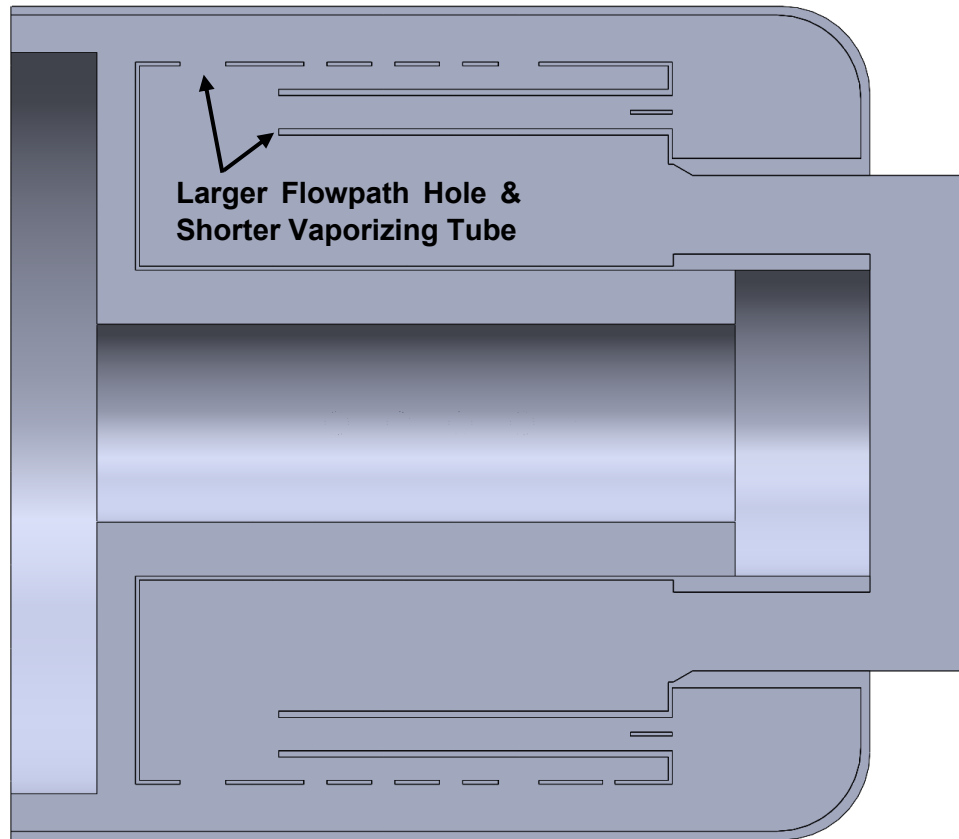


Figure 2-26: Combustion Chamber Geometry Change 1

Table 2-2: Model Geometry Changes

Model	Vaporizing Tube	Flowpath Hole
Baseline	Baseline	Baseline
Model Change 1	10mm Shorter	2x Diameter (10-20) mm
Model change 2	10mm Shorter	Removed



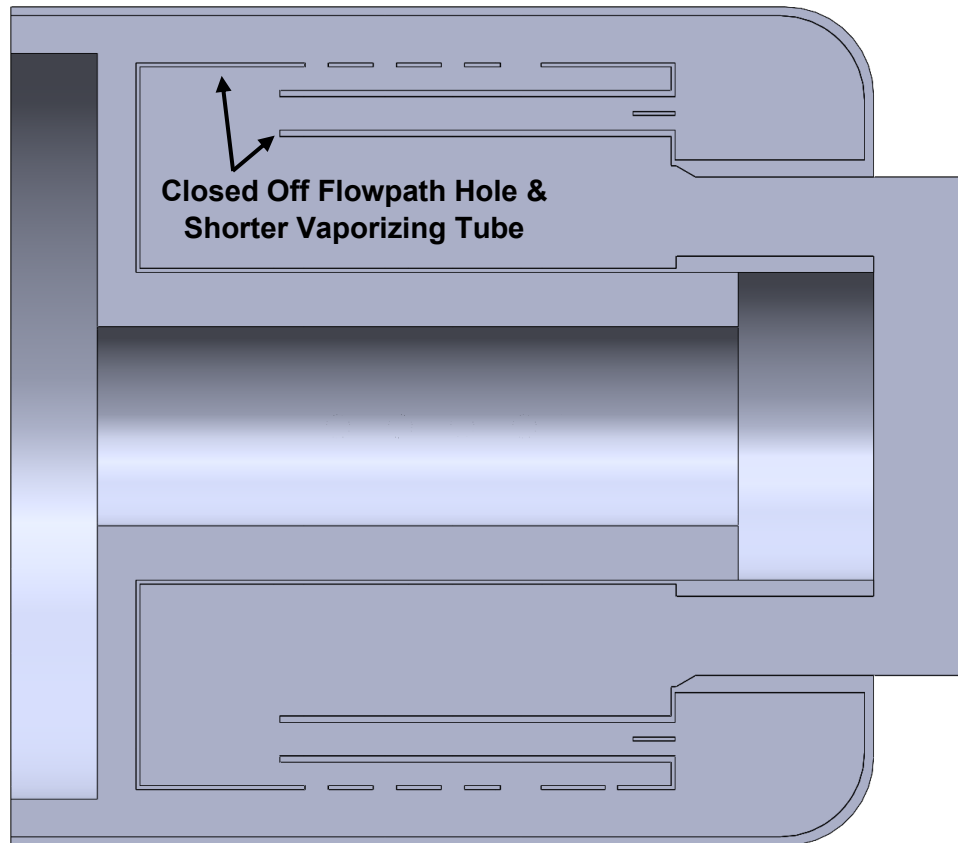


Figure 2-27: Combustion Chamber Geometry Change 2

When generating improvements to the combustion chamber there are several potential problems to be wary of including poor mixing, uneven combustion, environment, and economy (Singh, Kumar, & Kumar)

When considering improvements to the current combustion chamber, the focus was on the mixing of air and fuel in the combustion chamber, as well as avoiding uneven combustion.

### 3. COMPUTATIONAL MODEL

With the CAD models of the combustion chamber section completed, a proper mesh must be created for a solution through CFD. This would be done with the combination of Ansys Workbench as well as Ansys Fluent. For the purposes of meshing, Ansys Workbench was only used for its geometry software where the surfaces of the engine model would be named for easier meshing later. The choice

of name convention was selected to make it clear what the proper boundary conditions were for each of the surfaces. For this model, the geometry was separated into three primary domains. These domains would be the solid, fluid, and spark section mentioned in the modeling section (Section 2.3) of this paper. The solid domains were broken up further which included the inner combustion chamber as well as the outer combustion chamber. This nomenclature has nothing to do with the operation of the engine and is just a method to split up the type of mesh that distributes in the area. This was followed by the fluid domain which would be the remaining geometry that flows through these two solid domains. An image of the inner and outer combustion chamber domains can be seen in Figure 3-1 and Figure 3-2 respectively.

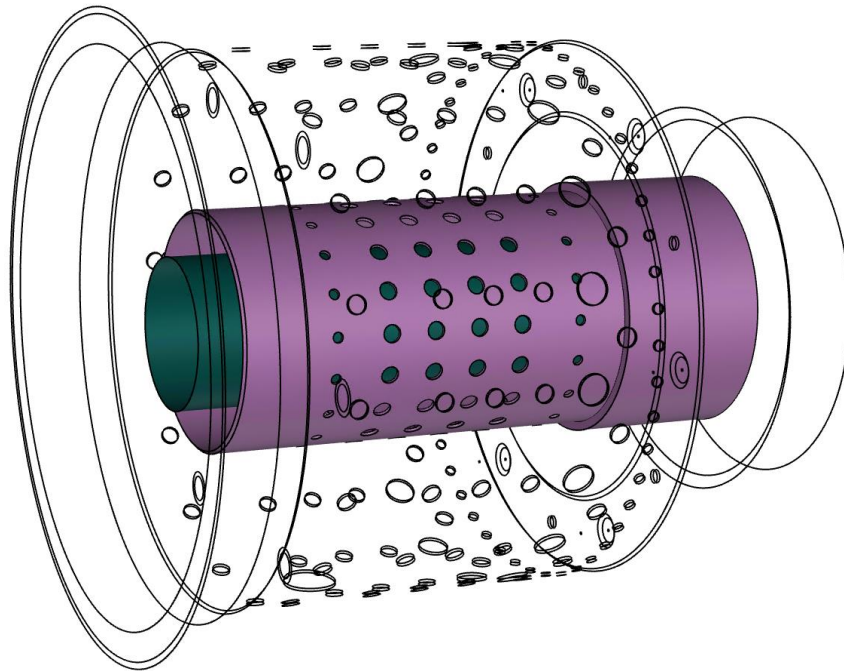


Figure 3-1: Inner Combustion Chamber

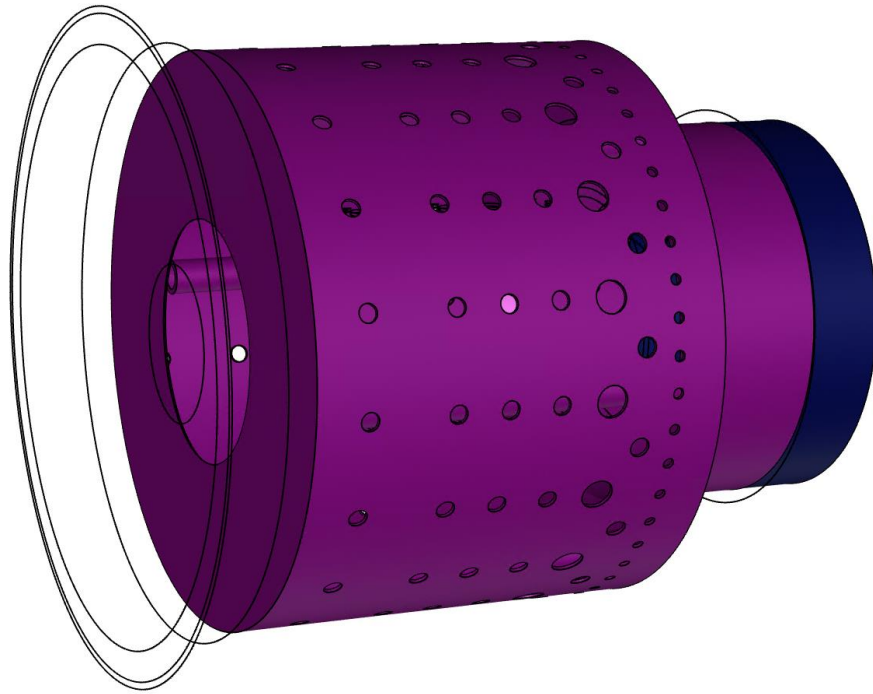


Figure 3-2: Outer Combustion Chamber

### 3.1. Meshing

Over time, the meshing of complex geometry had shifted from an entirely manual approach to a more automatically generated approach. Though this shift began to compromise the accuracy of the simulations in favor of convenience and therefore a hybrid approach was adopted. These hybrid meshes would use structured blocks in areas where the complexity of the geometry is limited, but switch to a more unstructured mesh when the complexities of the geometry increased.

While unstructured meshes are fast and time efficient they do not always offer an accurate solution. The more structured meshing method offers higher quality results. (Krishnamurthy, 2019)

With the naming convention chosen to separate the areas of the combustion chamber, the solid model was moved into the fluent meshing software. This software would be used to create a polyhexcore mesh which would allow for high quality hexahedral elements in the flow areas of the model while using polygonal mesh near the boundary layer to capture the more intricate geometry along the walls of the model, while allowing for less overall mesh complexity.

In a study to test the limits of polyhexcore meshing the turbulent flow surrounding a 100 passenger airliner was tested. The study had found the mosaic meshing to be

parallel scalable, resulting in 6.6x faster computation on a 121 million element mesh with 32 parallel compute cores. During the study, the mesh has predicted 1.5% higher lift than a wind tunnel test, as well as a 10% increase in drag (Zore, Parkhi, & Varghese, 2019).

The modeling steps done prior allowed for the use of what is called watertight geometry in Fluent meshing software. To begin, the mesh on the surface of the model had to be created. This is where the initial nomenclature was very helpful as it allowed for specific local sizing in the model by name selection. For the model a range of elements from 0.0001 inch to 0.001 inch would be used depending on what was considered critical for the model. For this reason, the areas of the model around the fuel injectors would be on the smaller end of this limit. The areas with larger overall size where there wouldn't be as many details such as the inner combustion chamber would be on the larger side of this limit. Inflation layers were a critical component to this model as the flow moving in and out of the combustion chamber, including the perforated holes would need to be observed. For this model the inflation layers of the model were projected from any solid surface adjacent with the flow using a first layer height which would be beneficial for the  $k-\omega$  SST model (Ndeda, Motsamai, & Muiruri, 2019). Finally, Creating the volume of the mesh was a separate section of its own after creating the surface model. The parameters for each of these categories including the overall Y-plus value after meshing can be seen in Figure 3-1.

Table 3-1: Local Sizing Table

Mesh Sizing		
Datum	Location	Sizing (mm)
Outer Combustion Chamber Local Sizing	Outer Combustion Chamber	0.0005
Inner Combustion Chamber Local Sizing	Inner Combustion Chamber	0.0005
Fuel Domain Local Sizing	Fuel Injectors	0.0001
Spark Solid Local Sizing	Spark Plug	0.0001
Surface Mesh	Full Domain	0.0001 - 0.001
Inflation Layers First Height	All Walls (Fluid Side)	1.30E-05
Volume Mesh	Full Domain	0.0001 - 0.0016
Y-Plus (Average)	Full Part	0.81

An overall view of the engine mesh can be seen in Figure 3-3. A section view of the engine can be seen in Figure 3-4, while a view of the polyhexcore meshing can be seen in Figure 3-5

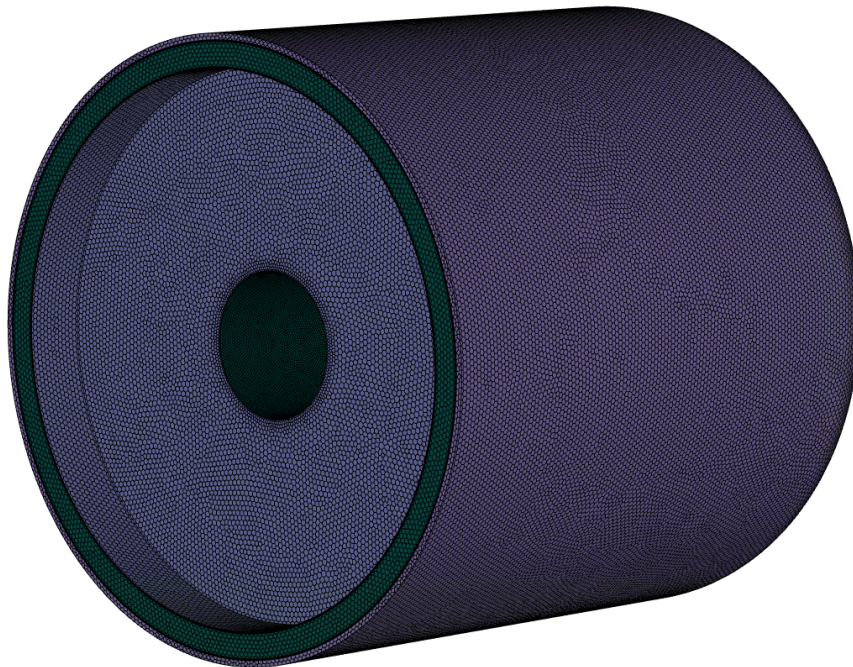


Figure 3-3: Overall Engine Mesh

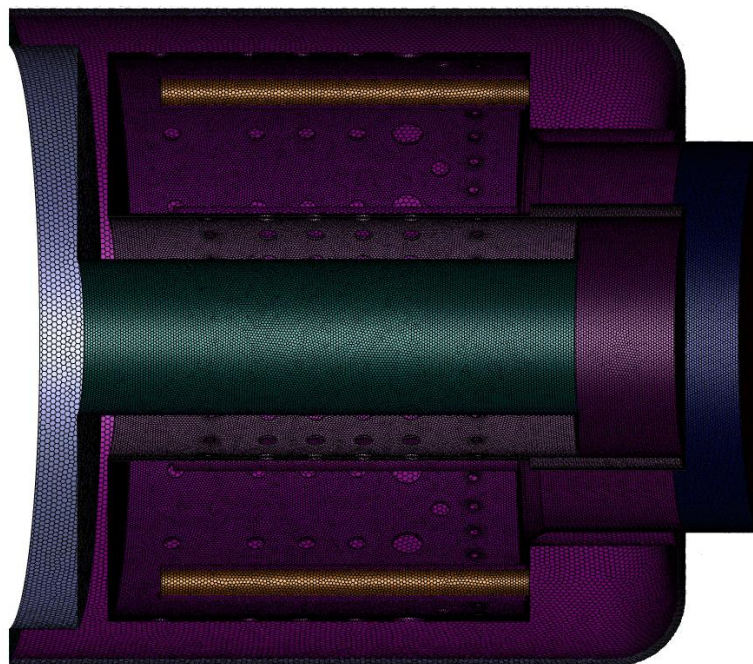


Figure 3-4: Section View of Engine

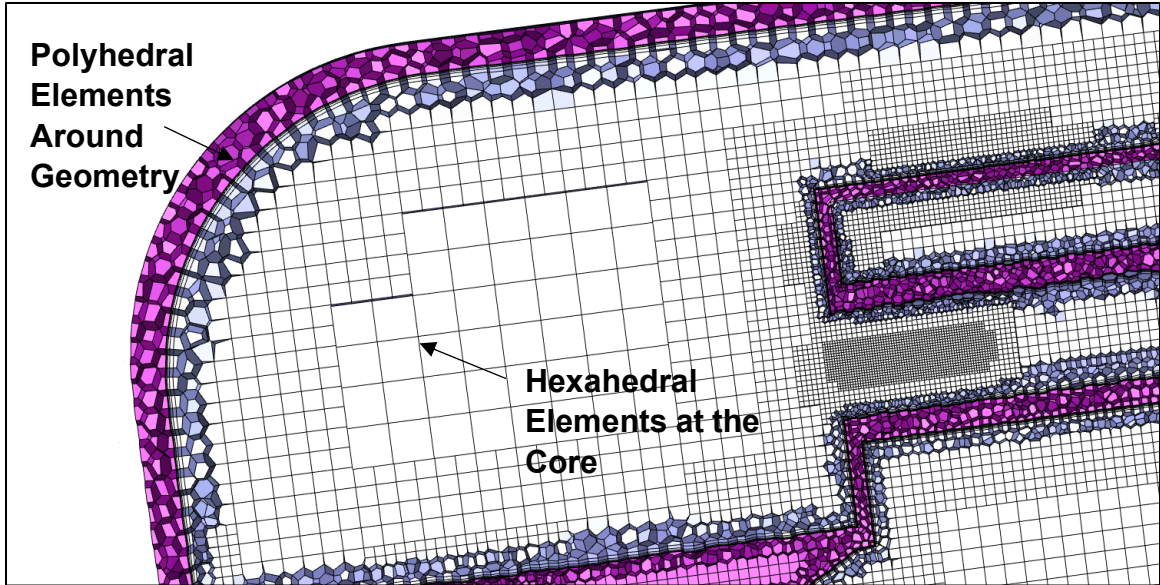


Figure 3-5: Polyhexcore Elements

The mesh for the initial model had a count of 23,335,601 elements with a surface mesh of elements ranging from 0.0001” to 0.001 inch. The critical overall meshing parameters for the combustion chamber model and the parameters from the changed geometry models can be seen in Table 3-2.

Table 3-2: Overall Mesh Criteria

Overall Mesh Sizing				
Model	Overall Elements	Y-Plus (Average)	Y-Plus (Outer-Combustion Chamber)	Y-Plus (Inner-Combustion Chamber)
Baseline	23335601	1.0455742	0.56671441	0.565921
Open Flowpath	21330299	0.38	0.56	1.207
Closed Flowpath	22984548	0.18600179	0.2325623	0.3167335

**Mesh Convergence & Y-Plus:**

With the mesh created, the convergence of the mesh was to be confirmed. This would include the calculation of the overall temperature difference between the

maximum temperature of the combustion chamber and the outlet temperature at the turbine inlet for the baseline model. This change would be considered “dT”. The focus of this practice was to ensure that even with the reduction in elements this parameter would not change substantially, therefore confirming the consistency of the results. The results of the mesh convergence can be seen in Table 3-3. In this table the maximum change between two of the dT values is 2.14% and the change from the 23 million element mesh to the 16 million element mesh was only 0.25%. This result implies that the original model was already converged and the slight variations in the dT could be a result of extra detail from vortices due to the higher element models.

Table 3-3: Mesh Convergence Criteria

Mesh Convergence						
Datum	Error Equation	Mesh Size	Fluid Average	Fluid Max	Outlet Average	% Error
dT	$\frac{T_{avg1} - T_{avg2}}{T_{max} - T_{out}}$	23 mil	868.804	2281.492	639.03142	x
		19.8 mil	841.08027	2300.465	599.46462	1.629849
		16 mil	831.36648	2027.4678	598.80254	0.679921

As the models for the other geometries were very similar, the convergence of the baseline model was used as justification that the other models with above 20 million elements would be converged. This resulted in the number of elements for the other models seen in Table 3-2.

Another consideration for convergence of the model is the y-plus value displayed by the wall conditions for the elements. Y-plus is described by equation 3-1. In this equation  $y^+$  is the non-dimensional wall distance and  $y$  represents the dimensional distance to the wall. The friction velocity and kinematic viscosity are  $u_*$  and  $\nu$  respectively. The result of this calculation is a non-dimensional wall distance which can aid in confirming the accuracy of a simulation (CFD-Online, 2014). The quantity manipulated to improve the y-plus for the model is the height of the first mesh cell next to the wall. To improve this value, inflation layers were implemented into the model on every wall that would be in contact with the flow domain. The value of y-plus would be ideal as close to or less than 1 due to the k-omega SST model being chosen. A table of the y-plus values achieved for the model can be seen previously in 3-2

$$y^+ = \frac{u_* y}{\nu}$$

### 3.2. Simulation Setup

With the mesh created the parameters for the simulations had to be set. Due to the focus on the combustion chamber, some operating parameters had to be set with estimates from other similar research on micro turbojet engines. First, the consideration of transient and steady state was reflected.

When modeling the combustion process in a turbojet the flame created from the process is slightly unsteady but overall, the oscillations are negligible. The combustion process in the combustion chamber is continuous and self-sustaining if fuel is still being injected into the engine. For this reason, the model can be run as a steady state flow problem (Singh, Kumar, & Kumar)

Originally the consideration of the density based model for the simulation was made. According to Ansys, the different calculation approach of the pressure and density base solvers prevents the density based solver from utilizing the non-premixed combustion method. The density based solver was meant for high-speed and compressible flows. This difference causes the density based solver to vary its use of energy, momentum, and continuity equations. (ANSYS, 2009)

The choice of turbulence model for a turbine engine combustion analysis seemed to vary greatly depending on choice of the researcher. Variance from models using basic k-epsilon to LES were noted.

The choice of combustion model for this analysis was made as a consideration of computation time as well as accuracy. The computation time and power needed to run an LES or DES model is the reason these models were not selected. As a balance of accuracy and time, RANS would be the model of choice. Within RANS K-epsilon was considered but decided against due to its limitations for not being accurate on no-slip walls, and adverse pressure gradients.

K-omega SST was ultimately chosen due to its beneficial convergence in jet flow, avoiding flow detachment and recirculation that would be an issue in k-epsilon and standard k-omega. For both general and external aerodynamic simulations, the k- $\omega$  sst model is the best overall fit for aerospace applications (Solmaz, 2021) (Malalasekera & Versteeg, 2007)



In this high turbulence model, k-omega SST was used to generate a solution. Pressure based-fully coupled, second order upwind and central discretization. Discrete linear system solver using Gauss seidel (Zore, Parkhi, & Varghese, 2019)

The modeling parameters of the simulation can be seen in Table 3-4,. The primary physical models of focus are Energy, Viscous Model, and the Species of choice for the model.

Table 3-4: Modeling Parameters

Modeling Parameters	Value
Multiphase	Off
Energy	On
Radiation	Off
Viscous Model	SST k-omega
Radiation	Off
Heat Exchanger	Off
Species	Non-Premixed Combustion

**Modeling Parameter Details:**

For the purpose of this model, the choice was made to use the non-premixed combustion. The non-premixed combustion model would allow the injection of fuel from a predetermined inlet or set of inlets of which would combust under the right thermodynamic conditions upon entering the combustion chamber. Ideally, the fuel entering the model would be in liquid form and evaporate to create the gaseous fuel as would happen in the experimental run of the combustion chamber, but this was omitted as the primary focus of this simulation is to observe the effect of geometric changes instead of the intricate details of an exact spray-evaporation model. Due to the choice of injecting the fuel as a gas, the volume flow rate of the inlet condition for the model would have to be carefully considered or an unrealistic supersonic flow could be induced at the inlet of the fuel.

**Non-Premixed Combustion:**

The setup for non-premixed combustion included the choice of a fuel as well as the choice of oxidizer as a parameter of mass fraction. As the fuel of the TJT-3000 is kerosene, it was selected as the fuel with the appropriate mass fraction and the oxidizer was chosen as air with the appropriate nitrogen and oxygen element mass fraction as seen in Table 3-5. (ToolBox, 2003). The mass balance of these elements are set as the initial conditions with a limited number of reactions to aid in reducing

the complexity of the simulation and allow multiple models to be run for comparison.

Table 3-5: Non-Premixed Combustion Setup

Species	Fuel	Oxid
Kerosene	1	0
N <sub>2</sub>	0	0.767
O <sub>2</sub>	0	0.233

When modeling with non-premixed combustion a Probability Density Function table (PDF table) is to be created. This table is what dictates the “PDF-Mixture” material which is chosen for the fluid region of the model. This mixture will include the chosen species and the properties of the mixture will vary depending on the mean mixture fraction otherwise known as the fuel concentration of the mixture. An example of one adapting variable is the density of the mixture which can be seen in Figure 3-6.

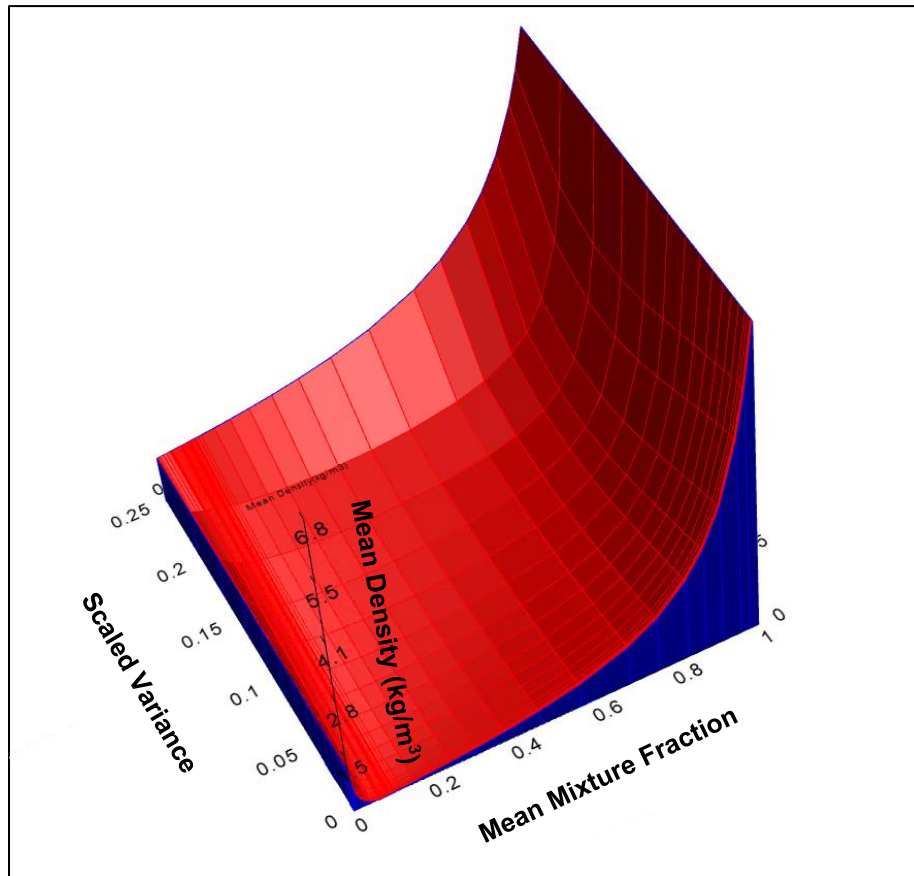


Figure 3-6: PDF Table for Non-Premixed Combustion

According to this displayed table, as the fuel is consumed the mean density of the mixture will reduce as would be expected. The characteristics of the PDF table can be seen in Table 3-6.

Table 3-6: PDF Table Characteristics

PDF Table Characteristics	
Category	Selection/Value
State Relation	Chemical Equilibrium
Energy Treatment	Non-Adiabatic
Operating Pressure (Pa)	101325
Fuel Stream Rick Flammability Limit	0.1
Initial Number of Grid Points	15
Maximum Number of Grid Points	200
Maximum Number Species	20
Minimum Temperature (K)	298

### 3.3. Modeling, Boundary, & Initial Conditions

With the models of the simulation selected, the boundary conditions of the model had to be selected. The collection of the boundary conditions for the combustion chamber were based off both experimental data as well as literature review. As the modeled section, the combustion chamber, was just a segment of the engine. The parameters for both the inlet and outlet would have to be based on what was expected from a full model of the engine. Unfortunately, the literature is limited on the expected turbine inlet pressures of a micro turbine engine of the same size as the TJT-3000. However, the outlet conditions for the model were based off an experimental model of a BMT 120 KS gas turbine (Large & Pesyridis, 2019). This is a slightly larger and more powerful turbine engine with an expected thrust of 13.256 kg vs the TJT-3000 12.5 Kg, but a reduction based off the reduced RPM would be implemented. In a separate study aimed at providing a “simple calculation” for experimental results of a turbine engine. The scaling of the expected pressure within

the combustion chamber to the RPM run of the compressor. Figure 10 of this research was interpolated with an expected value of 65.2% pressure value decrease to a 63.5% RPM decrease from maximum speed (Krampf, 1992). Now returning to the previous study (Large & Pesyridis, 2019) the expected drop in pressure was applied to the pressure within the combustion chamber just after the compressor found from Figure 9 in their literature. This value was 320 Kpa. The value from this reduced pressure was then applied with the same pressure drop as found in the study resulting in the pressure outlet selected. These values can be seen in Table 3-7.

**Table 3-7: Outlet Condition Findings**

<b>Outlet Condition</b>	
Datum	Value
Percent of Max RPM	0.634920635
Expected Pressure Fraction of Percent RPM	0.652
Pressure Value at Location 4 (Kpa)	320
Pressure Value Based With Reduction (Kpa)	208.64
Figure 9 Pressure Drop 10% aft of Location 4 (Kpa)	52.75
Pressure Drop Percentage	0.83515625
Final Outlet Pressure (Kpa)	174.247

The inlet flow characteristics of the model come from the engine lab setup as well as some models run on the micro turbine engine that the TJT-3000 is based off of, the KJ-66. Literature on fully coupled CFD models of the KJ-66 is available for rotational speeds of 80,000 RPM which is well within the capabilities of the TJT-3000 which has a maximum speed of 126,000 RPM. In the CFD model, the TJT-3000 is assumed to be running at half its maximum fuel rate which would correspond with approximately 90,000 RPM (Campbell, Latimer, & Scholes, 2006).

The fully coupled KJ-66 model had concluded that the expected air to fuel rate of the combustion chamber would be 65:1 (Wang, et al., 2020). This value would be used at the input for the inlet of the combustion chamber as the controlling factor for the throttle of the engine in the experiment was the fuel rate injected into the engine. A table of the expected specifications of the TJT-3000 turbine engine can be seen in Table I-1.

Following the expected limitations, as well as the conditions found in literature, a list of the boundary conditions for the combustion model can be seen in Table 3-6. The engine characteristics of the TJT-3000 can be referenced from Table I-1. Table

3-8 is quickly followed by Figure 3-7, and Figure 3-8 which show the location of the boundary conditions on the model as established in SolidWorks between the combustion chamber and the full model.

Table 3-8: Combustion Model Boundary Conditions

Model Boundary Conditions				
Boundary	Index	Type	Unit	Value
Fuel Inlet (Red)	Mass flow	Mass flow	Kg/s	0.002154
	Temperature	Initial	K	300
	Fuel Mass Fraction	Boundary	N/A	1
Flow Inlet (Blue)	Mass flow	Mass flow	Kg/s	0.14
	Temperature	Initial	K	300
	Fuel Mass Fraction	Boundary		0
Outlet (Yellow)	Pressure	Pressure Outlet	kPa	174
Inner Combustion Chamber Walls	Wall Motion	Stationary Coupled Wall	N/A	0
	Thermal	Coupled	N/A	0
Outer Combustion Chamber Walls	Wall Motion	Stationary Coupled Wall	N/A	0
	Thermal	Coupled	N/A	0

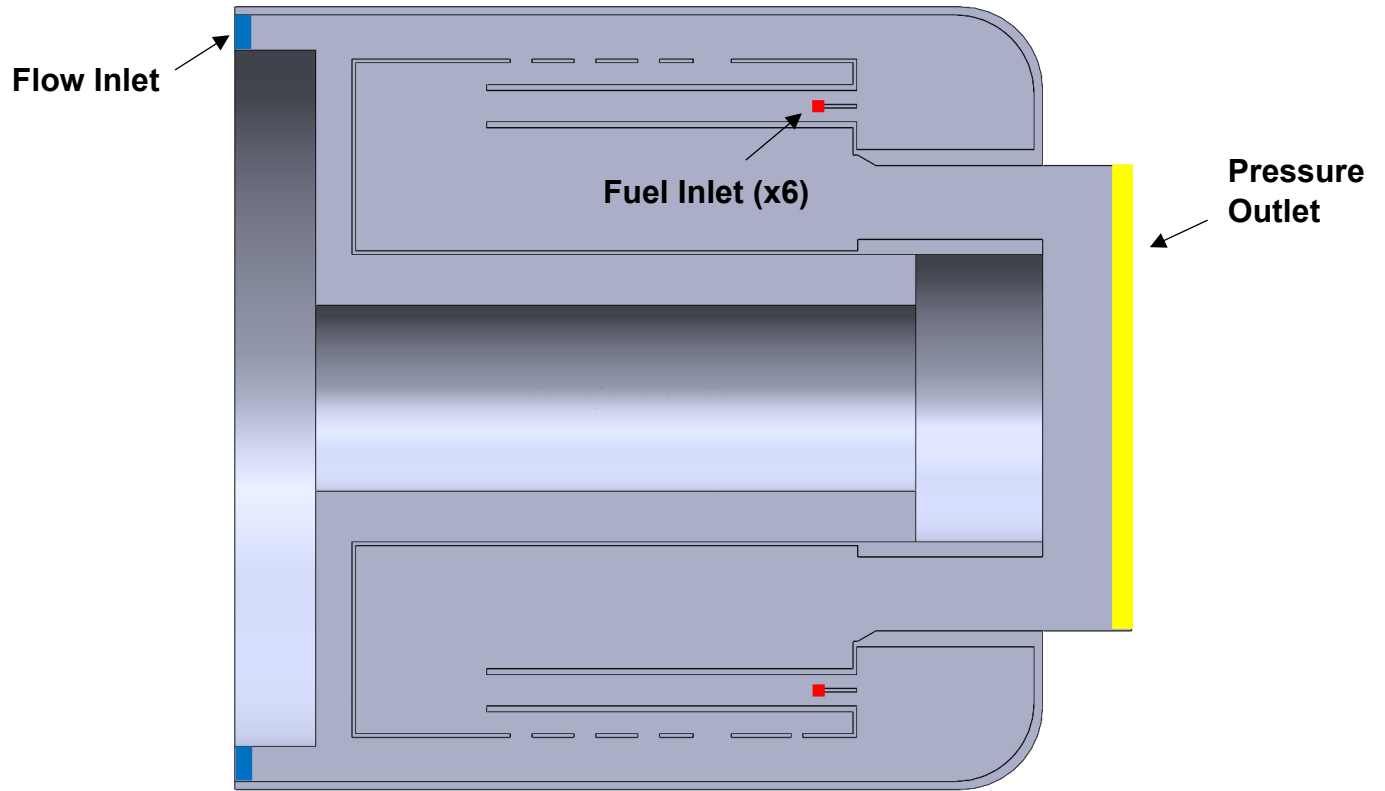


Figure 3-7: Boundary Conditions on Simplified Model

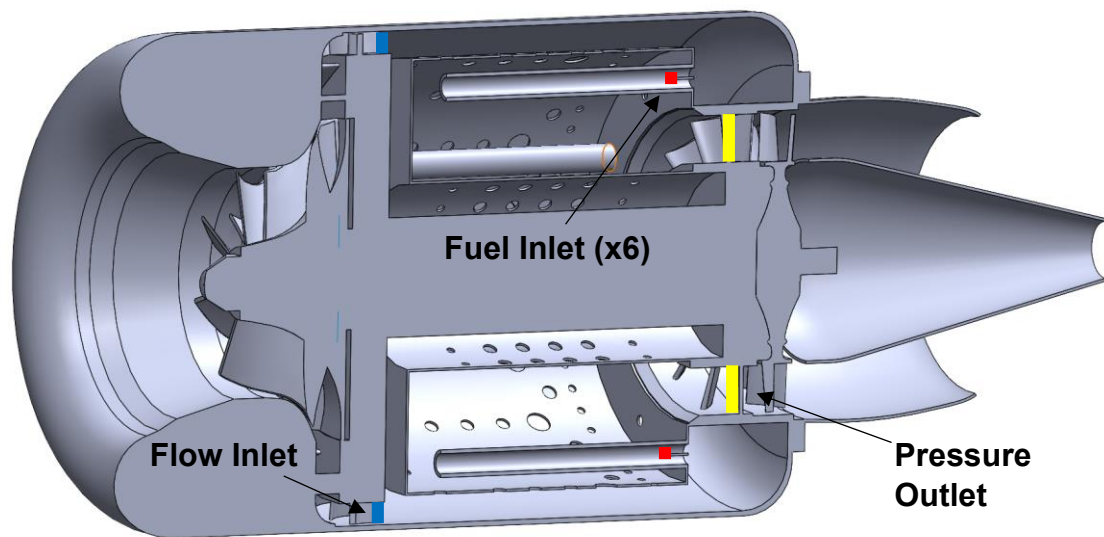


Figure 3-8: Boundary Conditions Related to Full Model

The final setup considerations before running the model would be the solution methods. A table of all solution methods can be seen in Table 3-9

Table 3-9: Model Solution Methods

Model Solution Methods	
Index	Property
Scheme	Coupled
Gradient	Least Squares Cell Based
Pressure	Second Order Upwind
Momentum	Second Order Upwind
Turbulent Kinetic Energy	First Order Upwind
Specific Dissipation Rate	First Order Upwind
Energy	Second Order Upwind
Mean Mixture Fraction	Second Order Upwind
Mixture Fraction Variance	Second Order Upwind

## 4. RESULTS

With the baseline and modified models completed, a comparison of the impact of geometric changes on the temperature of the overall combustion chamber and turbine inlet temperature can be performed. The turbine inlet temperature would be the primary focus of these models as this would be the driving force for the thermal efficiency of the engine.

The results of this simulation will be displayed as two cross section planes running through the center axis of the combustion chamber. The (y,z) axis of the combustion chamber will show the cross section of vaporizing tubes and how this flowed along the engine while the (x,y) plane will show the results from a front view crossing the center of the combustion chamber. These planes can be seen in Figure 4-1.

The initial sections will be focused on the baseline model to show the areas for potential improvement, once the contours for the baseline model are shown the results for all compared models and their contours will be shown.

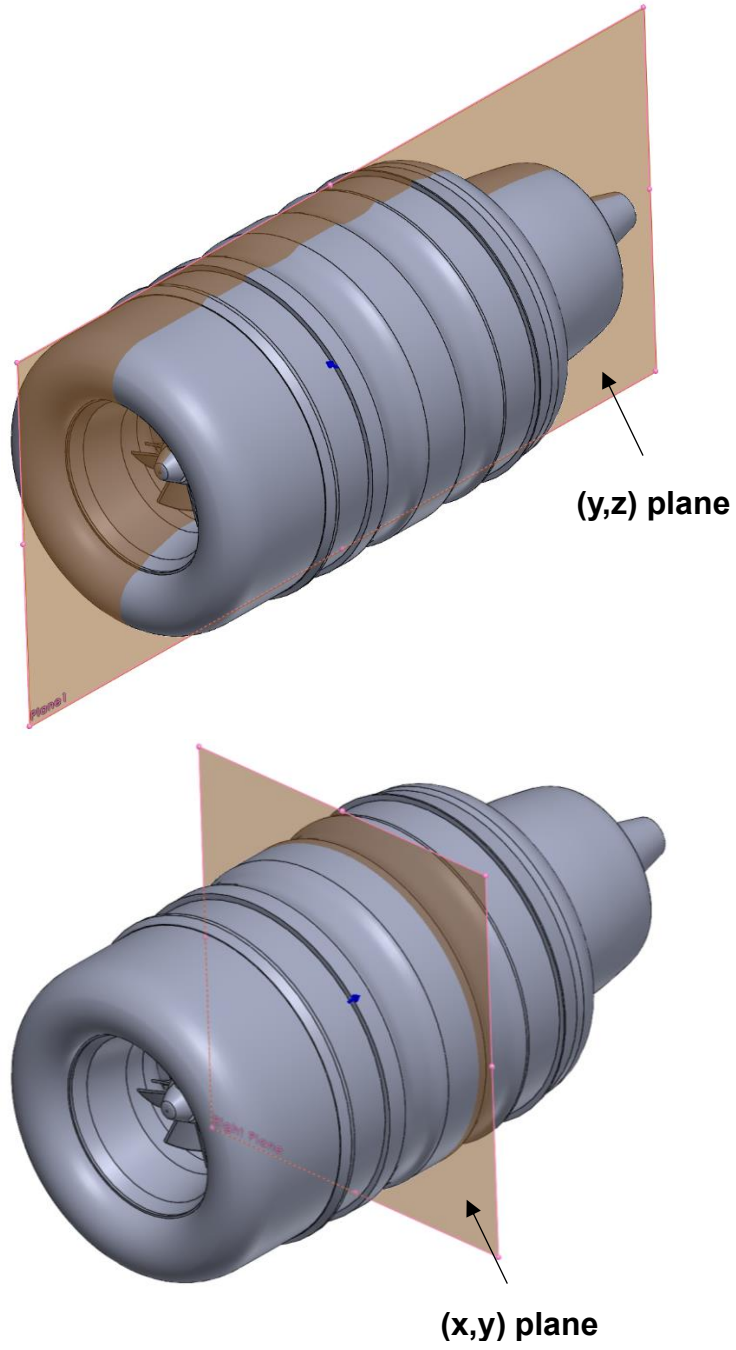


Figure 4-1: Cross Section Planes for Results



#### 4.1. Simulation Results – Base Model

The results chosen for comparison include the velocity, temperature, concentration of oxygen, and pressure. These results when compared together will give a full picture as to where improvements can be made to the base model.

##### **Velocity Results:**

To start, the overall velocity contours of the engine were captured on the (y,z) section plane of the engine that includes the vaporizing tubes. There are three main observations for this model including the vaporizing tubes, velocity entering the inner combustion chamber and the distribution of velocity leaving the pressure outlet. These points can be seen in Figure 4-2 and Figure 4-3.

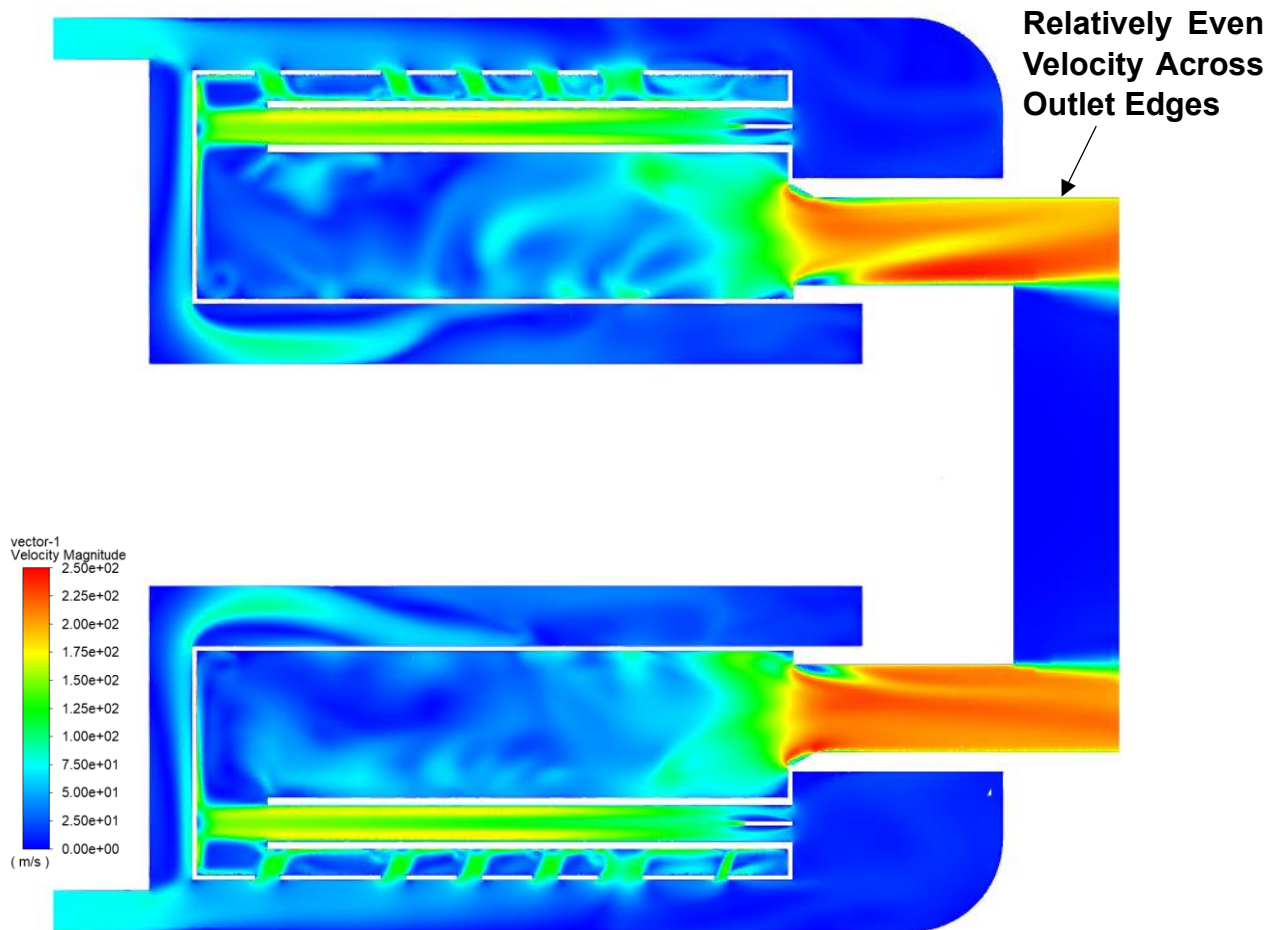


Figure 4-2: Engine Velocity Contour

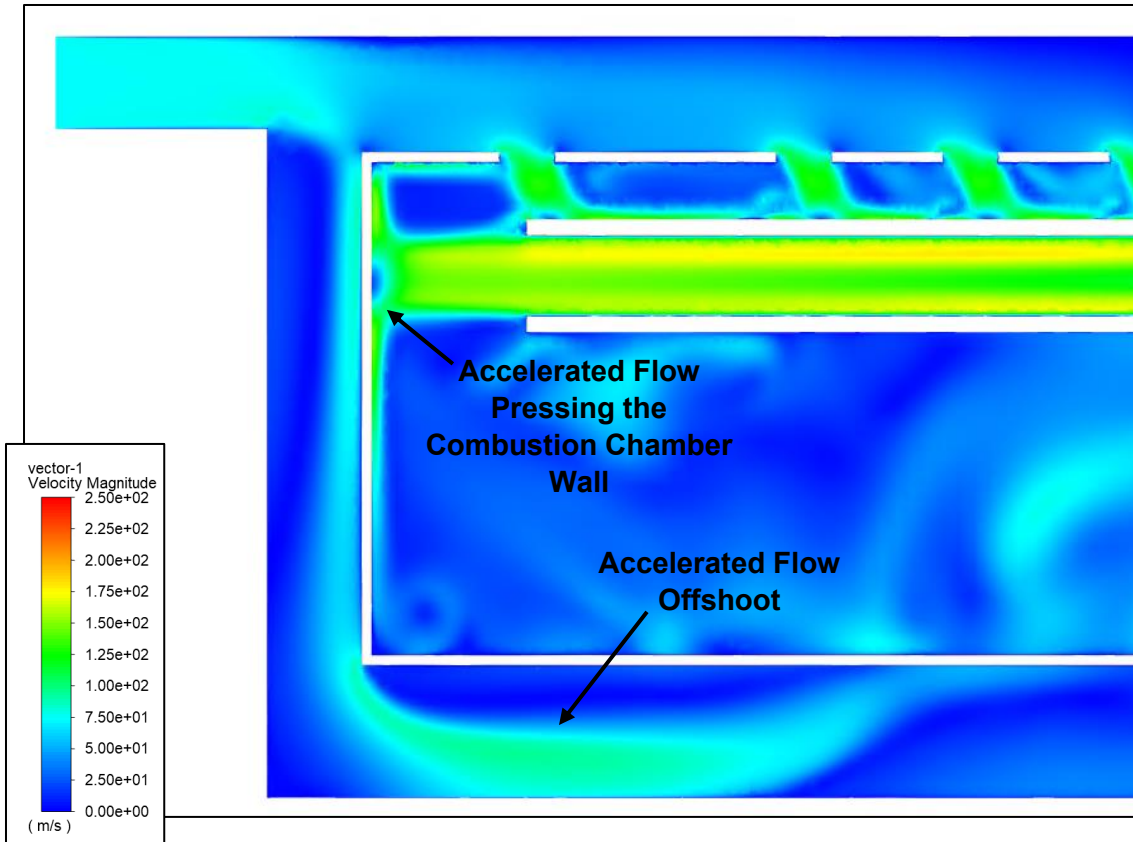
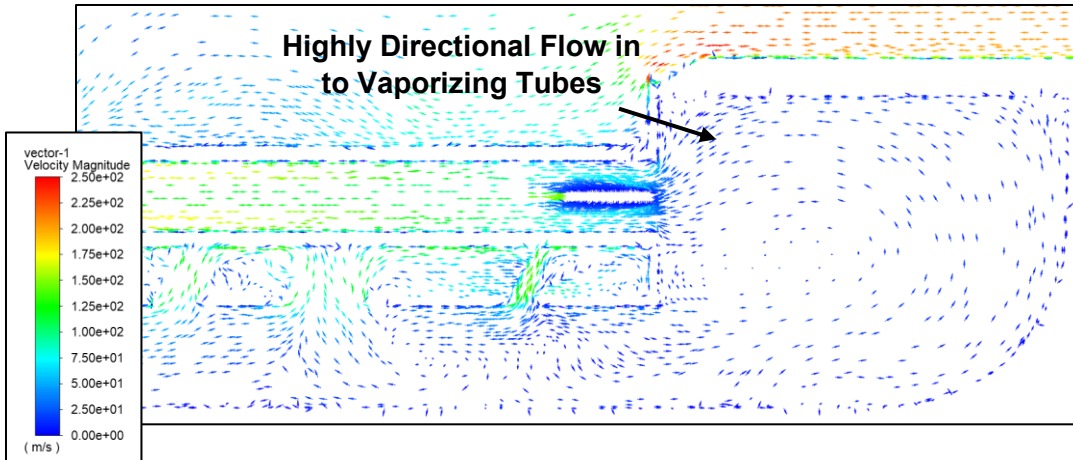


Figure 4-3: Accelerated Flow Offshoot

The accelerated flow offshoot seen in Figure 4-3 next to the inlet of the combustion chamber that quickly enters the inner combustion chamber area. This stream of accelerated flow is causing an area of concentrated stagnant flow when attempting to change direction towards the inner combustion chamber. What will be made more apparent in later contours is the high pressure increase that this redirection of flow is causing. This stagnant flow is not ideal for the pressure drop of the engine and can lead to reduced efficiency.

The acceleration of flow running through the vaporizing tubes seems to be aided by the shroud of the combustion chamber near the back of the engine. The flow here for the base model appears to do a very good job of redirecting through the back of these vaporizing tubes accelerating flow. The problem the accelerating flow through the vaporizing tubes is with how stagnant the flow becomes as it leaves the vaporizing tube and immediately is pressed into the front wall of the outer combustion chamber. This area appears to be something that could be optimized to allow for more turbulent flow and allow for more flow through the combustion chamber overall. See Figure 4-4.



**Figure 4-4: Flow Rotation in to Vaporizing Tube**

### **Temperature and Oxygen Mass Fraction Results:**

The temperature contour for the combustion chamber also yielded some considerable results. As can be seen from Figure 4-5, the combustion is starting right outside of the inlet due to the fuel injected being in a gaseous phase. In a normal operation, the fuel would be injected as a liquid and evaporate within the vaporizing tubes before entering the combustion chamber. Nevertheless, one should consider the location of the highest temperatures within this contour. The highest temperatures are located near the front of the combustion chamber. This is to be expected this is the area where fuel is being injected from the vaporizing tubes. As the fuel is consumed, multiple streams of fresh air are entering the rear of the combustion chamber cooling down the flow as it accelerates out of the back of the combustion chamber.

The entry of cold flow into the outer combustion chamber section from the inlet condition as well as any flow that was directed through the inner combustion chamber perforated holes is critical to the cooling of the flow before reaching the turbine inlet. This effect can be seen when observing the oxygen mass fraction and temperature contours together. The effect is clear when looking at Figure 4-6 where there is a lack of any oxygen near the vaporizing tubes where the fuel concentration would be high. The oxygen concentration increases within the outer combustion chamber when moving towards the back of the combustion chamber when the flow can move through the perforated holes and apply enough cooling to the turbine inlet.

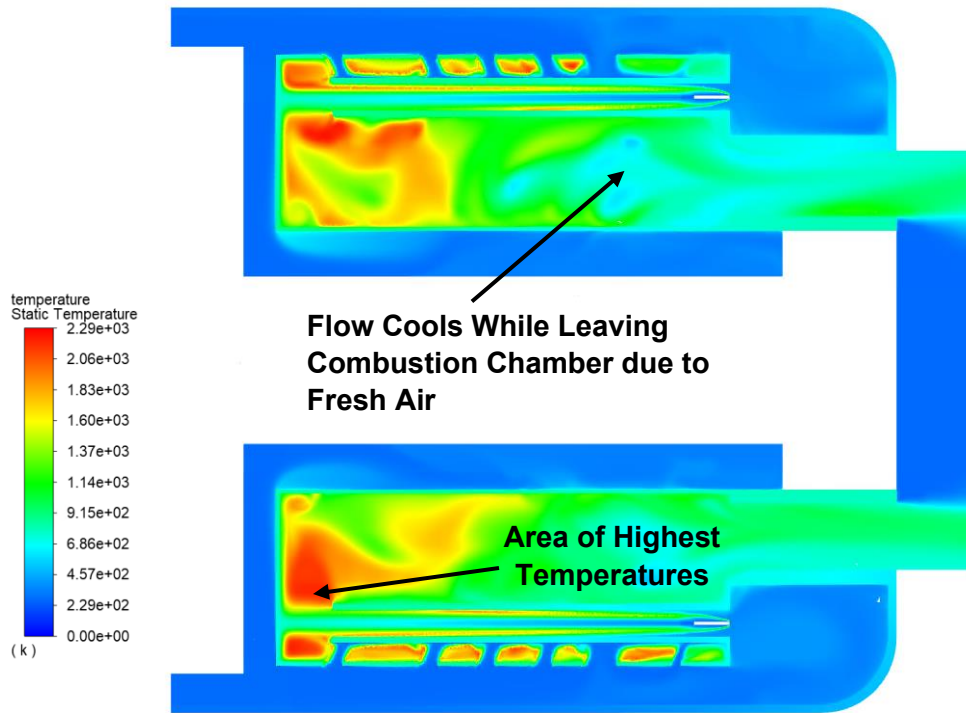


Figure 4-5: Side Profile Temperature Contour

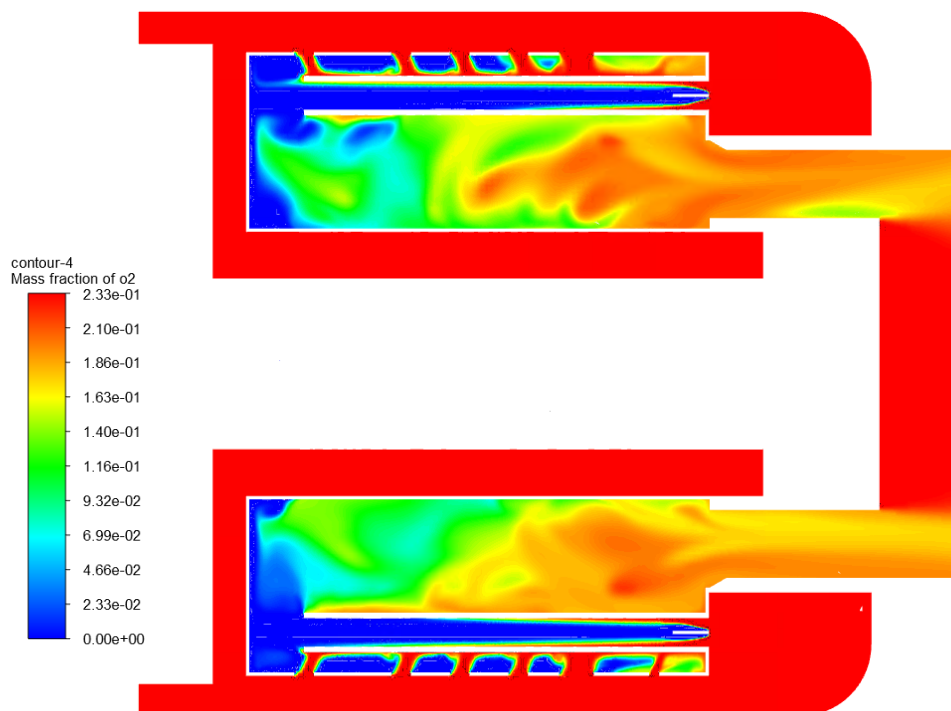


Figure 4-6: Side Profile Oxygen Contour

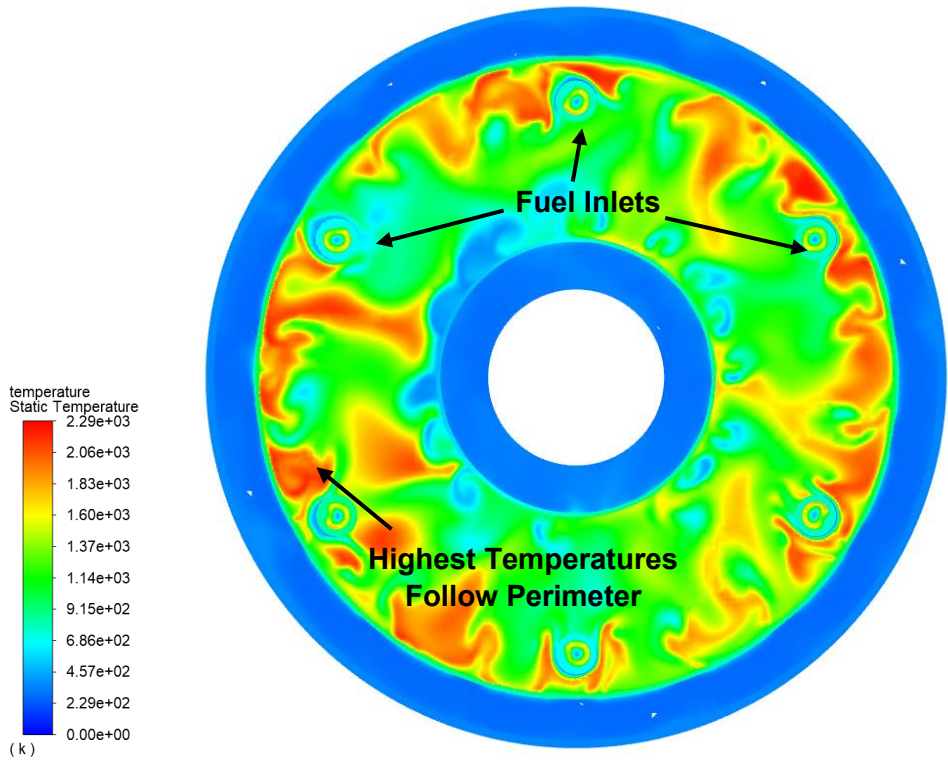


Figure 4-7: Head on Temperature Contour

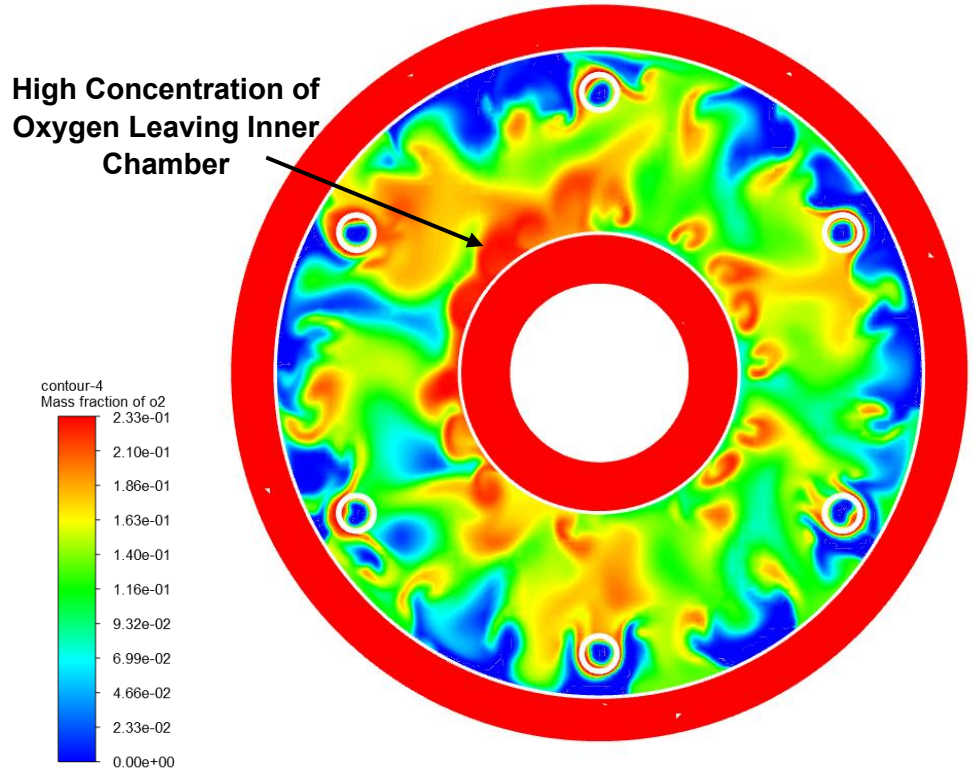


Figure 4-8: Head on Oxygen Contour

Additional details can be obtained by looking at the temperature contour on a cross section plane of the combustion chamber. Seen in Figure 4-7, the highest temperatures are located around the vaporizing tube and the perimeter of the outer combustion chamber where the combustion is focused around the fuel inlet. This is reflected in the results of Figure 4-8 where the absence of oxygen is located on the perimeter of the outer combustion chamber. Within this contour it is also clear how the fresh flow is moving from the inner combustion chamber to aid in the cooling of the turbine inlet.

### **Pressure Results**

Finally, we can look at the pressure across the combustion chamber. As found in the literature review (Large & Pesyridis, 2019), the pressure drop along the combustion chamber is expected to be minimal. Figure 4-9 confirms this. With a pressure drop of .02 MPA across the combustion chamber, the chosen pressure boundary condition was heavily influential on the overall pressure of the combustion chamber.

To some surprise, the highest-pressure area was within the inner combustion chamber. The amount of flow being redirected into the inner combustion chamber caused a high pressure zone which would have to be alleviated. Another area of high pressure was the previously mentioned vaporizing tubes where the flow became somewhat stagnant. These conditions can be seen in Figure 4-10. The final area of concern was the flow moving along the shroud flow areas, mainly the area of redirected flow towards the vaporizing tubes. The area being redirected causes a large amount of stagnant flow and creates an unwanted high pressure area seen in Figure 4-9

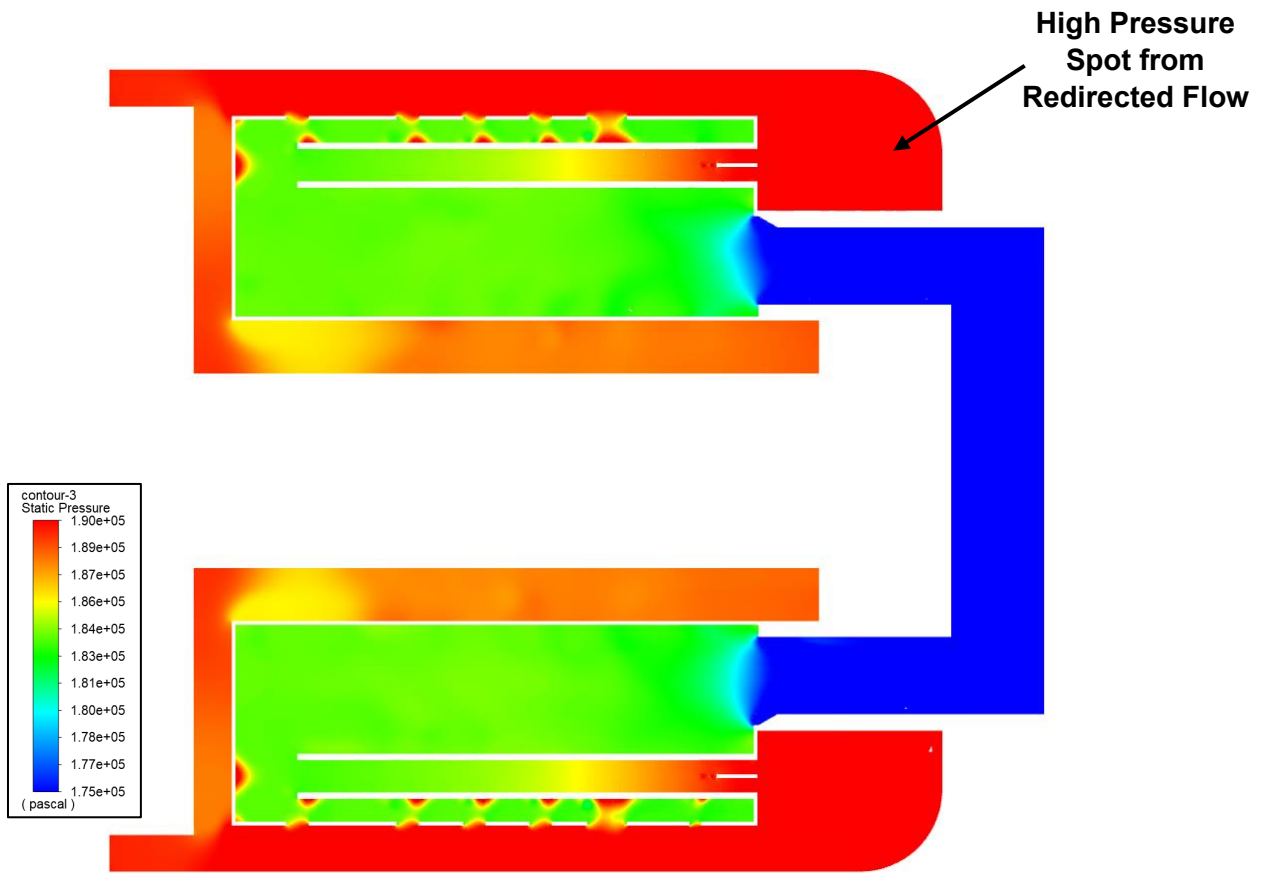


Figure 4-9: Combustion Chamber Pressure Contour

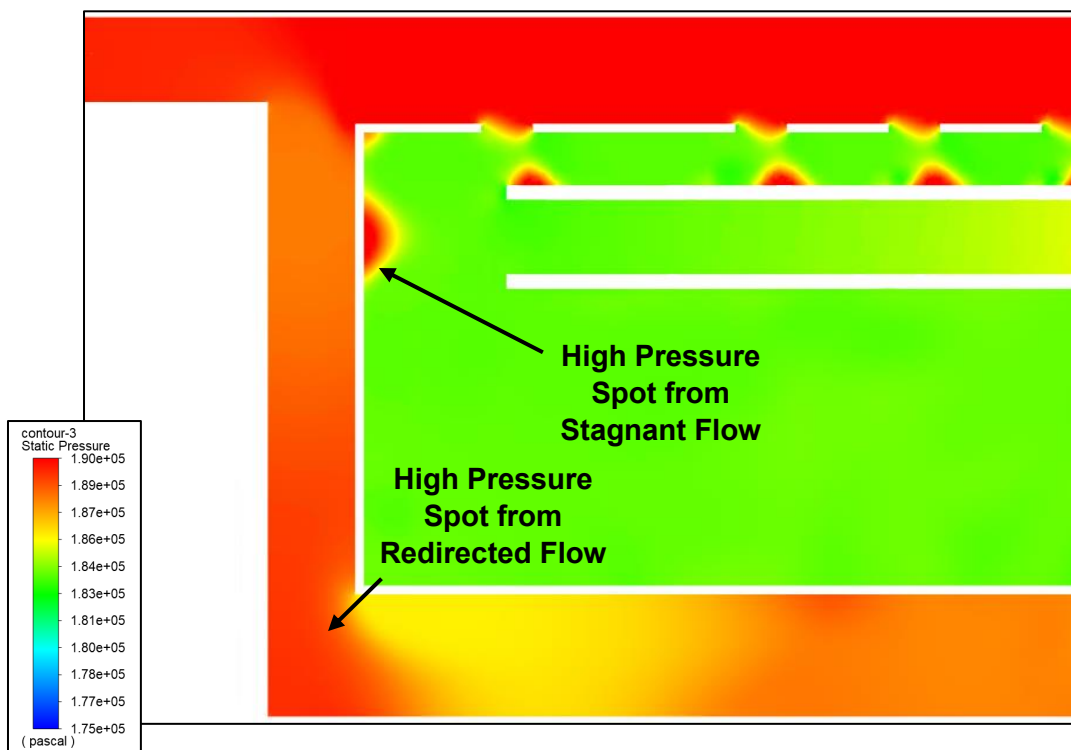


Figure 4-10: High Pressure Close-up

### Contour Overlays – Base Model:

Each of the previously displayed contours tell us about the model individually, but when displayed together they can tell a bigger story. Figure 4-11 displays the velocity vector and temperature contours together for the base model. This figure shows how the areas that are hottest within the combustion chamber are where flow slows down and circulates, and the flow cools down as the velocity vectors accelerate. A close up of these conditions can be seen in Figure 4-12 and Figure 4-13.

Of note in these comparison models is the locality of high temperature zones related to the speed of the flow running through the engine. It is especially noticeable in this overlapping contour of velocity vectors and temperature where the high velocity streams of flow almost appear to “pierce” the high temperature regions leaving cooler flow remaining. This should be considered when considering future improvements to the engine if specific components need additional cooling. The focus of the stream of flow running by the hotter components would aid in cooling. The more stagnant flow is to be avoided where hot spots are not desired.

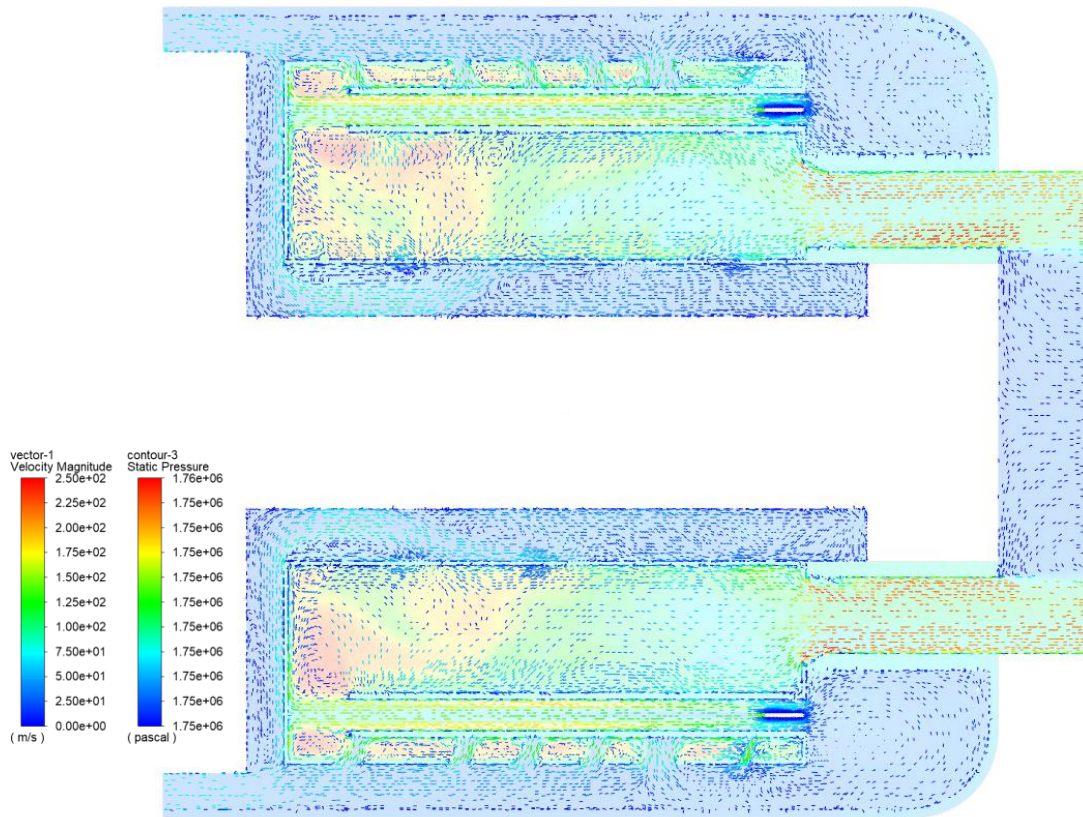


Figure 4-11: Velocity Vector & Temperature Overlay



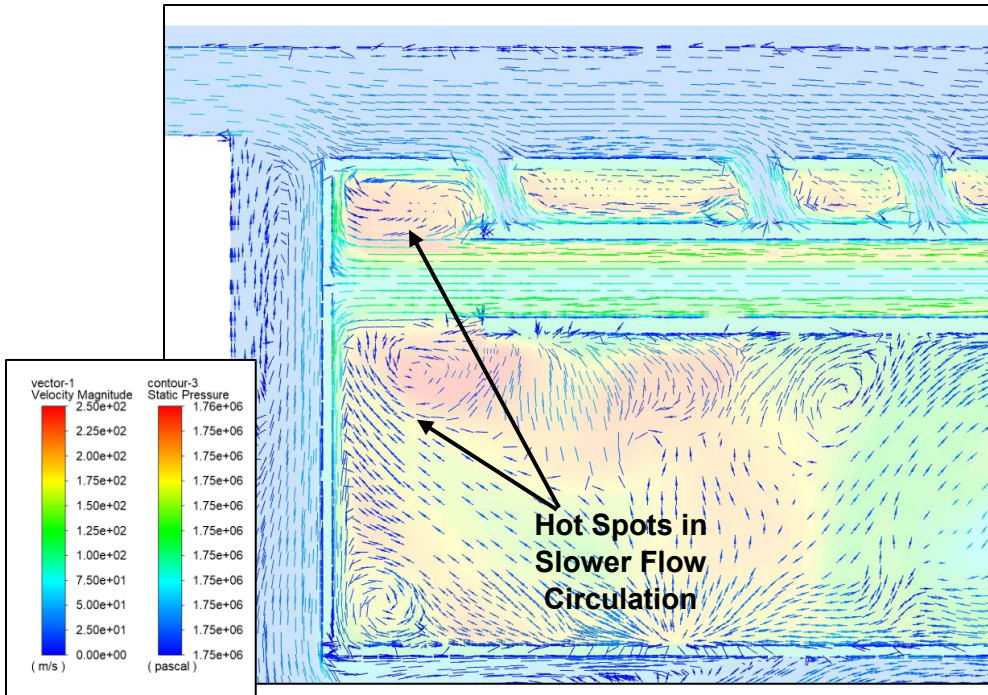


Figure 4-12: Velocity Vector & Temperature Overlay Close-Up

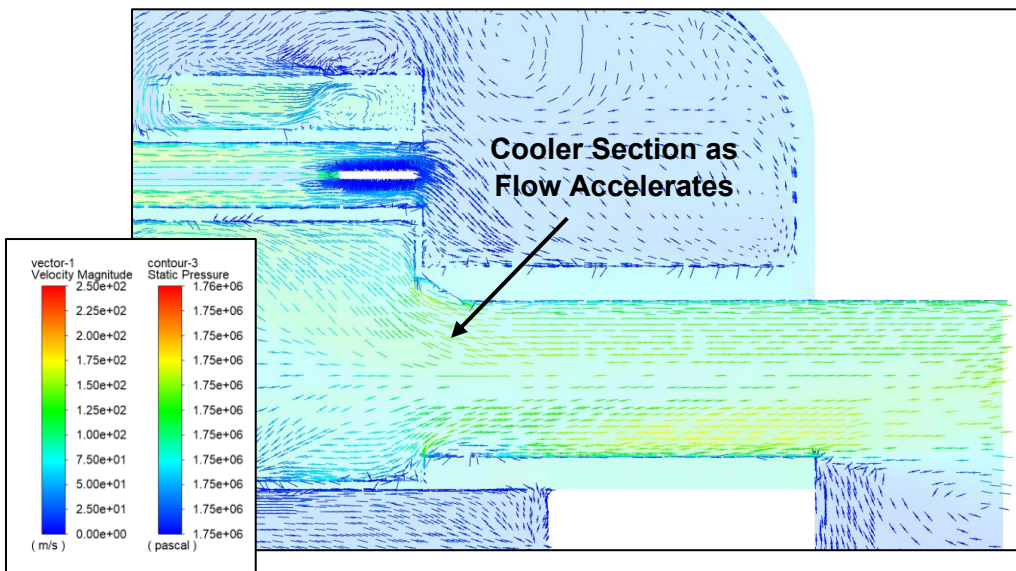


Figure 4-13: Velocity Vector & Temperature Overlay Close-Up

The next section of overlaid contour images are the velocity vectors with the pressure contour. This overlay confirms what was stated prior regarding the stagnant portion of the combustion chamber where the flow traveling through the combustion chamber would push into the front of the outer combustion chamber this is seen in Figure 4-14

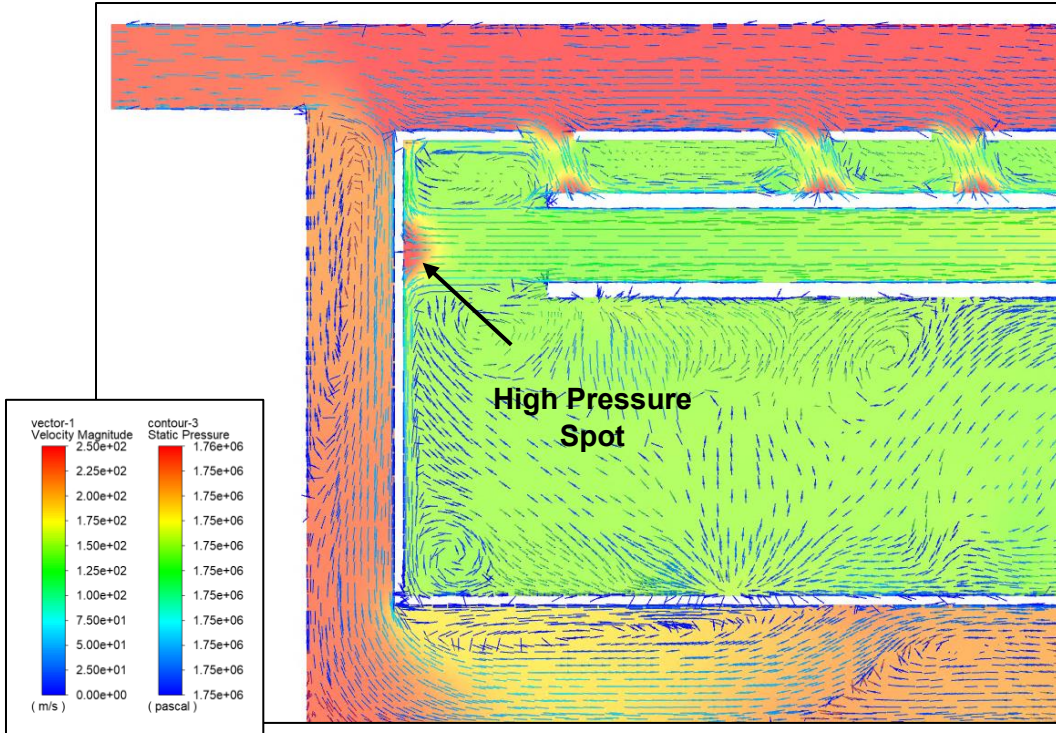


Figure 4-14: Velocity Vector & Pressure Overlay Close-Up

#### 4.2. Simulation Results – Compared Models

With the focus areas identified on the baseline combustion chamber, the focus is to be shifted to the differences between the models. The changes to each of the models can be seen in Table 2-2. Before each section, a table showing the critical values for the compared models will be shown. The following contours will be related to the table shown to allow a visual representation of the data.

In each of the following figures, (a) will indicate the original baseline model. (b) will indicate the model with a larger combustion chamber fluid domain inlet. Finally (c) will indicate the model with a closed off hole flowpath entrance. All models in this section are contoured to the same range to allow for visual comparison.

##### **Model Comparison – Velocity Contours & Vectors:**

The results for velocities within each model of the combustion chamber can be seen in

Table 4-1. The results to note for this table are the overall averages and maximums for the open Flowpath and closed Flowpath models. The maximum velocity for both of these models at the outlet and fluid region is higher than for the base model. Despite this, they have a lower average velocity in both cases. This indicates that despite the areas of higher velocity there is a sufficient amount of areas with lower velocities to bring the average down.

Table 4-1: Model Results – Velocity

Location	Property	Datum	Base Model	Larger Flowpath	Closed Flowpath
Inlet	Velocity (m/s)	Max Vertex	75.33705	75.33705	75.33705
		Average	75.33705	75.33705	75.33705
Outlet	Velocity (m/s)	Max Vertex	249.1226	264.64	269.8085
		Average	113.104	112.749	112.16755
Fluid Region	Velocity (m/s)	Max	351.84861	356.2823	382.1
		Average	55.656741	55.169905	55.0812

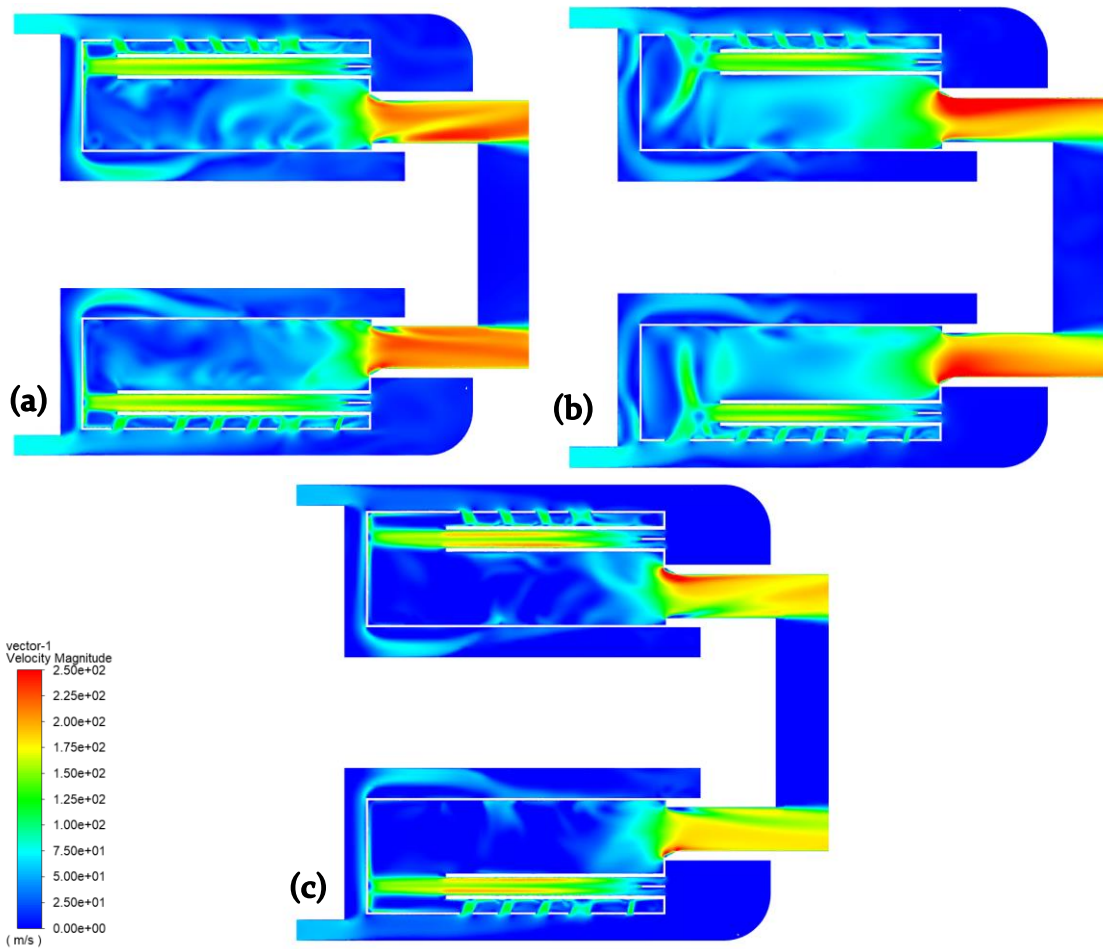


Figure 4-15: Velocity Contour Model Comparison: (a) baseline model, (b) larger flowpath model, (c) closed flowpath model

Starting with the same contour as the baseline model, velocity contours between the models can be seen in Figure 4-15. The primary changes to be focused on for these models are the changes to the amount of accelerated flow moving through the inner combustion chamber, the velocity of the flow moving out of the outlet and the stagnation of flow moving through around the vaporizing tubes.

The most apparent changes between these models is when approaching the outlet of the model. Both the original model (a) as well as the closed flowpath model (c) show a more uniform exit velocity along the fluid domain. This is likely due to the amount of flow that enters the inner combustion chamber which would then reenter the outer combustion chamber closer to the center of the engine. This would cause accelerated flow to remain close to the center of the combustion chamber and create a more uniform flow. The open flowpath model (b) shows a much more focused velocity increase towards the outer walls of the combustion chamber when moving towards the outlet. This is due to the reduced flow moving through the inner combustion chamber which causes this nonuniformity. This nonuniformity causes the models to have a higher maximum velocity but when comparing the average velocity of the outlet the change is minor (Table 4-1). However, this accelerated flow located on the edge of the outlet would be the flow most impacted by the turbine stage following the combustion chamber.

#### **Base Model vs Larger Flowpath Model (b):**

The changes to the model velocity become immediately apparent when looking at the areas of modified geometry. In image (b) of Figure 4-15 the heavily directed flow in the original model that was impinging the front wall of the outer combustion chamber is instead being redirected towards the inner combustion chamber by the increased flow from the first holes of the combustion chamber. This effect can clearly be seen in Figure 4-16. In Figure 4-17, the result of this change can be seen as large vorticities forming in the combustion chamber. This will aid turbulence within the engine as well as force the fuel rich mixture from the vaporizing tubes deeper in to the engine. This condition will result in a higher overall temperature within the engine as the fuel rich mixture is spread more evenly through the combustion chamber.

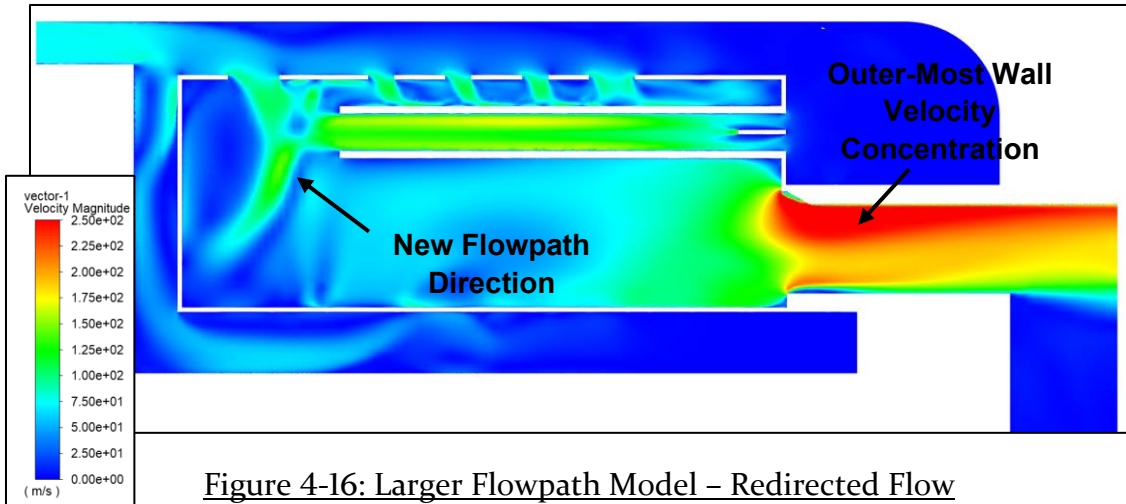


Figure 4-16: Larger Flowpath Model – Redirected Flow

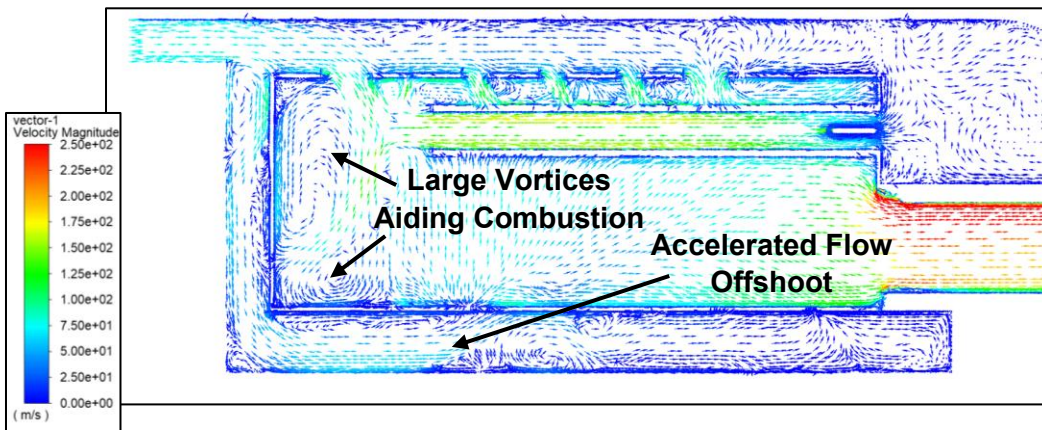


Figure 4-17: Larger Flowpath Model – Vorticity

The accelerated offshoot of flow that enters the inner combustion chamber is still present within the larger flow path model. This accelerated flow offshoot appears to have a correlation with the amount of pressure being seen in the inner combustion chamber due to the amount of stagnant flow it causes. In Figure 4-18 the highly directional flow from the baseline model as it follows the shroud appears to be less efficient. This is assumed to occur due to the momentum of the flow being redirected towards the outer combustion chamber earlier.

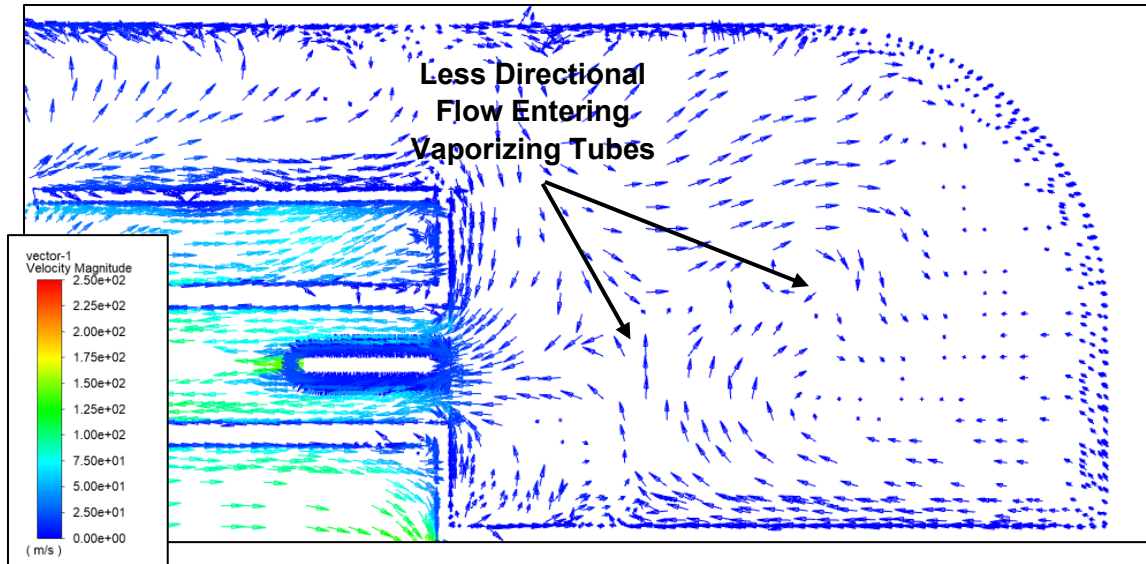


Figure 4-18: Larger Flowpath Model – Less Directional Flow

### **Base Model vs Closed Flowpath Model (c):**

Upon inspection, the modified geometry immediately shows a change in the flowpath of the velocity vectors. The first immediate change is the redirection of more flow through the inner combustion chamber at the initial flow divergence. Compared to the base model, it is apparent there is additional flow that will cause an increased stream of gases to enter the outer combustion chamber from the inner combustion chamber shown in Figure 4-20. In addition, this increase in flow moving through the inner combustion chamber will cause a further increase in the pressure caused by redirecting flow reducing engine efficiency.

Due to the lack of flow from the first layer of holes in the combustion chamber, the issue of the accelerated flow from the vaporizing tubes pressing into the front of the combustion chamber wall persists, although with the shortened tube, the flow has some time to slow down before reaching the wall (Figure 4-19). This allows the flow to be more easily redirected and it creates large vortices along the wall. Seen in Figure 4-21, the directional flow following the combustion chamber shroud persists from the original model which is different from the larger flowpath model. This is likely due to the flow not being sapped from the first layer of holes in the combustion chamber and being accelerated over the outer combustion chamber walls.

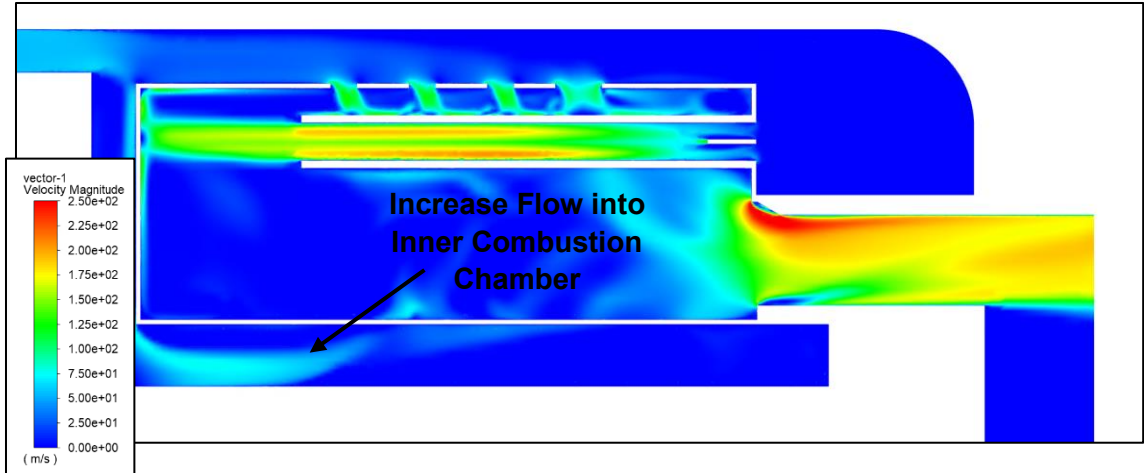


Figure 4-19: Closed Flowpath Model - Redirected Flow

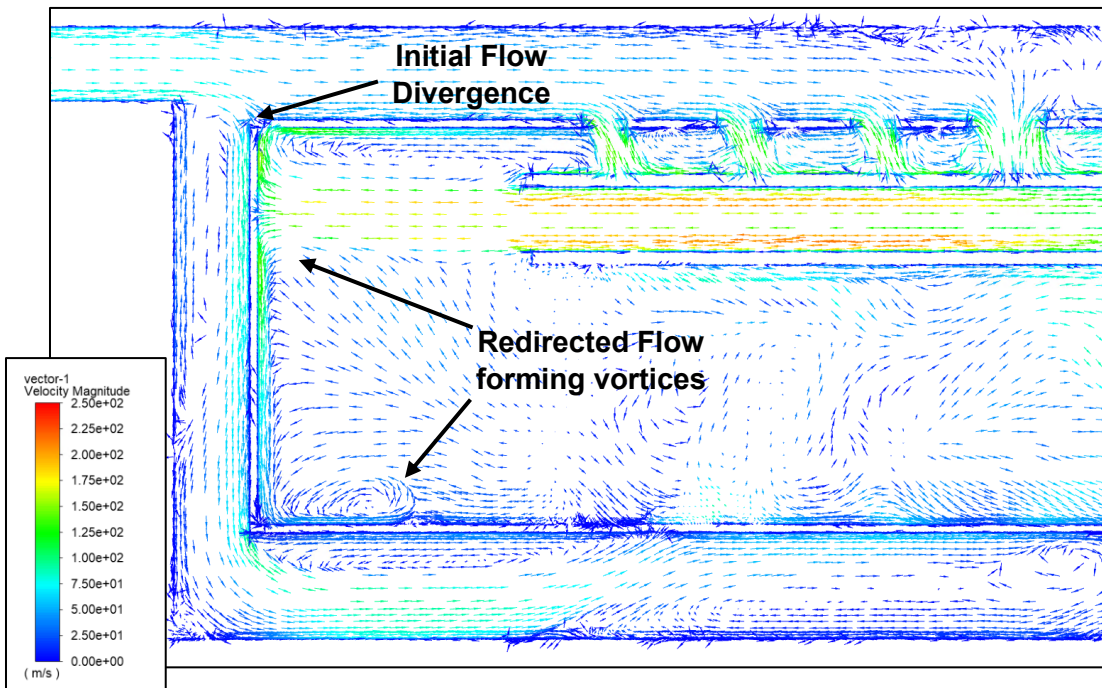


Figure 4-20: Closed Flowpath Model - Flow Divergence



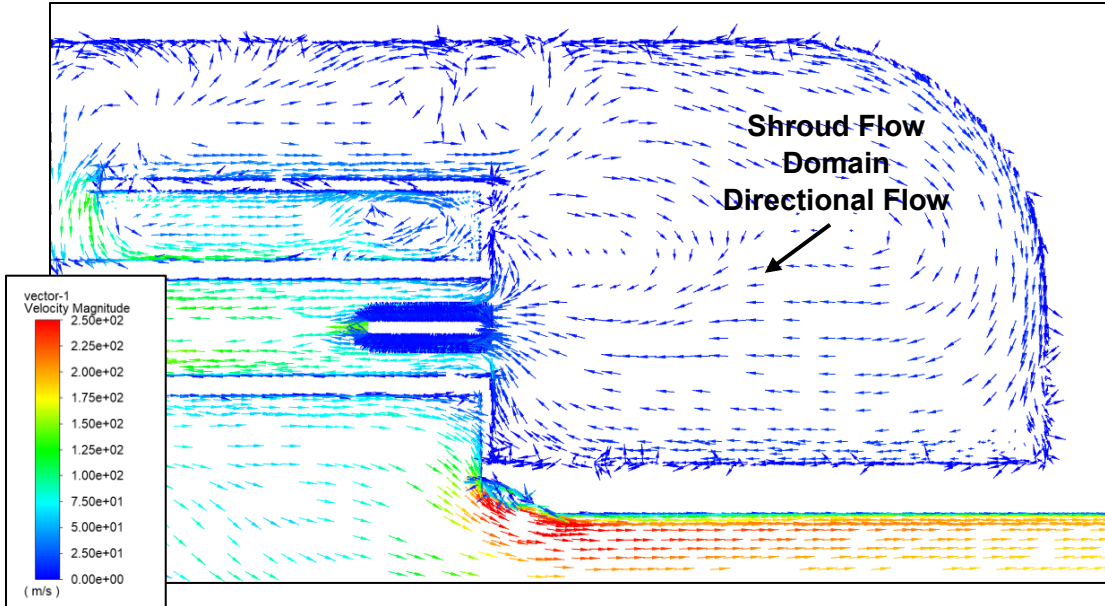


Figure 4-21: Closed Flowpath Model – More Directional Flow

**Model Comparison – Pressure Contours:**

The next area of comparison is the pressure values of the models. The recorded values for each model would be looking at the calculated pressure drop for the engine. The main pressure drop to be observed is the pressure drop across the entire combustion chamber. Ideally the combustion process is an isobaric one, so aiming for the maximum efficiency possible the goal is to have the smallest pressure drop. The model with the lowest pressure drop was the Larger Flowpath model with a pressure drop of 12.68 kPa. This is compared to the pressure drop of the baseline model of 15.39 kPa. This is due to the Larger Flowpath model having removed the critical areas of stagnant flow and pressure concentrations along the engine within the inner combustion chamber and front of the outer combustion chamber.

Table 4-2: Model Results – Pressure

Location	Property	Datum	Base Model	Larger Flowpath	Closed Flowpath
<b>Inlet</b>	Pressure (kPa)	Average	189.389	186.679	190.139
<b>Outlet</b>	Pressure (kPa)	Average	173.999	173.999	173.999
		Drop Average (Inlet vs. Outlet)	-15.39	-12.68	-16.14
<b>Fluid Region</b>	Pressure (kPa)	Average	177.909	176.329	178.489
		Drop Average (Full Chamber)	-3.91	-2.33	-4.49

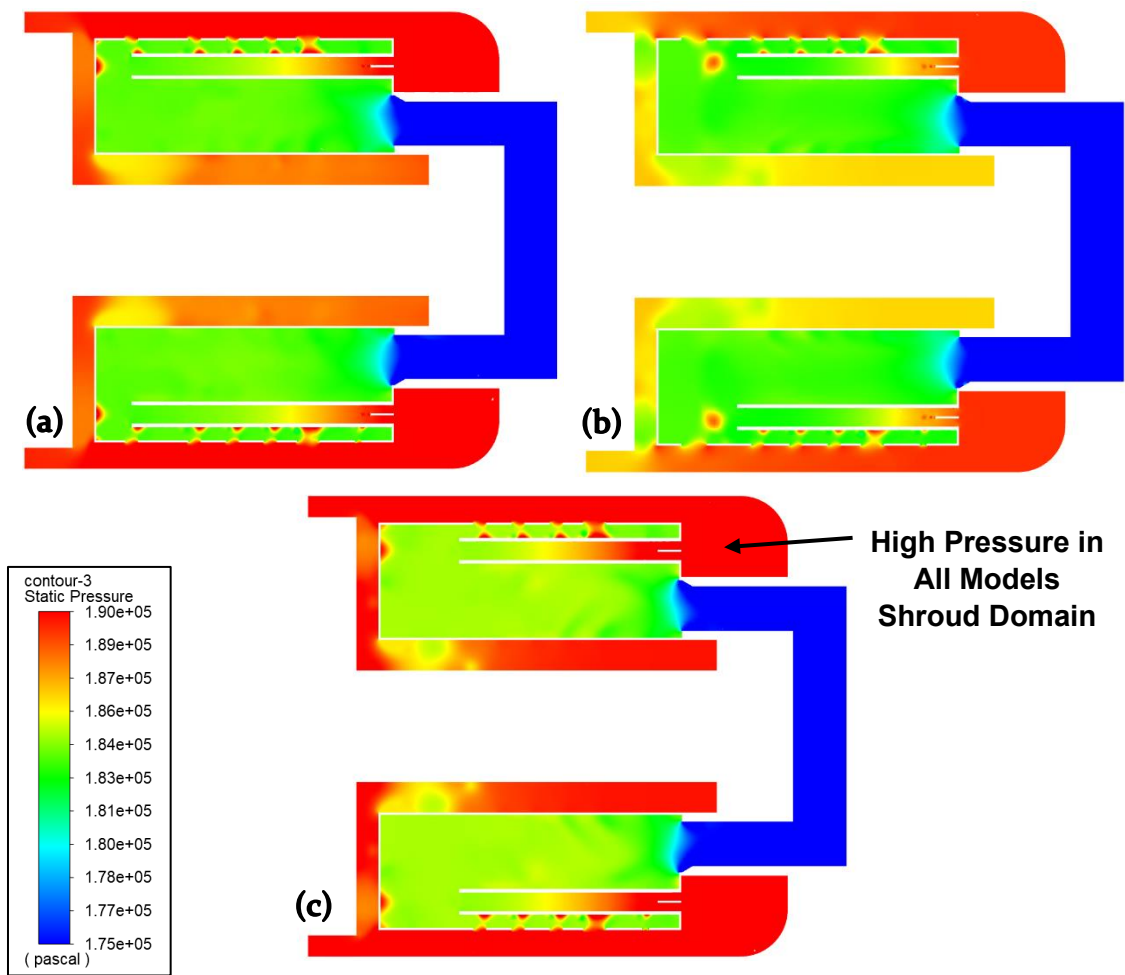
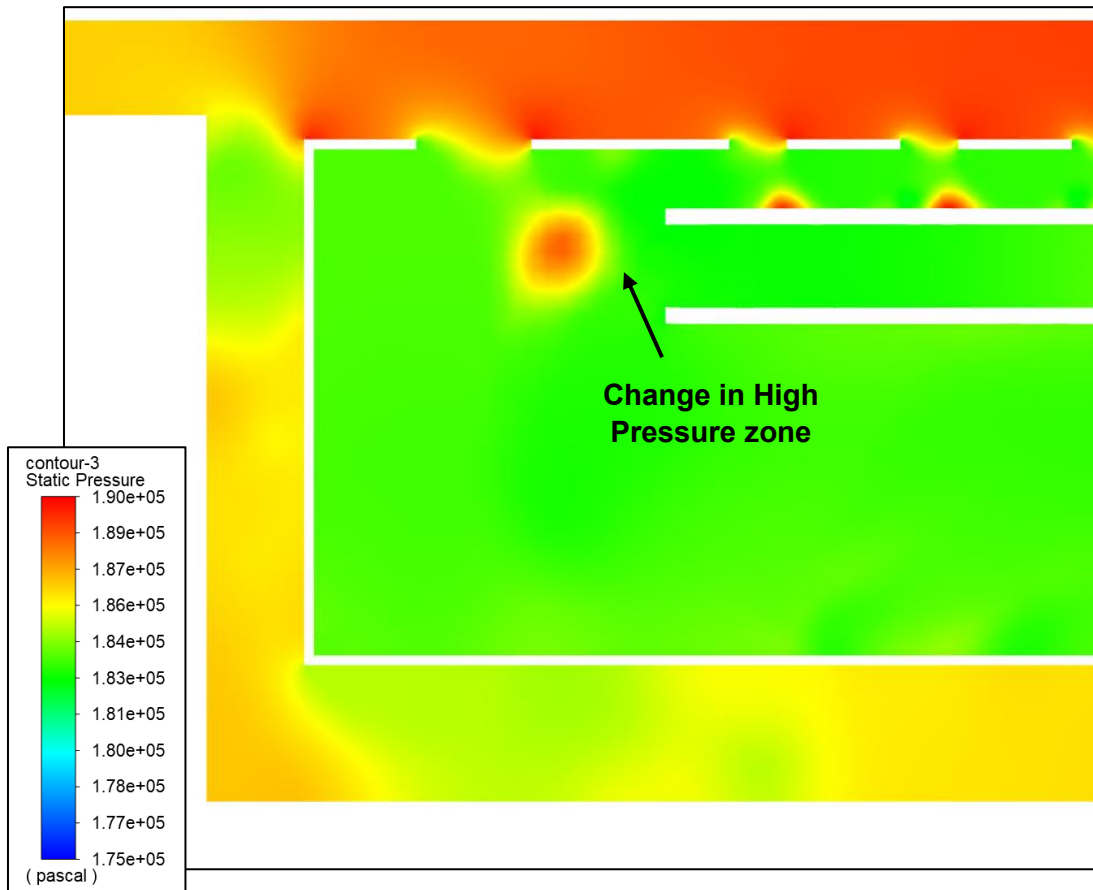


Figure 4-22: Pressure Contour Model Comparison: (a) baseline model, (b) larger flowpath model, (c) closed flowpath model

Overall the pressure contour was very similar between the models with some key changes in the inner combustion chamber and in front of the vaporizing tubes seen in Figure 4-22. The result that is the same between all three models is the area of the shroud flow domain, this area of the analysis is where a large amount of improvement can be made with additional geometric changes. Changes to the shroud flow domain to alleviate the pressure increase from redirected flow through the vaporizing tubes would allow for less of a pressure drop in the combustion chamber.

**Base Model vs Larger Flowpath Model (b):**

The most noticeable change between the baseline model and the larger flowpath model is the location of high pressure leaving the vaporizing tubes. As stated for the base model there was an area of increased pressure that caused the flow to stagnate at the front of the combustion chamber. Now, with the larger flowpath holes and reduced length of the vaporizing tubes, the pressure increase shows up away from the wall, where the flow from the combustion chamber hole and the vaporizing tube connects and become redirected (Figure 4-23).



**Figure 4-23: Larger Flowpath Model – Pressure Zone**

With the larger flowpath model, there is a noticeable reduction in pressure within the inner combustion chamber. This can be seen in Figure 4-24. This is an expected result due to the decreased flow running through the inner combustion chamber and increase in flow running through the first row of holes in the combustion chamber. Less flow being pressed in this location resulted in reduction of pressure in this area. This reduction will help with the overall pressure drop in the combustion chamber and improve thermal efficiency of the engine.

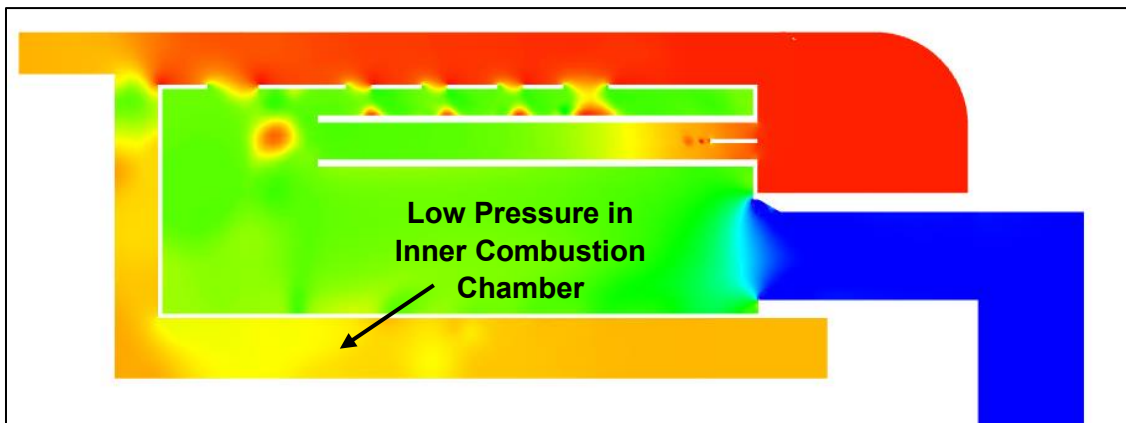


Figure 4-24: Larger Flowpath Model - Lower Pressure Inner Combustion Chamber

#### **Base Model vs Closed Flowpath Model (c):**

Without the additional flow coming from the first pattern of holes in the combustion chamber, the accelerated flow from the vaporizing tubes is pressed into the front of the combustion chamber walls. However, as the vaporizing tubes were shortened, this accelerating flow has time to slow down before hitting the combustion chamber wall which results in a lower pressure build up in this area. See Figure 4-25.

Also of note is the increased pressure within this model of the combustion chamber. This is especially noticeable when looking at the inner combustion chamber and is caused by the increased amount of flow being directed in this direction. The flow is being pressed into the back of the inner combustion chamber area causing a high pressure zone as seen in Figure 4-26.

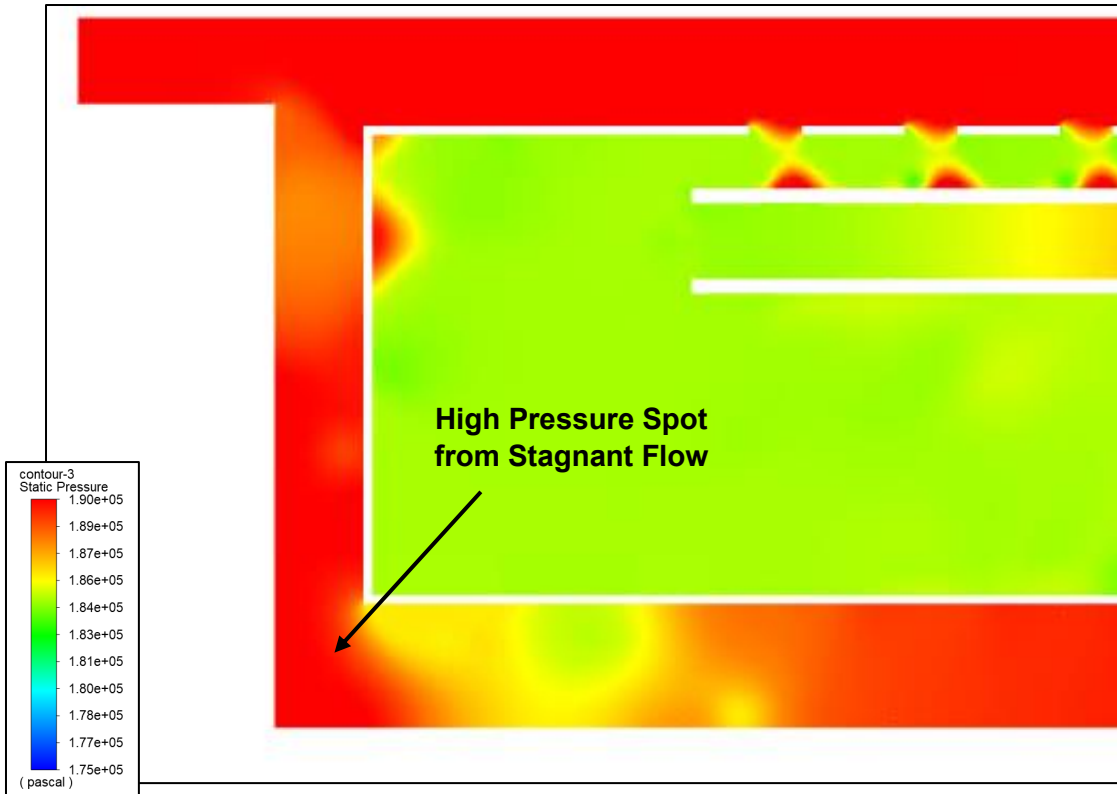


Figure 4-25: Closed Flowpath Model – High Pressure Zone

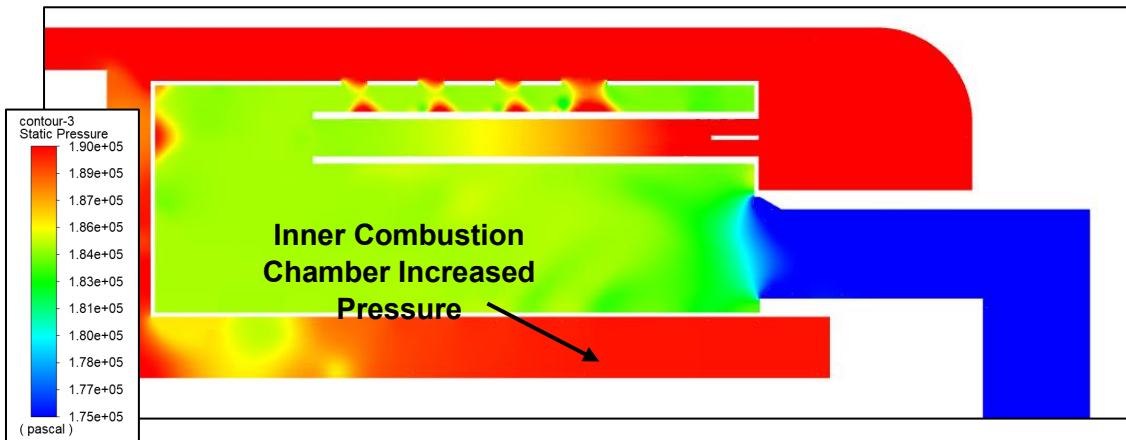


Figure 4-26: Closed Flowpath Model – High Pressure Inner Combustion Chamber

**Model Comparison – Temperature & Oxygen Mass Fraction Contours:**

The temperature results of the combustion chamber show that each of the geometric changes to the turbine engine display a temperature increase. This is indicated by both the maximum value as well as the average values of temperature. The model with the largest increase in temperature was the open Flowpath model.

Shown in Table 4-3, the maximum temperature in the fluid region of the combustion chamber for the open Flowpath model was displayed as 2365K. The higher temperature in this model will lead to an increase in thermal efficiency, but caution must be given to the potential degradation of material at these increased temperatures.

The temperature at the outlet of the model gives a better picture as to what is happening in the combustion chamber despite these higher fluid region temperatures. The average temperature in each of the model for the outlet is very similar, only a difference of 4.57K between the minimum and maximum values. This indicates that despite the increase in temperature in the combustion chamber there is enough cooling before reaching the outlet to not heavily impact the turbine.

The temperatures of the wall conditions are also of concern for these models. There is a noticeable increase in the Larger Flowpath model, but this increase is likely manageable due to the structural strength of steel at 655.4K being at approximately 90% of its strength compared to steel at 294.15K. The temperature of the Closed Flowpath model however would likely not be manageable at 864.22K as the structural strength of steel at this temperature is approximately 30% (The Engineering Toolbox, 2008).

Table 4-3: Model Results – Temperature

Location	Property	Datum	Base Model	Larger Flowpath	Closed Flowpath
Outlet	Temperature (K)	Max Vertex	1430.39	1607.12	1608.66
		Average	639.03	640.4	643.6
Fluid Region	Temperature (K)	Max	2281.42	2365	2300.14
		Average	868.8	891.6	844.04
Combustion Chamber Solid	Temperature (K)	Max Vertex	1051.76	1552.28	1163.06
		Min Vertex	311.39	320.31	448.36
		Average	589.9	655.4	864.22

The comparison of the temperature contours became rather critical as it is one of the primary foci of this project. Figure 4-27 has the compared models temperature contours side profile while Figure 4-29 presents a front profile of the turbine engine contours.

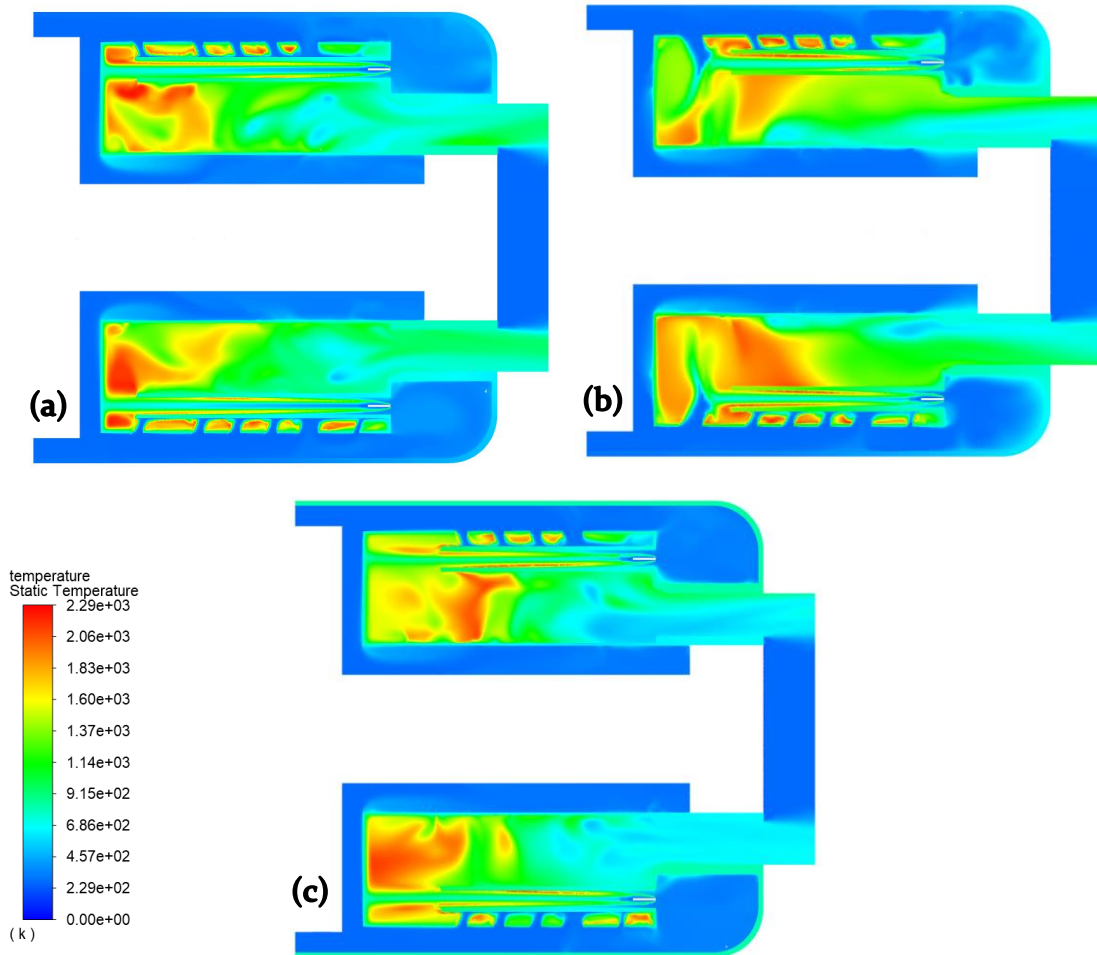


Figure 4-27: Temperature Contour Model Comparison – Side Profile: (a) baseline model, (b) larger flowpath model, (c) closed flowpath model

The apparent difference between the three configurations is the concentration of the high temperature flow within the combustion chamber. The model with the combustion chamber holes closed off (c) has the most concentrated area of heat focused near the outlet of the vaporizing tubes. The baseline model (a) has the heat mostly concentrated on the front of the combustion chamber while the larger flowpath model (b) has a much more uniform distribution of heat along the entire combustion chamber spreading further back into the engine.

More insight can be gained looking into the oxygen concentrations for each model. This can be seen in the concentration of oxygen between each model will give a proper view at where the combustion process is the most intense within the model. Areas of intense combustion will show a reduced or absent concentration of oxygen in the contour. The side profile contour results for the oxygen in the combustion chamber can be seen in Figure 4-28.

The difference in the combustion reactions of each model is made apparent when viewing the oxygen mass fraction contours. Changes of note are the changes in the closed Flowpath model (c) having that high concentration of combustion trapped in the front of the combustion chamber. The concentration of fuel rich mixture in this area is apparent due to the lack of oxygen that acts almost as a barrier between the rest of the flow. The distribution of the fuel rich mixture deep in to the combustion chamber from the open Flowpath model (b) is also readily apparent.

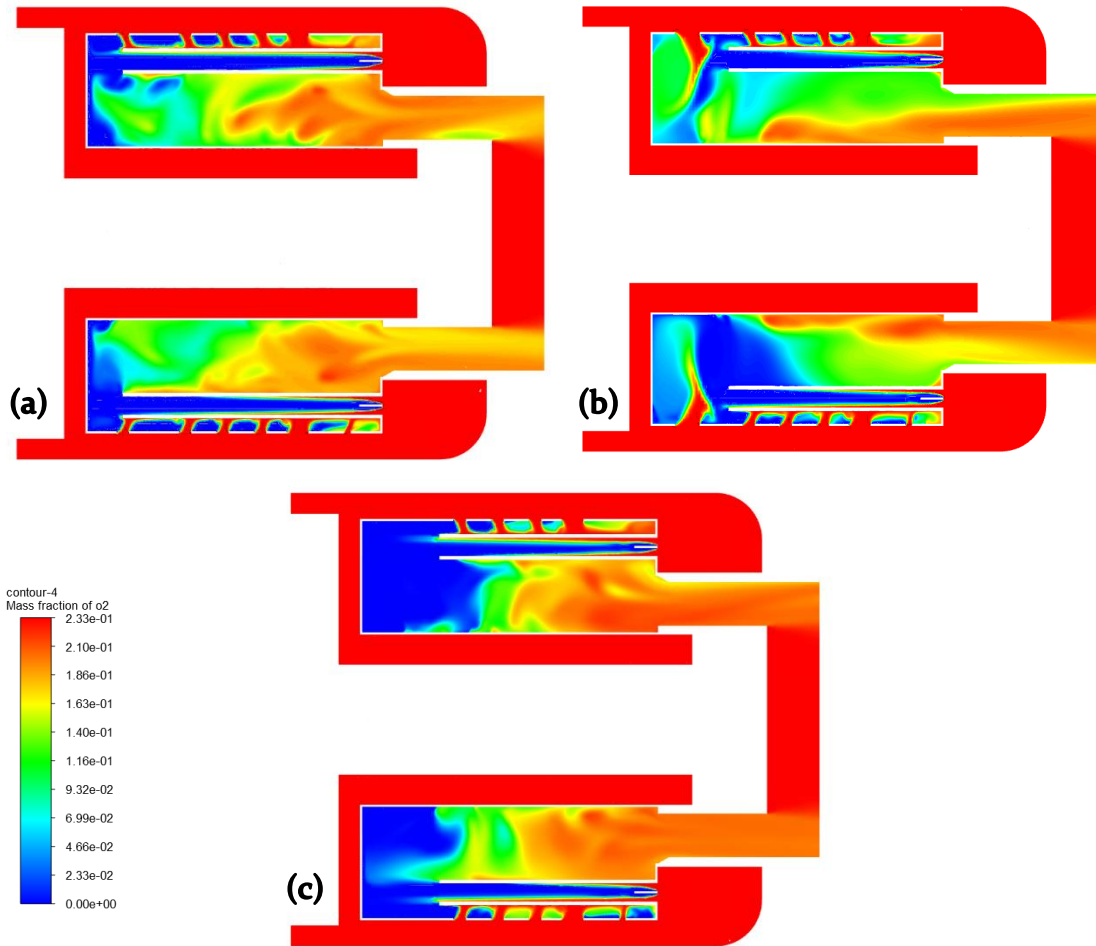


Figure 4-28: Oxygen Mass Fraction Contour Model Comparison – Side Profile: (a) baseline model, (b) larger flowpath model, (c) closed flowpath model

Figure 4-29 shows another angle of this high temperature distribution. The baseline model (a) has high temperature areas hugging the outside walls of the outer combustion chamber, which the closed flowpath model (c) is also following this pattern. The open flowpath model (b) shows more temperature distribution and has the high temperatures reaching deeper in to the model.



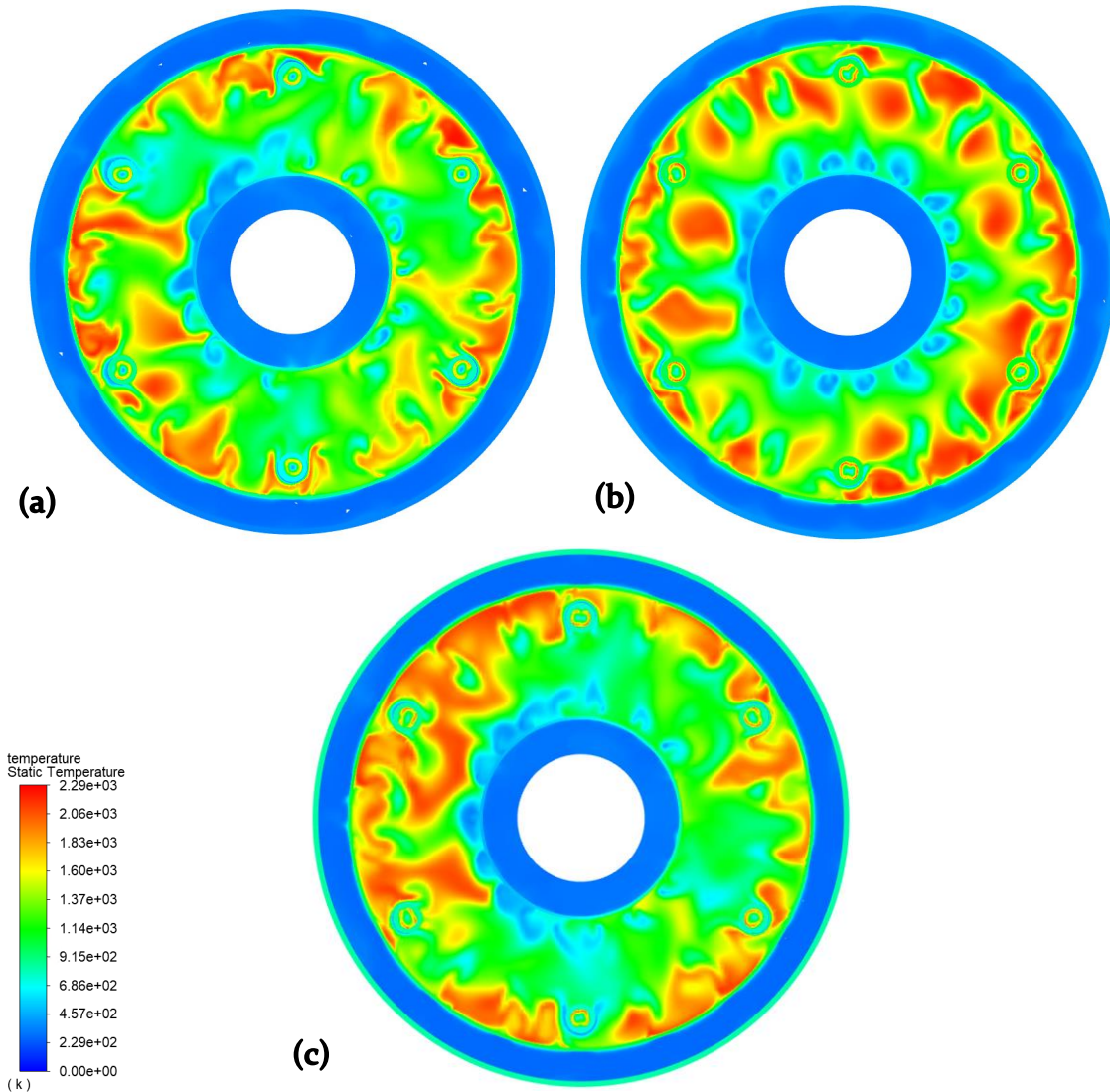


Figure 4-29: Temperature Contour Model Comparison – Front Profile: (a) baseline model, (b) larger flowpath model, (c) closed flowpath model

Figure 4-30 presents the oxygen mass fraction concentration from a head on view of the engine. This view shows the overall increase in fresh air moving through the inner combustion chamber for the open Flowpath model (b) where there is a limited and less uniform injection of this fresh air coming from the base model (a) and closed flowpath (c) model.

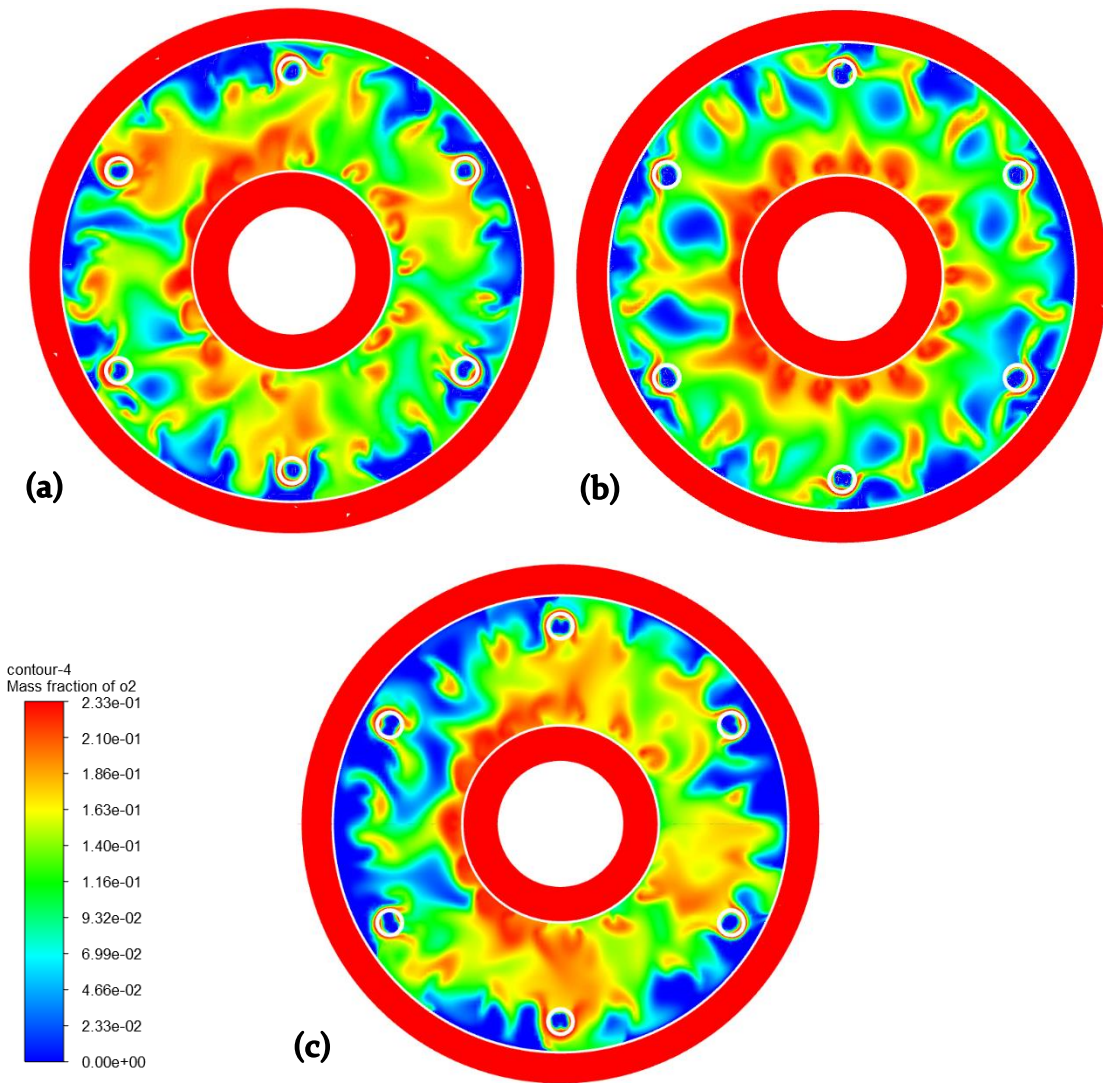


Figure 4-30: Oxygen Mass Fraction Contour Model Comparison – Front Profile: (a) baseline model, (b) larger flowpath model, (c) closed flowpath model

**Base Model vs Larger Flowpath Model (b):**

The changes from the larger flowpath model become apparent when focusing the attention on where the hottest temperatures of the model are occurring. Due to the higher amount of flow coming from the initial holes in the combustion chamber, the flame is being pushed towards the center of the combustion chamber. This will cause a more equal distribution of the high temperature areas throughout the engine causing the domain to heat up on average. This will also cause the heating of the combustion chamber walls that was seen in Table 4-3. Additionally, the flame is also expanding to a greater degree due to the vortices created from the increased

turbulent flow. The effect that the increased flow had on the combustion chamber temperature distribution can be seen in Figure 4-31.

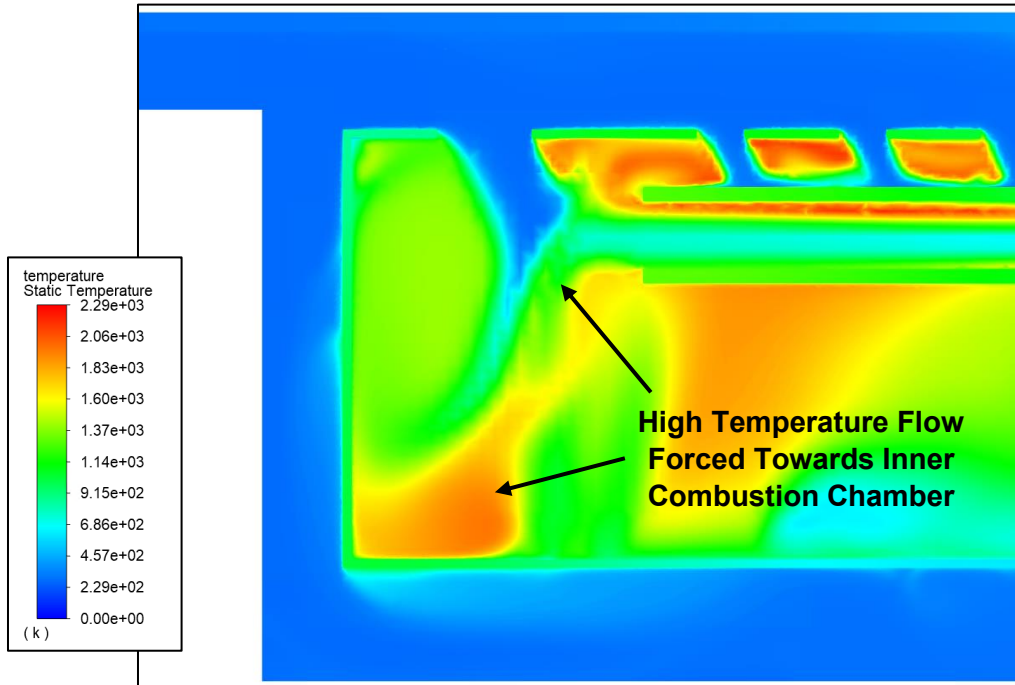


Figure 4-31: Temperature Contour Penetrating Flow

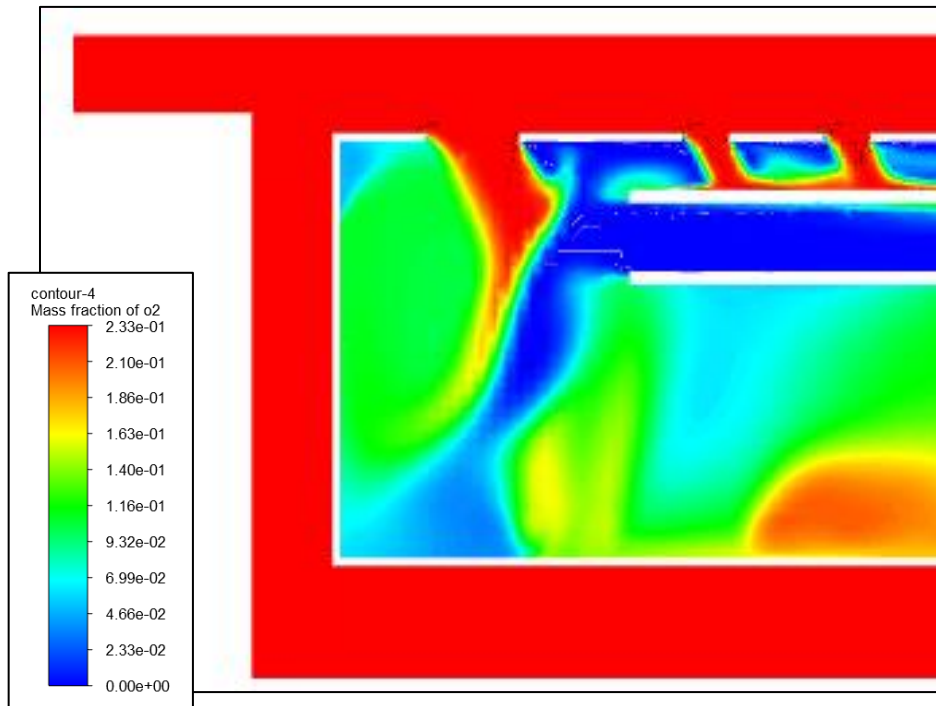


Figure 4-32: Oxygen Contour Penetrating Flow

The effect of this increased flow moving towards the inner combustion chamber can be seen in the front view contour as well. Seen in Figure 4-33 the hot spots of the combustion chamber are more evenly distributed than in the original model. When comparing this figure to the mass fraction of oxygen in Figure 4-34 the cooling fresh air coming from the inner combustion chamber is more apparent. The coldest sections of the outer combustion chamber are found where the fresh oxygen is being supplied from the inner combustion chamber.

The cooling that is happening due to this increase in fresh air coming from the inner combustion chamber is a key improvement to the larger Flowpath model. This additional flow is what allows the engine to run at a higher temperature without dramatically increasing the temperature of the outlet. This is a key factor to improving the efficiency of the combustion chamber.

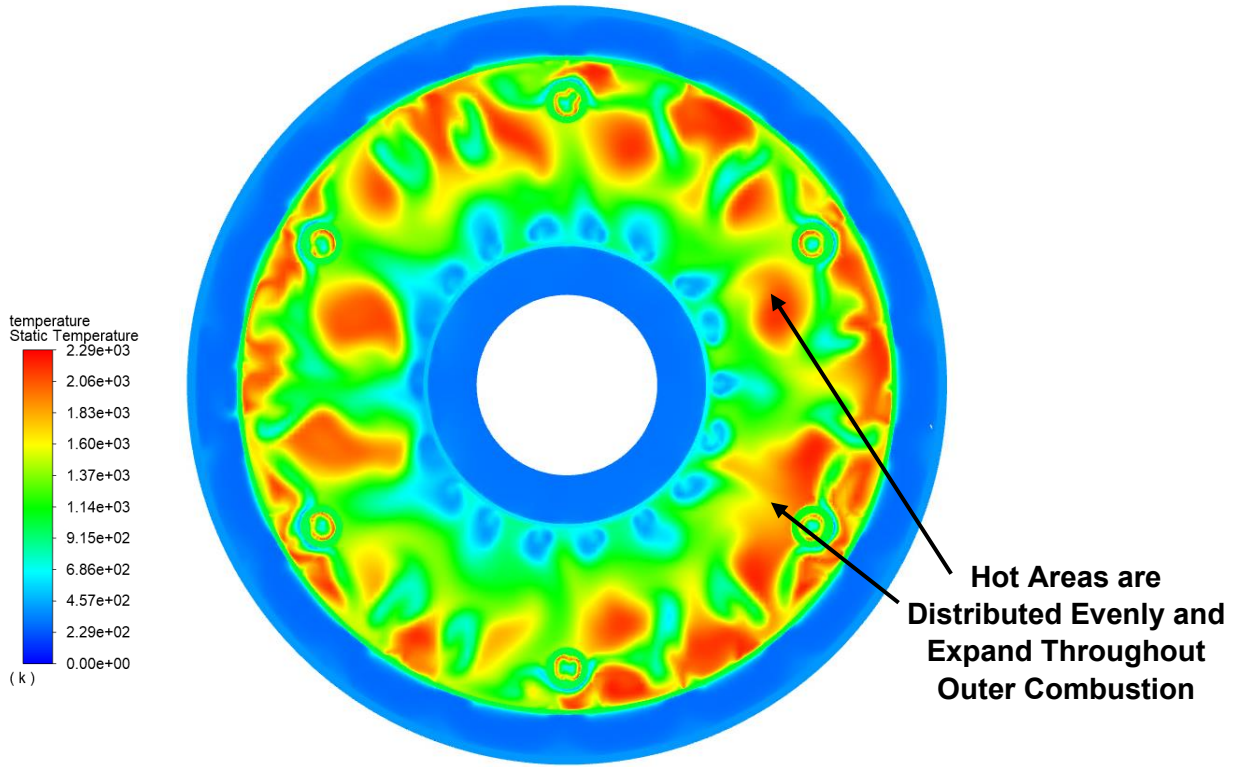


Figure 4-33: Distributed Temperatures

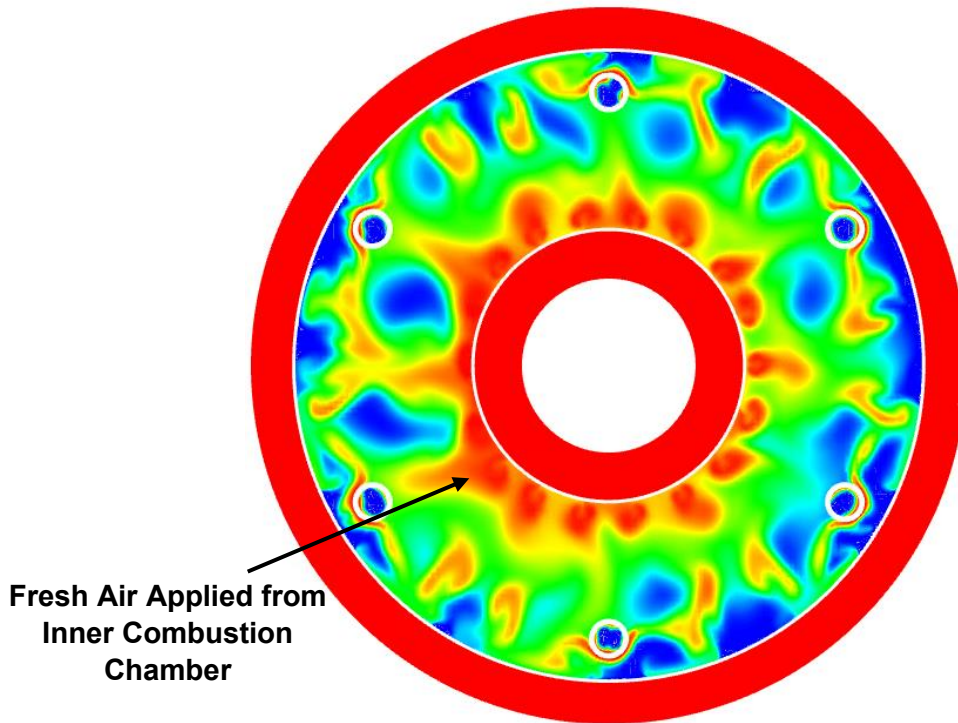
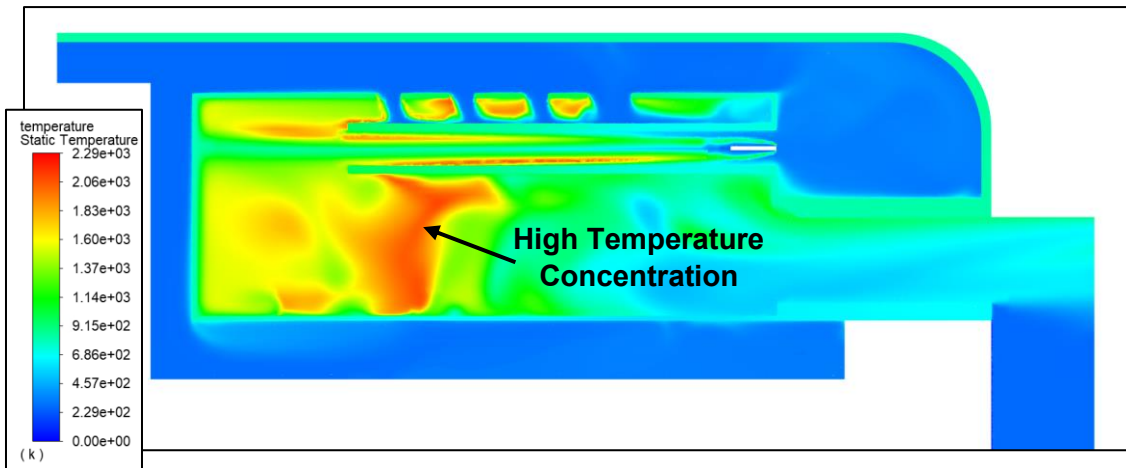


Figure 4-34: Open Flowpath Oxygen Distribution

**Base Model vs Closed Flowpath Model (c):**

As mentioned previously, the closed flowpath model (c) has a much higher concentration of high temperature flow around the outlet of the vaporizing tubes as seen in Figure 4-35. This appears to be caused by the increased flow coming from the inner combustion chamber as well as the removal of the first set of perforated holes causing the flow to move much slower in this area.



**Figure 4-35: Closed Flowpath Model – Temperature Concentration**

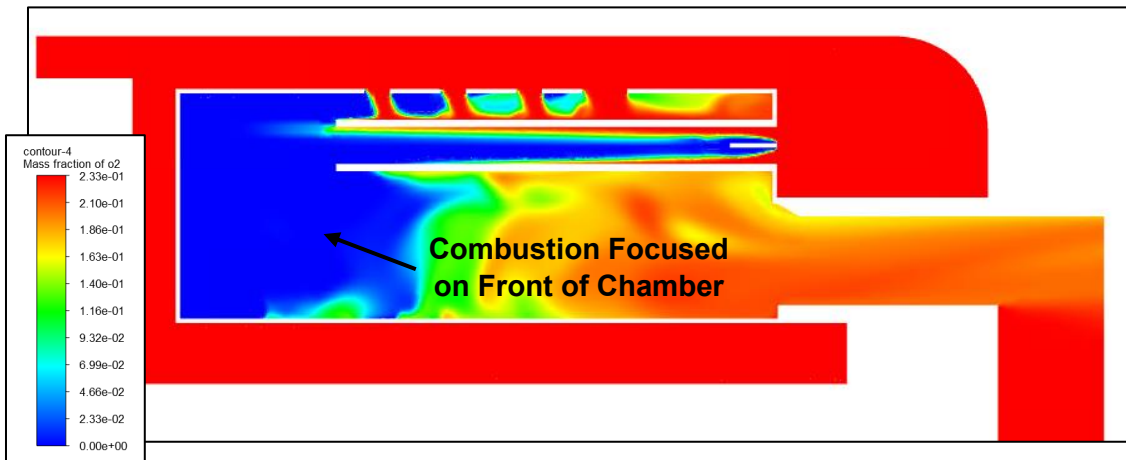


**Figure 4-36: Closed Flowpath Model – Temperature Concentration**

### Model Comparison – Temperature Contour Overlay:

The comparison evaluated next is related to the temperature and velocity contours overlays for each model as seen in Figure 4-37. The overlay between these models is useful to press upon some of the phenomenon already discussed in the previous models. From the overlay of temperature and velocity vectors is becomes clear that the hot spots within each model can be associated to the change in the flow circulation.

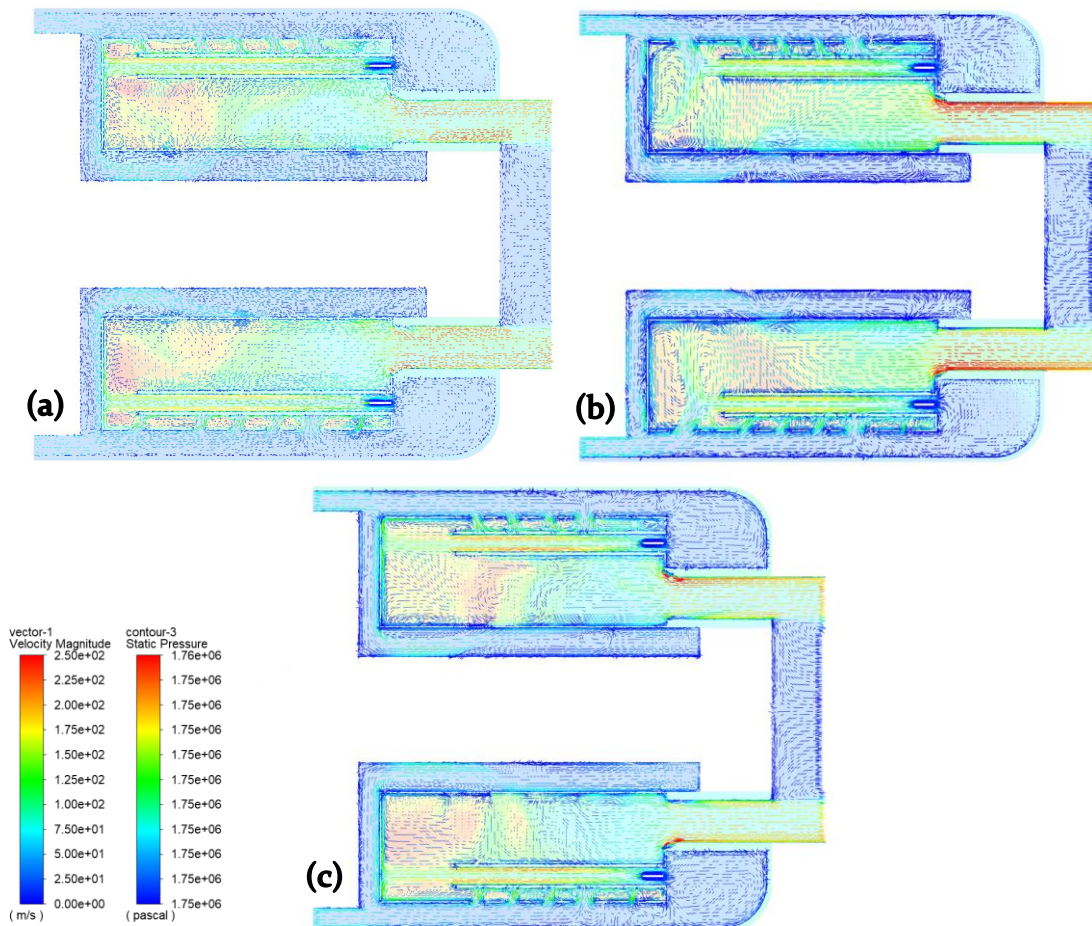
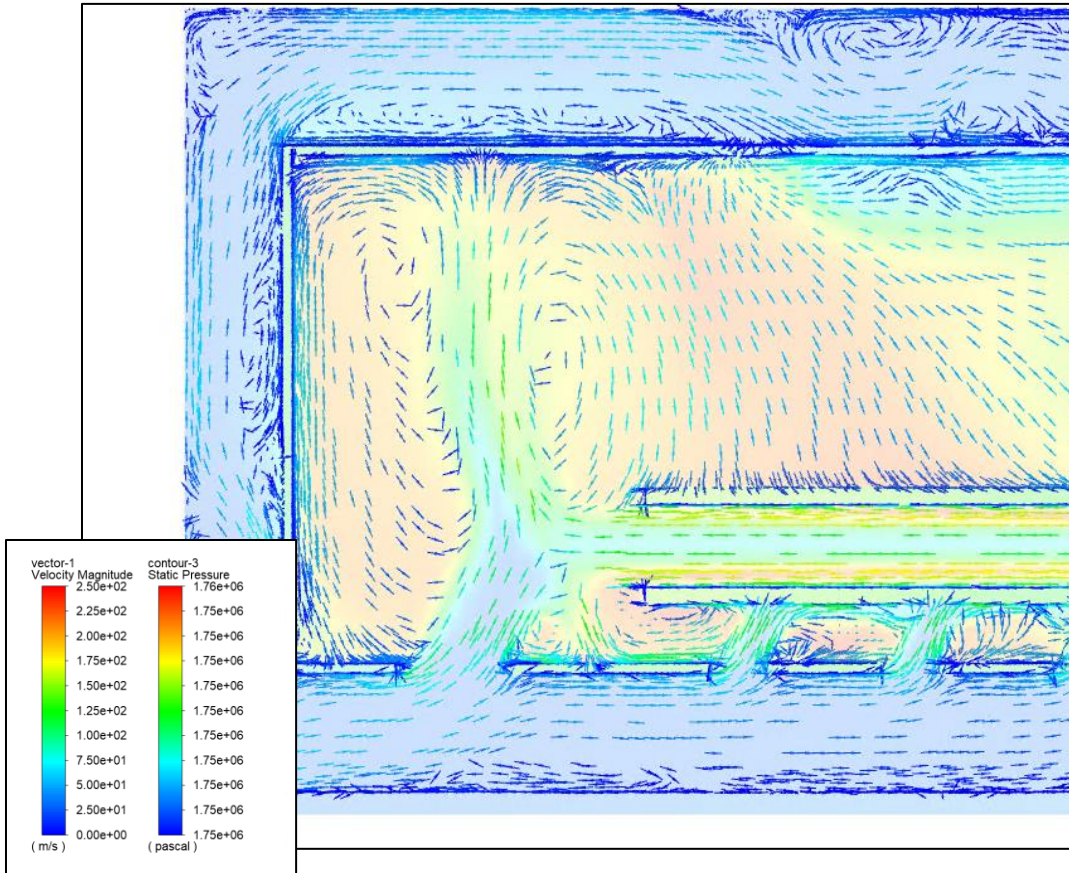


Figure 4-37: Temperature and Velocity Vector Overlay Comparison: (a) baseline model, (b) larger flowpath model, (c) closed flowpath model

### **Base Model vs Larger Flowpath Model (b):**

Within the larger flowpath model, the redirected flow which is moving towards the inner combustion chamber and causing circulation has the distributed hot spots following along the flow. This can be seen in Figure 4-38



**Figure 4-38: Open Flowpath Model – Circulation Temperatures**

### **Base Model vs Closed Flowpath Model (c):**

The more interesting phenomenon is with the closed flowpath model which shows the velocity vectors flowing from the inner combustion chamber and practically enclosing the high temperature areas with a stream of cold flow.



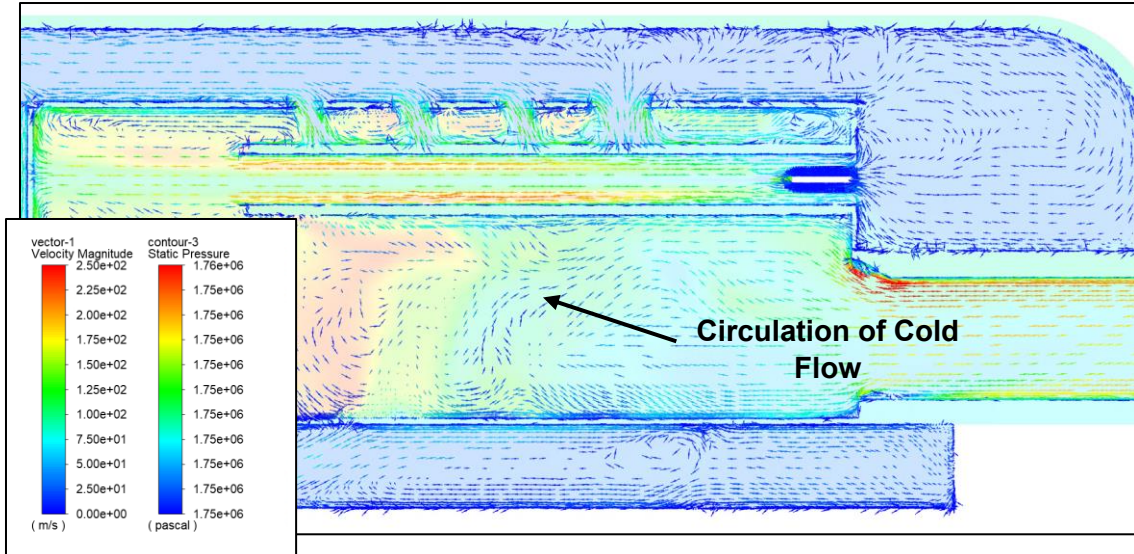


Figure 4-39: Closed Flowpath Model – Cold Flow Circulation

**Model Comparison – Pressure Contour Overlay:**

Figure 4-40 presents an overlay of the pressure and velocity vectors for each model. The overall pressure difference between these models is small but the velocity vector overlay can explain certain phenomena that are occurring.

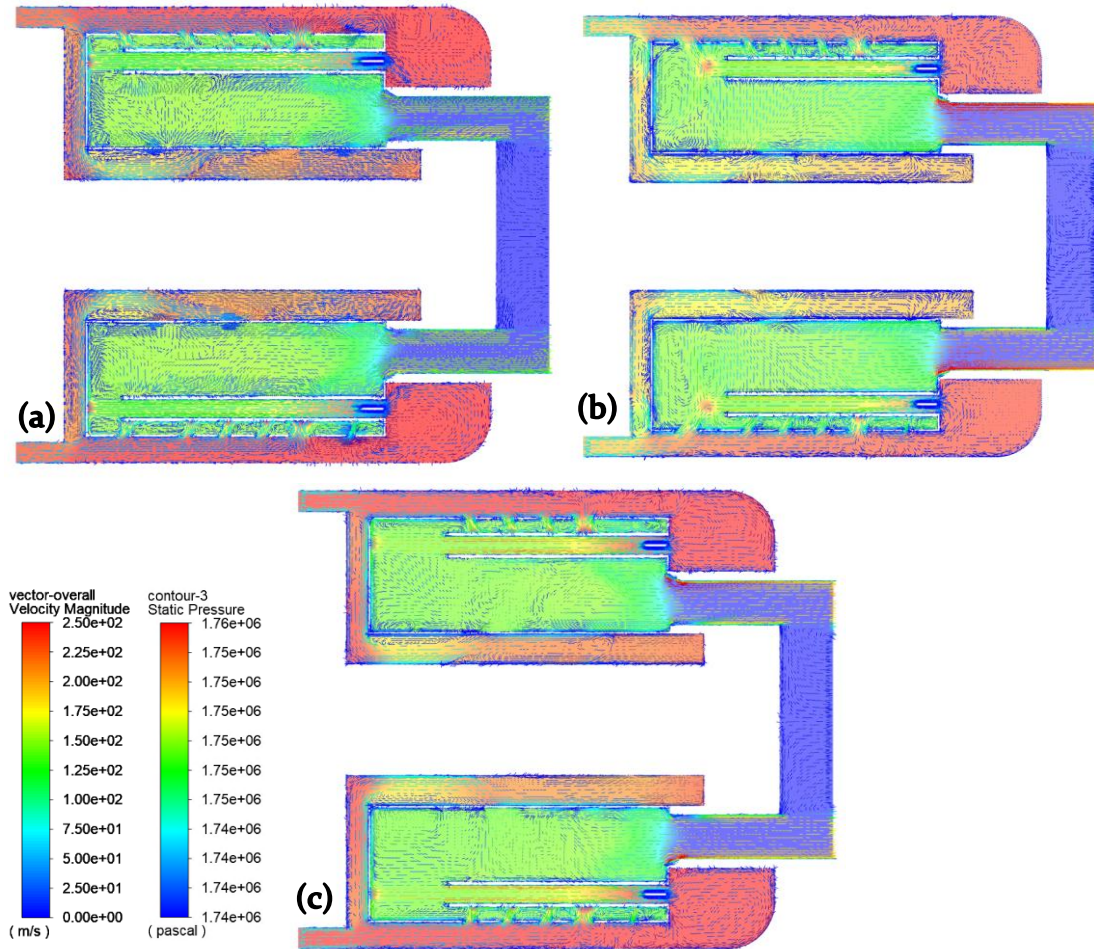


Figure 4-40: Pressure and Velocity Vector Overlay Comparison: (a) baseline model, (b) larger flowpath model, (c) closed flowpath model

### **Base Model vs Larger Flowpath Model (b):**

The main observation from the pressure contours is the pressure build-up in the larger flowpath model which forms in front of the vaporizing tubes instead of on the front of the combustion chamber walls. Figure 4-41 shows a closeup of the velocity vectors of two separate flows redirecting the vaporizing tube fluid domain to the inner combustion chamber. This redirection of flow causes a high-pressure area that is no longer pressed against the combustion chamber wall. This high pressure zone no longer being against the wall will reduce the potential for a hot spot avoiding the impedance of hot combustion chamber gasses.

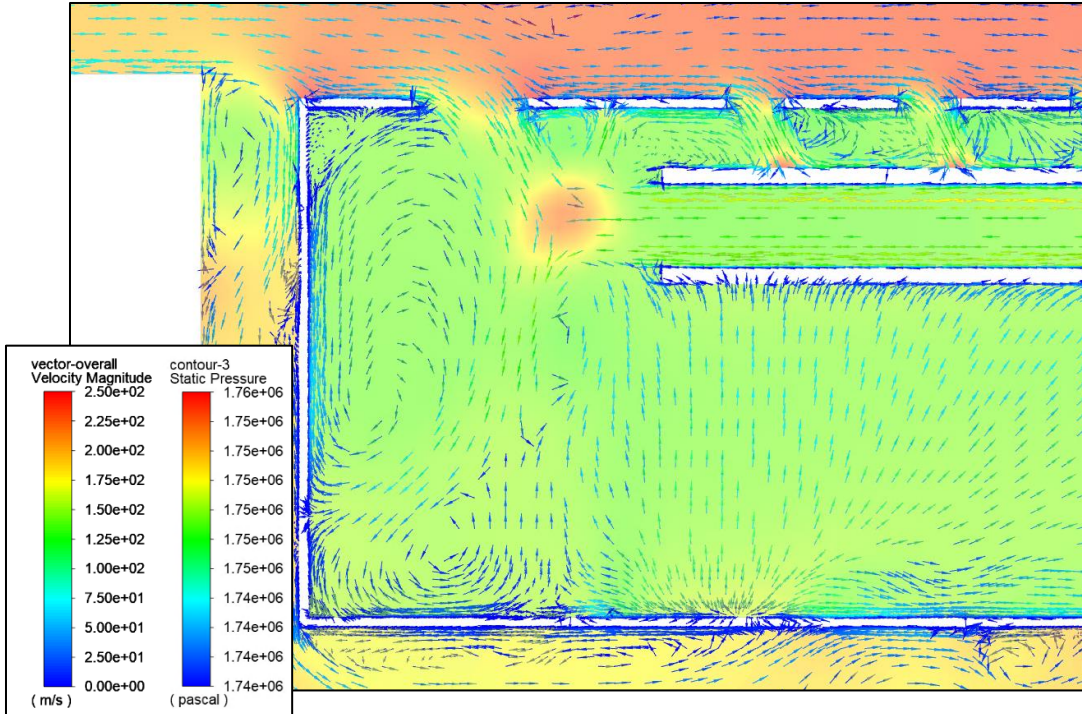


Figure 4-41: Larger Flowpath Model – Flow Interference

#### 4.3. Additional Observations – Turbulent Kinetic Energy

The turbulent kinetic energy is the next point of comparison. In Fluent, the turbulent kinetic energy is calculated using the Root-Mean-Square (RMS) of the fluctuating velocity terms. This will give an idea of how much variation there is in the model regarding the velocity at different locations in the model. Equations 4.1 and 4.2 present the turbulent kinetic energy used by Fluent (ANSYS Fluent, 2006) (Online, 2011).

$$k = \frac{\overline{u'_i u'_i}}{2} \quad 4-1$$

$$k = \frac{(\overline{u_x'^2} \overline{u_y'^2} \overline{u_z'^2})}{2} \quad 4-2$$

Table 4-4 shows the average results for turbulent kinetic energy within the combustion chamber between each model.

Table 4-4: Model Results – Turbulent Kinetic Energy

Model Results - Turbulent Kinetic Energy					
Location	Property	Datum	Base Model	Larger Flowpath	Closed Flowpath
Fluid Region	Average Turbulent Kinetic Energy	(m <sup>2</sup> /s <sup>2</sup> )	213.2	225.99	239.41

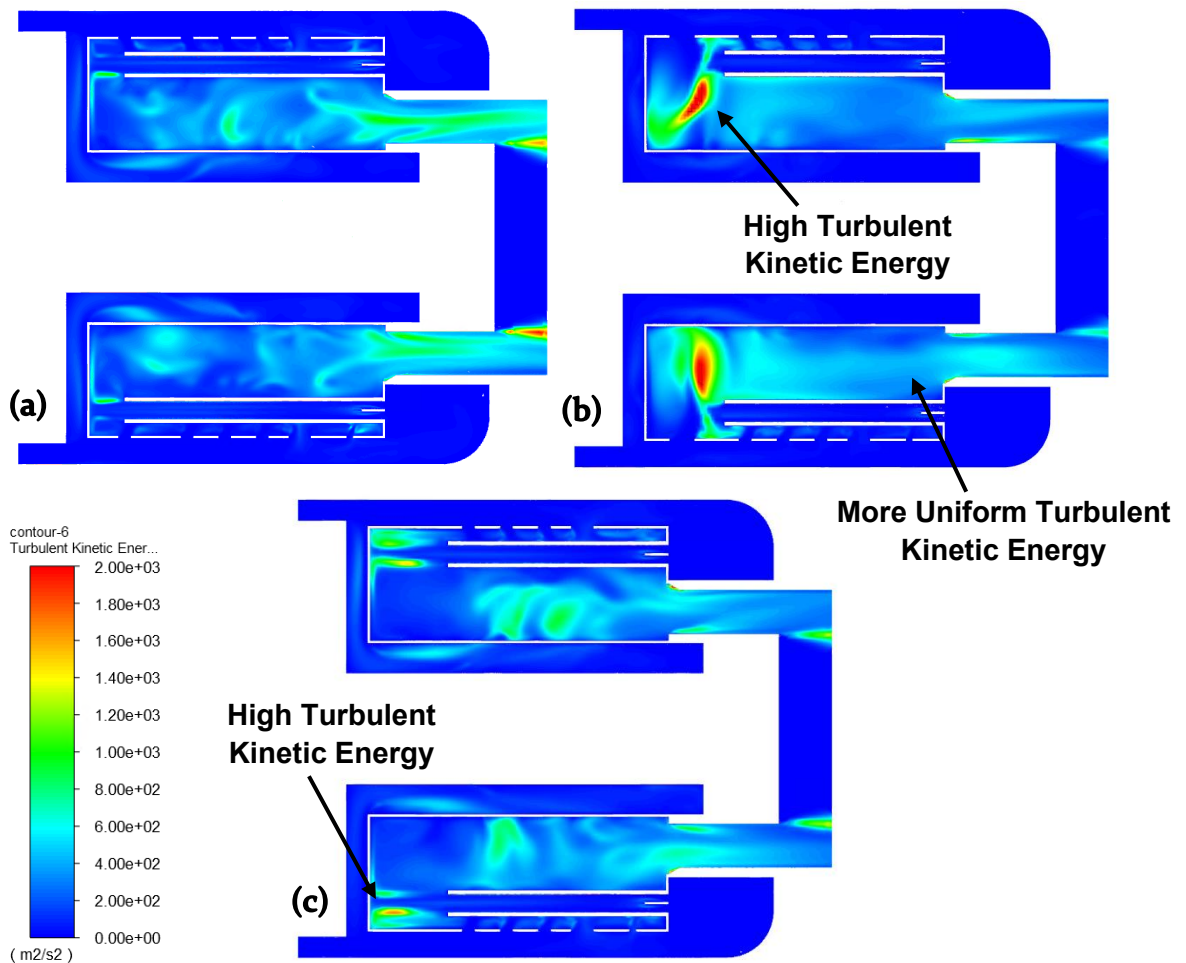


Figure 4-42: Turbulent Kinetic Energy Comparison: (a) baseline model, (b) larger flowpath model, (c) closed flowpath model

The first observation in Figure 4-42 is the increasing turbulent kinetic energy as we changes were made to the models. The open Flowpath model has an increased turbulent kinetic energy while the closed Flowpath model has an even further increased turbulent kinetic energy on average.

The distribution of turbulent kinetic energy in each model becomes apparent when looking at the contours. The baseline model (a) with the lowest turbulent kinetic energy has its highest concentration towards the outlet of the combustion chamber. The flow is relatively stable throughout the rest of the combustion chamber but becomes more turbulent later. The open Flowpath model has a high concentration of turbulent kinetic energy towards the front of the combustion chamber. This makes sense due to the increased amount of flow and the interference of flow between the perforated holes and vaporizing tubes. What is interesting about this model is the fact that the turbulent kinetic energy appears to be more stable towards the outlet of the combustion chamber. The closed Flowpath model with the highest turbulent kinetic energy appears to be much more distributed. There is more turbulence across the model without any single area of extensive turbulent kinetic energy. There is a small concentration towards the outlet of the vaporizing tubes.

The distribution is also apparent when looking at a front cross section of the engine in Figure 4-43. As this is a cross section of the center of the combustion chamber. The baseline model (a) has a moderate amount of turbulent kinetic energy in the center of the engine while the open Flowpath model (b) has much less. This is to be expected from the previous contours with the heavy concentration of turbulent kinetic energy towards the front of the combustion chamber and much less towards the rear. Finally, the closed Flowpath model (c) has the most turbulent kinetic energy in this cross section due to its very distributed and higher average turbulent kinetic energy.

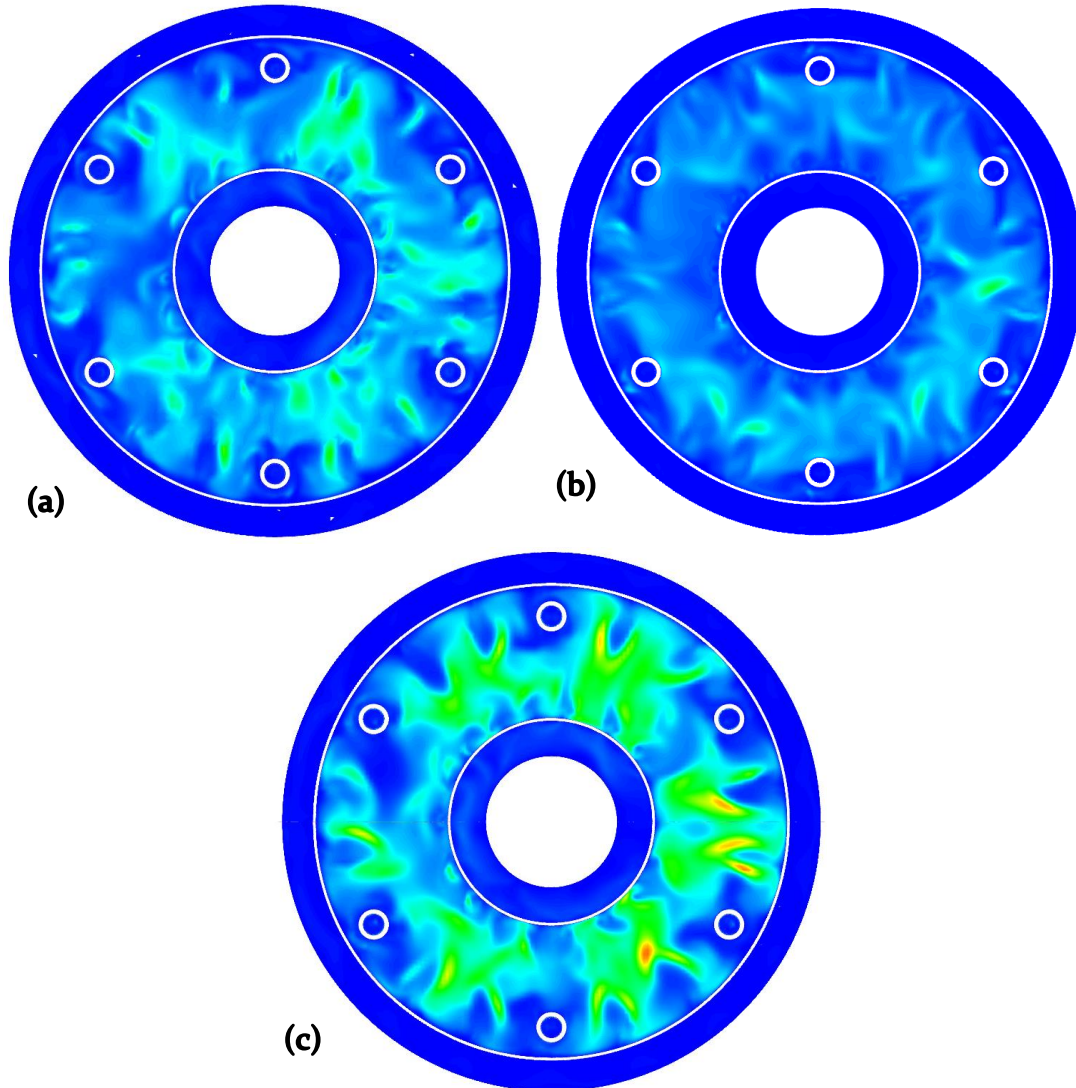


Figure 4-43: Turbulent Kinetic Energy Comparison Front View: (a) baseline model, (b) larger flowpath model, (c) closed flowpath model

#### 4.4. Model Comparison – Overview & Analytical Results

This section is focused on the collection of data from the CFD models previously shown. General comments of overall data, comparison to experimental values, and calculation of the combustion efficiency of each model are to follow.

##### **Comments on Overall Data**

The geometric changes in the closed flowpath model allowed for a higher max velocity due to the closing of the first set of combustion chamber holes, but this was

limited to the inlet area outside of the combustion chamber. Because of this the overall average velocity in the fluid domain was lower. This is also seen in the maximum pressure values of the models where the high pressure in the areas outside of the combustion chamber for the closed flowpath model occurred. Because of this high pressure in the outside areas, the model also saw the largest pressure drop which is not ideal for the turbine engine performance.

The temperature of the combustion chamber solid region is of note as this seems to increase steadily as the turbulent kinetic energy of the models also increases. This is likely a result of redirecting flow early on into the inner combustion chamber which enhanced the mixing in the outer combustion chamber. The higher turbulent kinetic energy from the enhanced mixing generates higher heat transfer and can cause higher temperatures in the material of the turbine engine. Looking at the same location, it is extremely interesting that the overall average temperature of the closed flowpath model (c) was higher but had a lower max vertex temperature and higher minimum vertex temperature. This indicates that the temperature of the combustion chamber walls is more spread out instead of localized. The wall temperatures for the other models had a lower average but had an area of very high concentrated heat.

The temperature at the turbine inlet between the models on average remains consistent, remaining around 640K. When considering the maximum temperature at the same location, the modified geometries appear to produce a hot spot somewhere on the turbine inlet. The produced hot spots are of concern but the average temperatures remaining steady imply that the high temperature is not in a large area.

### **Comparison to Experimental Data**

Comparison between the models and the experimental data will allow some insight into the overall accuracy of the data being presented. Thanks to the initial experimental run, in addition to the work done by previous students to collect data on the TJT-3000 (Campbell, Latimer, & Scholes, 2006) comparison of the temperatures throughout the combustion chamber can be considered. Tables Table 4-5 & Table 4-6 show the engine characteristics and experimental results of the engine at “new make” condition. This data was previously displayed in Table 1-1 and Table 1-2 but is placed here for ease of comparison with additional data from the baseline model.

Table 4-5: TJT-3000 Engine Characteristics

Engine Characteristics	
Maximum Thrust	12.5 kg
Maximum Sustainable Shaft Speed	126,000 RPM
Idle Shaft Speed	33,000 RPM
Max EGT	640°C
Fuel	Kerosene, Jet A1
Fuel Consumption	0.35 (L/min)
Weight	1.65 Kg

Table 4-6: New Make Experimental Results vs Baseline Model

Experimental Results					
Datum	Experiment	Base Model (Outlet Max)	Base Model (Outlet Average)	Base Model (Overall Max)	Base Model (Overall Average)
Exhaust Temperature	904.8 K	x	x	x	x
Compressor Temperature	375.7 K	300 K	300K	300K	300K
Combustion Temperature	1541.9471 K	1430.397	639.9K	2281.42K	868.8K

The primary point of comparison between the experimental data and the CFD models is the combustion temperature. The location of the specified “combustion temperature” heavily skews the temperature data. During the experiment the thermocouple displaying the combustion temperature was placed within the combustion chamber directly in front of the turbine inlet which is to be compared to the CFD data for the outlet of the model. With the base model, the outlet temperatures were calculated to be a maximum of 1430.397K which is 111K below the experimental data. This reduction in temperature is likely due to the turbulent nature of the combustion process. The vertex maximum temperature across the engine model fluid domain was calculated as 2281.419K. This high temperature is an isolated hot spot, but this variation describes how a slight change in thermocouple location or data collection can contribute to temperature variations.



## Data Analysis

Using the collected values, the combustion efficiency is calculated between each model shown in Table 4-7. The combustion efficiency will show the amount of heat being released compared to the amount of fuel being burned within the chamber. The combustion efficiency will be calculated using Equation 4-3. In this equation  $\eta_b$  is the combustion efficiency,  $\dot{m}$  is the mass flow rate of the system, which is 65x the mass flow rate of the fuel based off of the previously used fully coupled KJ-66 simulation (Wang, et al., 2020).  $\dot{m}_f$  is the mass flow rate of the fuel into the system calculated by converting half the maximum flow rate possible for the pump used in running the TJT-3000 (0.35L/m).  $c_{pg}T_{04}$  is the enthalpy of the outlet conditions based off the specific heat (The Engineering ToolBox, 2004) and temperature at the outlet of the combustion chamber from CFD calculations. While  $c_{pa}T_{03}$  is the enthalpy at the inlet of the combustion chamber.  $\dot{Q}_f$  is the higher heating value of the fuel (The Engineering ToolBox, 2003), which in this case is kerosene.

$$\eta_b = \frac{(\dot{m} + \dot{m}_f)c_{pg}T_{04} - \dot{m}c_{pa}T_{03}}{\dot{m}_f\dot{Q}_f}$$

4-1

Table 4-7: Combustion Efficiency

Model Results - Combustion Efficiency				
Datum	Units	Base Model	Larger Flowpath	Closed Flowpath
$T_{04}$	K	639	640.4	643.6
$c_{pg}$	KJ/Kg	1.06564	1.065304	1.064536
$T_{03}$	K	300	300	300
$c_{pa}$	KJ/Kg	1.006	1.006	1.006
$\dot{m}$	Kg/s	0.14	0.14	0.14
$\dot{m}_f$	Kg/s	0.00215	0.00215	0.00215
$\dot{Q}_f$	KJ/Kg	46200	46200	46200
$\eta_b$	N/A	<b>54.91%</b>	<b>55.09%</b>	<b>55.51%</b>

Comparing the results for each model, the combustion efficiency improves for the larger Flowpath model and then improves further with the closed Flowpath model. This result is directly related to the increase of the outlet temperature of the combustion chamber. The closed Flowpath model having the highest combustion

efficiency makes sense when compared to Figure 4-35 and Figure 4-36. The highly stagnant flow at the front of the combustion chamber causing the high concentration of combustion allows for the hot gasses to rest within the combustion chamber for a longer period. This would cause the combustion within the closed Flowpath model to be more complete compared to the other models. This combustion efficiency comes at a cost of likely degradation to the engine, however. As stated when observing the temperature contours, this stagnant flow causes a very large increase in the walls of the combustion chamber to an likely unmanageable degree.

## 5. CONCLUSIONS & COMMENTS

When independently modeling a combustion chamber, the pressure expected within the flow domain is very sensitive to the turbine inlet boundary condition. A fully coupled simulation would alleviate this sensitivity at the cost of an increase in computation time and power.

Increasing the air flow rate into the outer chamber pushes fuel further into the combustion chamber. This causes more of the chamber walls to heat up, but this is to a manageable degree compared to the turbine inlet temperature.

Restricting the amount of flow moving into the outer combustion chamber allowed the combustion to remain stagnant near the front of the chamber. This caused a higher combustion efficiency due to slower flow allowing the combustion to sit longer but also lead to a large increase in the combustion chamber wall temperatures. This increase in temperature would not be manageable due to reduction of material strength at said temperatures.

Modifying the forward side of the combustion chamber to increase flowrate in to the TJT-3000 combustion chamber without also aft side geometry to increase the flow rate to the turbine inlet leads to increased temperatures across the combustion chamber but a lesser pressure drops. This increased temperature and reduced pressure drop would require more robust materials for the TJT-3000 to utilize the improvements.

The temperature of combustion can be increased without effecting the combustion chamber outlet by increasing the amount of cold flow reaching the rear of the combustion chamber via further adjustments to the inner combustion chamber hole location and size. The open Flowpath model showed how important the flow coming from the inner combustion chamber is for proper cooling and increasing this flowrate could improve this effect.

Restricting flow to the inner combustion chamber and focusing flow to the outer combustion chamber of the TJT-3000 can reduce uniformity of the outlet velocity, causing a higher velocity on the perimeter of the outlet. This increased velocity could warrant further investigation when observed at the tip of the turbine blades for a potentially improved engine efficiency.

The pressure drop in the combustion chamber was related to the restriction of flow through the combustion chamber. The opening of the first set of perforated holes reduced the pressure drop, while closing the perforated holes increased the pressure drop.

A handheld scanner with a resolution of the 0.100 mm is viable to model the components of a micro turbine engine but not ideal. A finer resolution scanner would avoid a substantial amount of the in between modeling steps required to smooth the geometry in this project.

When modeling the fuel inlet of the combustion chamber as a gas instead of a liquid, care must be taken to appropriately expand the surface area of the inlet during the modeling process to avoid excessive speeds at the inlet due to the decreased density of the injected fuel.

Geometric changes to the shroud flow domain to allow less stagnant flow would lead to a lesser pressure drop across the combustion chamber. The most apparent high-pressure zone after the improvements from the open Flowpath model was the shroud Flowpath area when flow was being redirected through the vaporizing tubes. Improving the flow in this area would benefit the engine.

### **Future Work**

The analysis done here is only a part of what can be done to observe the thermodynamic cycle of the TJT-3000 turbine engine. As the CFD analysis of the TJT-3000 done here was only done for the combustion chamber. Future analysis could include the turbine in order to see if the increased velocity at the perimeter of the outlet is beneficial to the engine efficiency. A similar analysis could be done for the compressor of the engine which could result in movement towards a fully coupled CFD model of the TJT-3000 using all the scanned components.

In addition, gathering additional scans of the micro turbine engine using new hardware that can scan to a finer resolution would greatly improve the accuracy of the CAD modeled engine. A recent addition on campus includes a computer tomograph (CT) of which can be used to get scans of the TJT-3000 with a resolution of 0.01mm instead of the 0.1mm from the HandySCAN 300. This would allow for faster integration in to the CFD modeling phase.

A more robust combustion calculation can be done using more available species in the non-premixed combustion model. This can come in the form of more reaction species or in more accurate combustion of the fuel and oxid mixture. The mixture used in this simulation had only utilized the nitrogen and oxygen as the major components of air, future calculations could add the minor components as well.

## REFERENCES

- Aminov, R. Z. (2018). Optimal gas turbine inlet temperature for cyclic operation. *Journal of Physics: Conference Series*. Retrieved from <https://iopscience.iop.org/article/10.1088/1742-6596/1111/1/012046/pdf>
- ANSYS. (2009). *26.1 Overview of Using the Solver*. Retrieved from ANSYS FLUENT: <https://www.afs.enea.it/project/neptunius/docs/fluent/html/ug/node776.htm>
- ANSYS Fluent. (2006, December). *Modeling Turbulent Flows*. Retrieved from [www.fluentusers.com](http://www.fluentusers.com).
- Benson, T., & Shaw, R. J. (2021, May 13). *How does a jet engine work?* Retrieved from [nasa.gov: https://www.grc.nasa.gov/WWW/K-12/UEET/StudentSite/engines.html](https://www.grc.nasa.gov/WWW/K-12/UEET/StudentSite/engines.html)
- Boukhanouf, R. (2011). *Micro Gas Turbine*. Retrieved from [sciencedirect.com: https://www.sciencedirect.com/topics/engineering/micro-gas-turbine](https://www.sciencedirect.com/topics/engineering/micro-gas-turbine)
- Campbell, M., Latimer, E., & Scholes, J. (2006, April 19). Mini Gas Turbine. Youngstown, Ohio, United States.
- Capehart, B. L. (2016, 12 22). *Microturbines*. Retrieved from WBDG: <https://www.wbdg.org/resources/microturbines>
- CFD-Online. (2014, March 28). *CFD Online*. Retrieved from [cfid-online: https://www.cfd-online.com/Wiki/Dimensionless\\_wall\\_distance\\_\(y\\_plus\)](https://www.cfd-online.com/Wiki/Dimensionless_wall_distance_(y_plus))
- Chauhan, S., & Wessley, G. J. (2019). Thermodynamic Performance Analysis of a Micro Turbojet Engine for UAV and Drone Propulsion. *International Journal of Recent Technology and Engineering (IJRTE)*, 1-6.
- Chiesa, P., Consonni, S., Lozza, G., & Macchi, E. (2015, February 25). *ASME Digital Collection*. Retrieved from ASME Digital Collection: <https://asmedigitalcollection.asme.org/GT/proceedings/GT1993/78903/V03AT15A074/236260>
- Collins. (2020, February 13). *Turbine Engine*. Retrieved from Collins Dictionary: <https://www.collinsdictionary.com/us/dictionary/english/turbine-engine>
- CREAFORM. (2021). *Metrology Solutions*. Retrieved from [creaform3d.com: https://www.creaform3d.com/sites/default/files/assets/brochures/files/handyscan3d\\_brochure\\_en\\_hq\\_21032017\\_2.pdf](https://www.creaform3d.com/sites/default/files/assets/brochures/files/handyscan3d_brochure_en_hq_21032017_2.pdf)

- Gangaraju, S. S., & Krishna, M. M. (2014, November). *CFD Analysis of Non-premixed combustion in cannular combustion chamber at Gas turbine operating conditions*. Retrieved from Research Gate: [https://www.researchgate.net/publication/269462927\\_CFD\\_analysis\\_of\\_Non-premixed\\_combustion\\_in\\_cannular\\_combustion\\_chamber\\_at\\_Gas\\_turbine\\_operating\\_conditions](https://www.researchgate.net/publication/269462927_CFD_analysis_of_Non-premixed_combustion_in_cannular_combustion_chamber_at_Gas_turbine_operating_conditions)
- Habibi, I. F. (2019). *Optimization of an Annular Combustion Chamber for Micro Turbo Jet System*. Retrieved from IOP Conference Series: Materials Science and Engineering: <https://iopscience.iop.org/article/10.1088/1757-899X/645/1/012009/pdf>
- Hall, N. (2021, May 13). *Ideal Brayton Cycle*. Retrieved from nasa.gov: <https://www.grc.nasa.gov/WWW/K-12/airplane/brayton.html>
- He, W., Guo, Z., Xu, S., & Jin, Y. (2021). Numerical and Experimental Investigations on Performance Optimization of Microturbojet Engine Combustor. *International Journal of Aerospace Engineering*. Retrieved from <https://www.hindawi.com/journals/ijae/2021/6616537/#B8>
- Krampf, F. M. (1992). A Practical Guide for Gas Turbine Performance Field and Test Data Analysis. *The American Society of Mechanical Engineers*. Retrieved from [https://watermark.silverchair.com/v003t07a016-92-gt-427.pdf?token=AQECAHi208BE49Ooan9kKhW\\_Ercy7Dm3ZL\\_9Cf3qfKAc485ysgAABCYwggQiBgkqhkiG9w0BBwagggQTMIIEDwIBADCCBAgGCSqGS Ib3DQEHATAeBgIghkgBZQMEAS4wEQQMw2VTItNwDcLzFZ-NAgEQgIID2SXIpgGUNwc7R-8ydcv5-J9YaoyeSIdej](https://watermark.silverchair.com/v003t07a016-92-gt-427.pdf?token=AQECAHi208BE49Ooan9kKhW_Ercy7Dm3ZL_9Cf3qfKAc485ysgAABCYwggQiBgkqhkiG9w0BBwagggQTMIIEDwIBADCCBAgGCSqGS Ib3DQEHATAeBgIghkgBZQMEAS4wEQQMw2VTItNwDcLzFZ-NAgEQgIID2SXIpgGUNwc7R-8ydcv5-J9YaoyeSIdej)
- Krishnamurthy, R. (2019, March 29). *The Art and Science of Meshing Turbine Blades*. Retrieved from GridPro Blog: <https://blog.gridpro.com/the-art-and-science-of-meshing-turbine-blades/>
- Large, J., & Pesyridis, A. (2019). *Investigation of Micro Gas Turbine Systems for High Speed Long Loiter Tactical Unmanned Air Systems*. Department of Mechanical and Aerospace Engineering, Brunel University London.
- Malalasekera, W., & Versteeg, H. K. (2007). An Introduction to Computational Fluid Dynamics: The Finite Volume Method. *Pearson Education Limited*.
- Malalasekera, W., & Versteeg, K. H. (2007). *An Introduction to Computational Fluid Dynamics*. Harlow: Pearson Prentice Hall. Retrieved from

[http://ftp.demec.ufpr.br/disciplinas/TM702/Versteeg\\_Malalasekera\\_2ed.pdf](http://ftp.demec.ufpr.br/disciplinas/TM702/Versteeg_Malalasekera_2ed.pdf)

NATO. (2021, October 20). *RA 1600 - Remotely Poloted Air Systems*. Retrieved from [https://assets.publishing.service.gov.uk/government/uploads/system/uploads/attachment\\_data/file/948686/RA1600\\_Issue\\_8.pdf](https://assets.publishing.service.gov.uk/government/uploads/system/uploads/attachment_data/file/948686/RA1600_Issue_8.pdf)

Ndeda, R., Motsamai, S. O., & Muiruri, I. P. (2019). A comparative study of RANS-based turbulence models for an upscale wind turbine blade. *Springer Nature Switzerland AG*.

Online, C. (2011, June 11). *Turbulence Kinetic Energy*. Retrieved from CFD Online: [https://www.cfd-online.com/Wiki/Turbulence\\_kinetic\\_energy](https://www.cfd-online.com/Wiki/Turbulence_kinetic_energy)

Rosa, M. A. (2014). *Micro Gas Turbine Engine: A Review*. Retrieved from Intech: [https://cdn.intechopen.com/pdfs/45114/InTech-Micro\\_gas\\_turbine\\_engine\\_a\\_review.pdf](https://cdn.intechopen.com/pdfs/45114/InTech-Micro_gas_turbine_engine_a_review.pdf)

Singh, R., Kumar, D. B., & Kumar, S. (n.d.). Design and CFD Analysis of Gas Turbine Engine Chamber. *International Journal of Science and Research (ISJR)*.

Soares, M. C. (2013). Gas Turbines in Simple Cycle Mode. In M. C. Soares, *Gas Turbines in Simple and Combined Cycle applications*. Netl.

Solmaz, S. (2021, 24 June). Turbulence: Which Model Should I Select for My CFD Analysis? *Simscale*. Retrieved from <https://www.simscale.com/blog/2017/12/turbulence-cfd-analysis/>

The Engineering ToolBox. (2003). *Fuels - Higher and Lower Calorific Values*. Retrieved from The Engineering ToolBox: [https://www.engineeringtoolbox.com/fuels-higher-calorific-values-d\\_169.html](https://www.engineeringtoolbox.com/fuels-higher-calorific-values-d_169.html)

The Engineering ToolBox. (2004). *Air- Specific Heat vs. Temperature at Constant Pressure*. Retrieved from The Engineering ToolBox: [https://www.engineeringtoolbox.com/air-specific-heat-capacity-d\\_705.html](https://www.engineeringtoolbox.com/air-specific-heat-capacity-d_705.html)

The Engineering Toolbox. (2008). *Temperature and Strength of Metals*. Retrieved from The Engineering Toolbox: [https://www.engineeringtoolbox.com/metal-temperature-strength-d\\_1353.html](https://www.engineeringtoolbox.com/metal-temperature-strength-d_1353.html)

- ToolBox, E. (2003). *Air - Composition and Molecular Weight*. Retrieved from engineeringtoolbox: [https://www.engineeringtoolbox.com/air-composition-d\\_212.html](https://www.engineeringtoolbox.com/air-composition-d_212.html)
- Trebunskikh, T. V., Ivanov, A. V., & Dumnov, G. E. (n.d.). FloEFD simulation of micro-turbine engine. Retrieved from [http://www.cadflo.com/fileadmin/user\\_upload/Trebunskikh\\_-\\_FloEFD\\_simulation\\_of\\_micro-turbine\\_engine.pdf](http://www.cadflo.com/fileadmin/user_upload/Trebunskikh_-_FloEFD_simulation_of_micro-turbine_engine.pdf)
- Valigi, M. C., Logozzo, S., & Affatato, S. (2017, May). New Challenges in Tribology: Wear Assessment Using 3D Optical Scanners. *Materials*. Retrieved from [https://www.researchgate.net/publication/317116887\\_New\\_Challenges\\_in\\_Tribology\\_Wear\\_Assessment\\_Using\\_3D\\_Optical\\_Scanners](https://www.researchgate.net/publication/317116887_New_Challenges_in_Tribology_Wear_Assessment_Using_3D_Optical_Scanners)
- Wang, C., Zhang, M., Li, T., Su, N., Yang, J., & Liu, Y. (2020, November 2). *THREE-DIMENSIONAL CFD SIMULATION OF A MICRO TURBOJET ENGINE*. Retrieved from <http://conference.cftn.cn/upload/file/e5a4519dd47846358fa3d10600865a3d.pdf>
- Williams, K. (2016, September 18). AJ/TJT-3000 Minuature Gas Turbine Propulsion System. Perth, australia.
- Zore, K., Parkhi, G., & Varghese, A. J. (2019). *semanticscholar*. Retrieved from Ansys Mosaic Poly-Hexcore Mesh for High-Light Aircraft Configuration: ANSYS-Mosaic-Poly-Hexcore-Mesh-For-High-Lift-Aircraft-Configuration\_AeSI-21st-CFD-Sym-Aug-2019.pdf



## APPENDIX

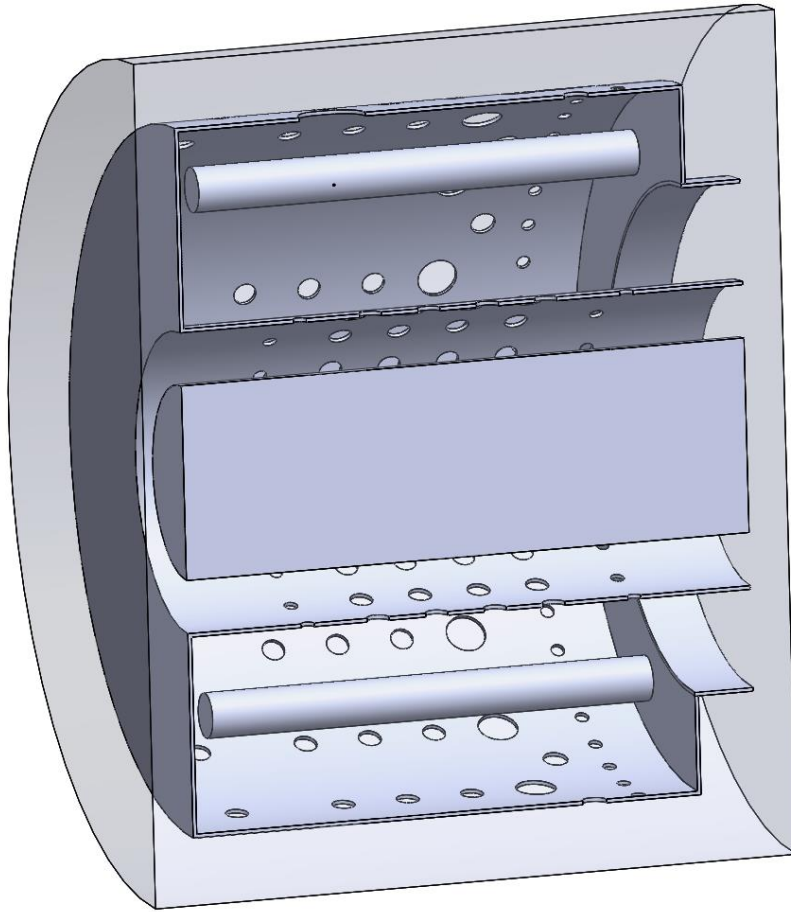


Figure 5-1: Combustion Chamber in Fluid Domain Cavity

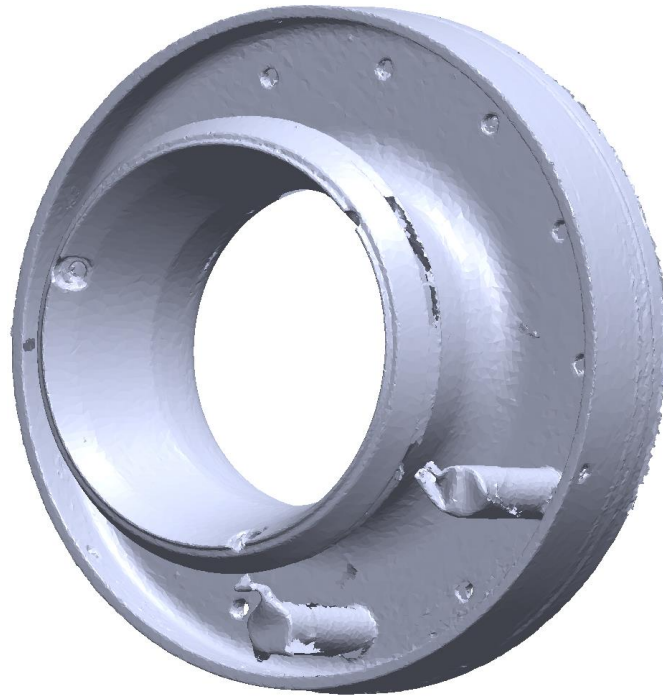


Figure 5-2: Engine Inlet Scan

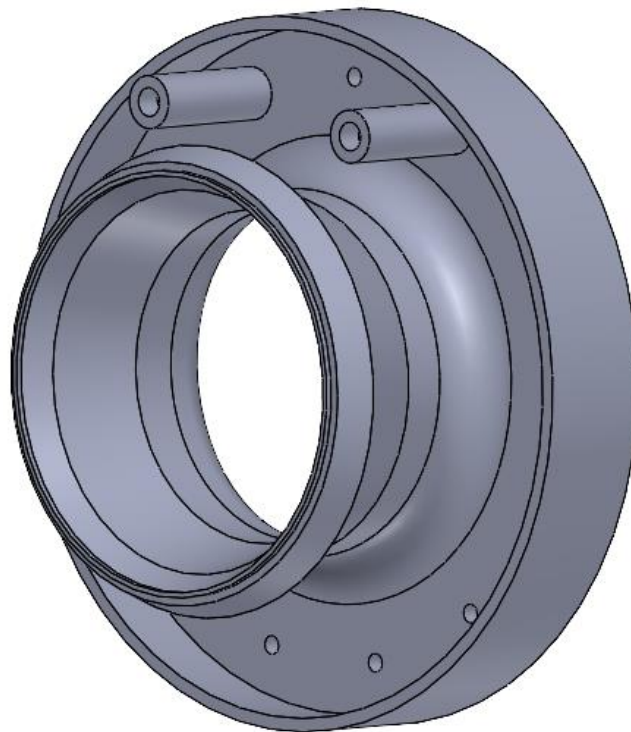


Figure 5-3: Engine Inlet Model



Figure 5-4: Compressor Stator Scan

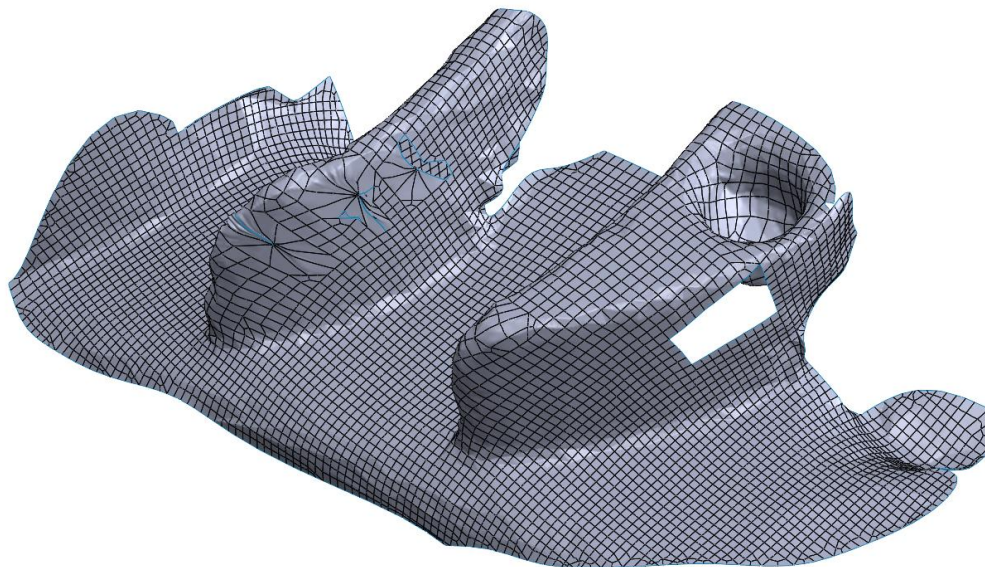


Figure 5-5: Compressor Stator Fins Import

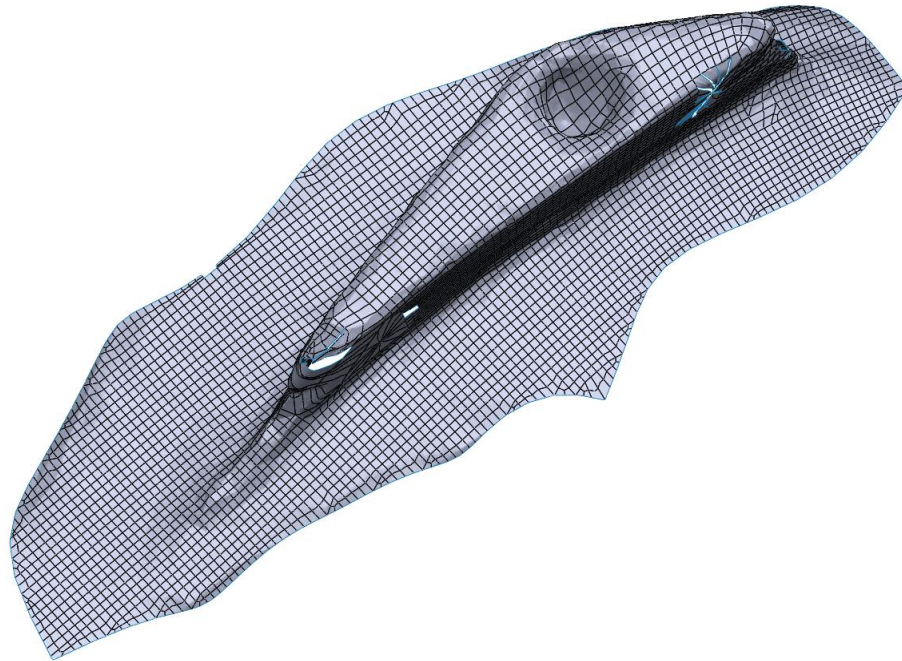


Figure 5-6: Compressor Stator Fin Import

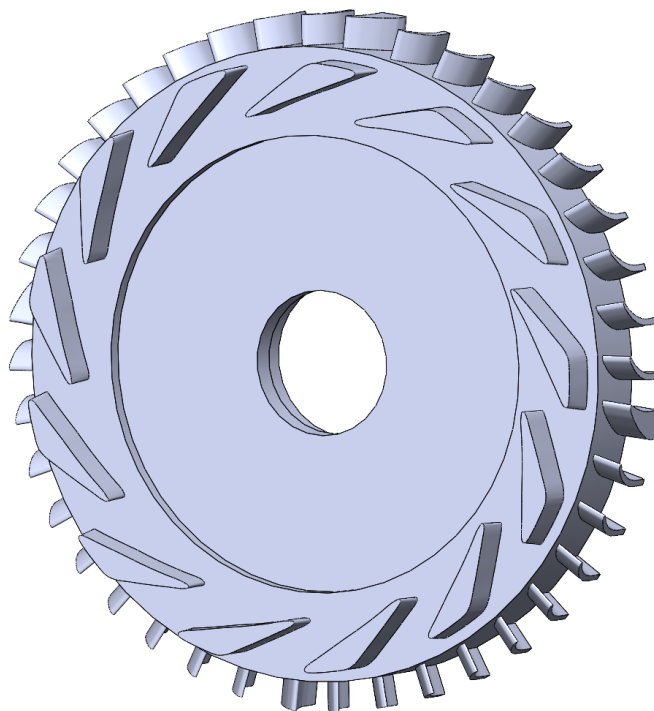


Figure 5-7: Compressor Stator Model



Figure 5-8: Turbine Stator Scan



Figure 5-9: Turbine Stator Fin Import

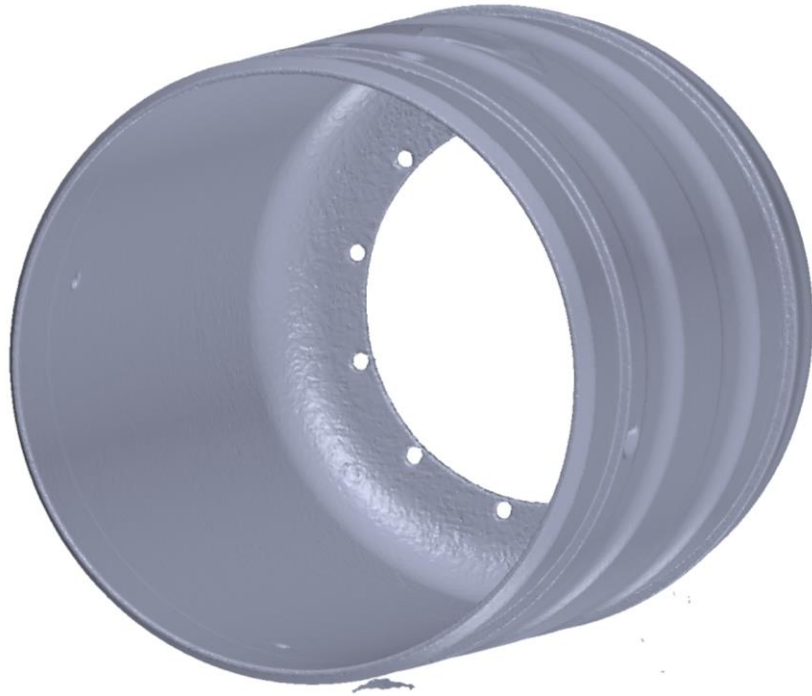


Figure 5-10: Engine Shroud Scan

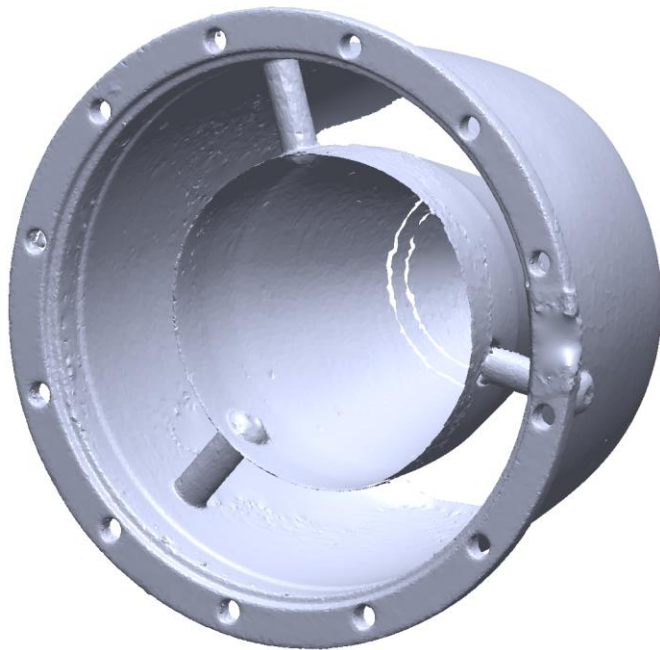


Figure 5-11: Engine Nozzle Scan

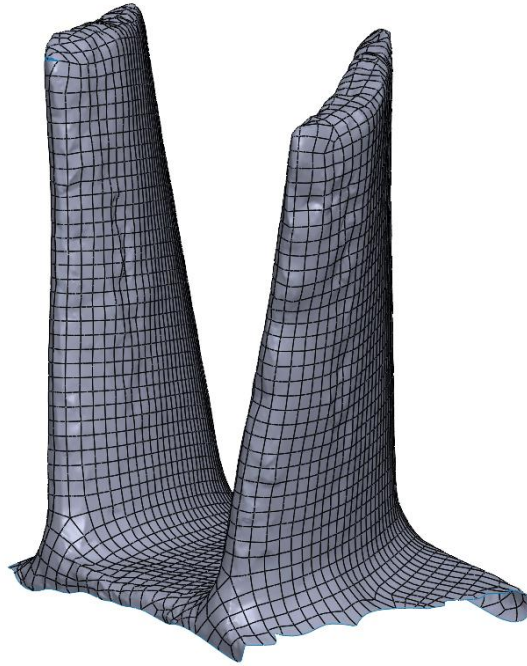


Figure 5-12: Turbine Rotor Blades Import

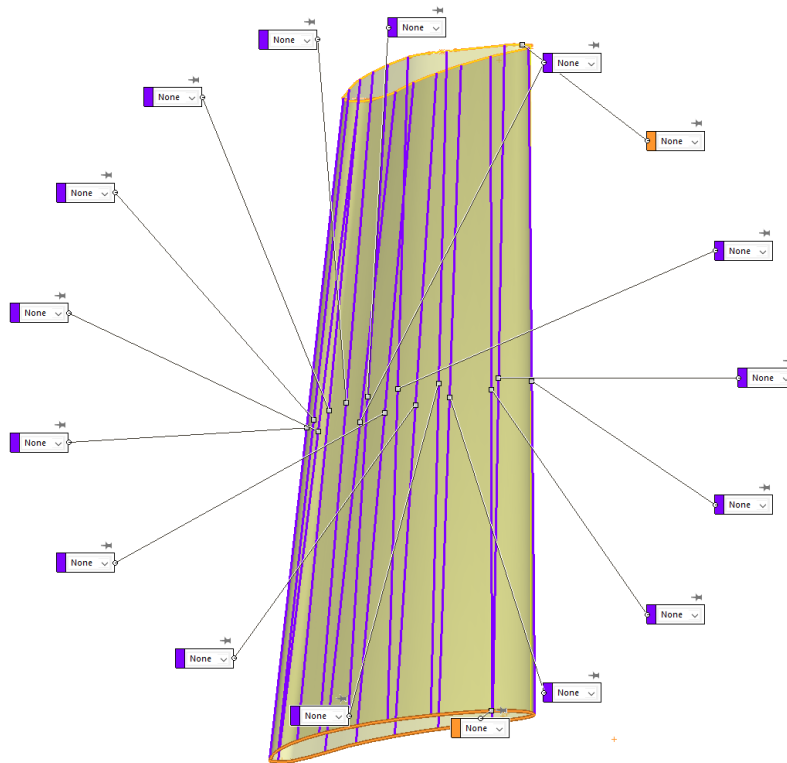


Figure 5-13: Turbine Rotor Blade - SolidWorks Boundary Surface

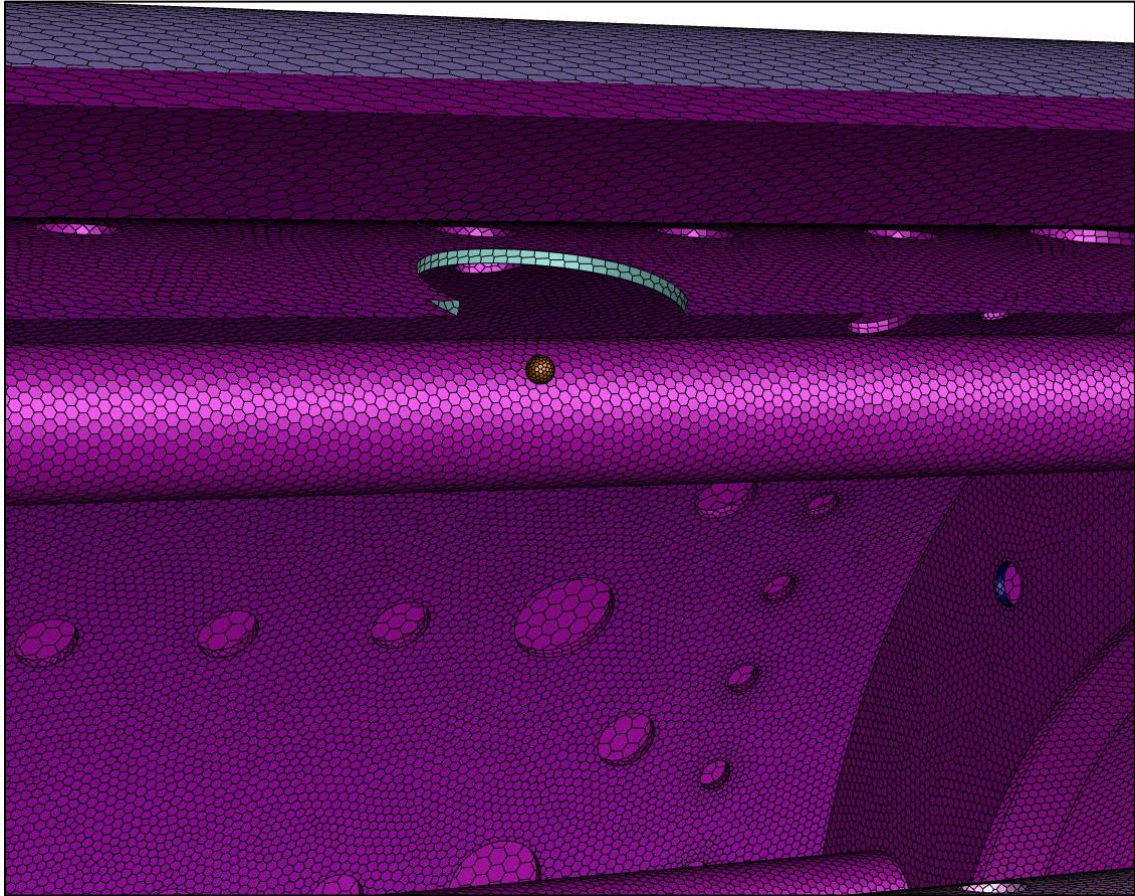


Figure 5-14: Fluent Meshing Spark Domain



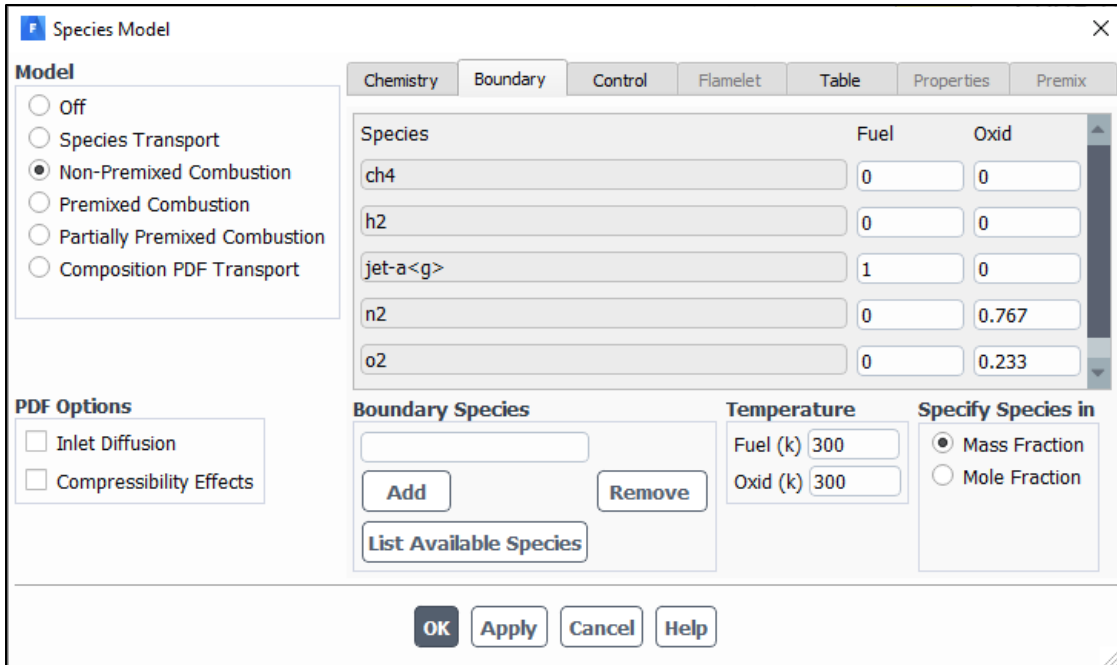


Figure 5-15: Non-Premixed Combustion – Boundary Mass Fraction

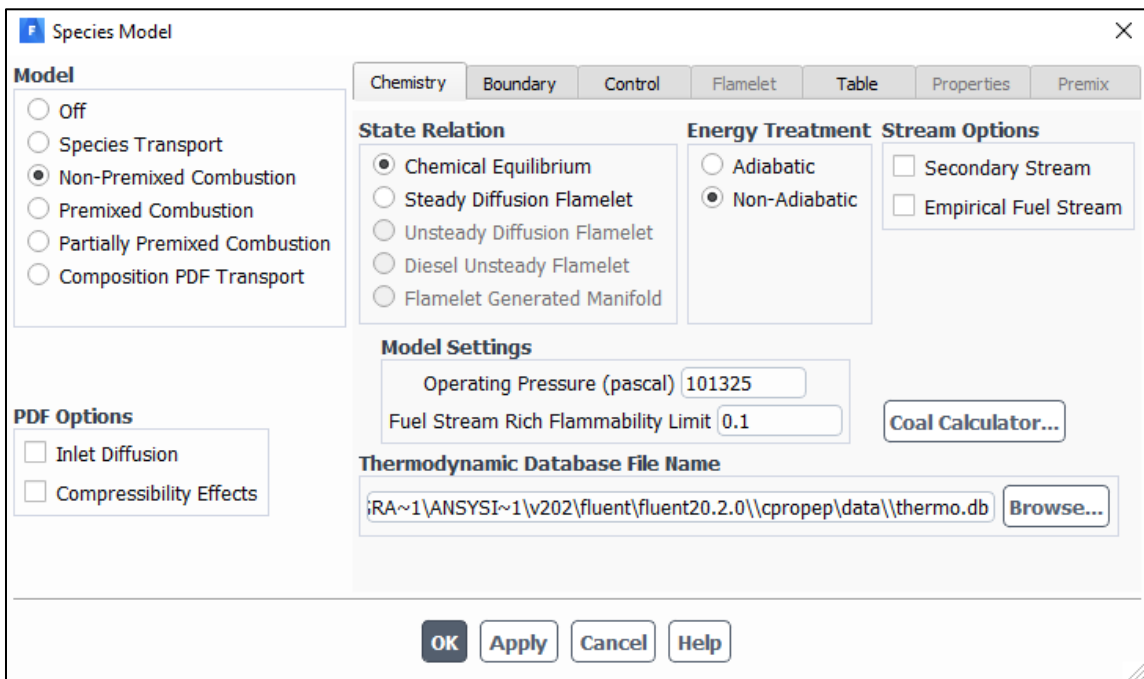


Figure 5-16: Non-Premixed Combustion – Chemistry

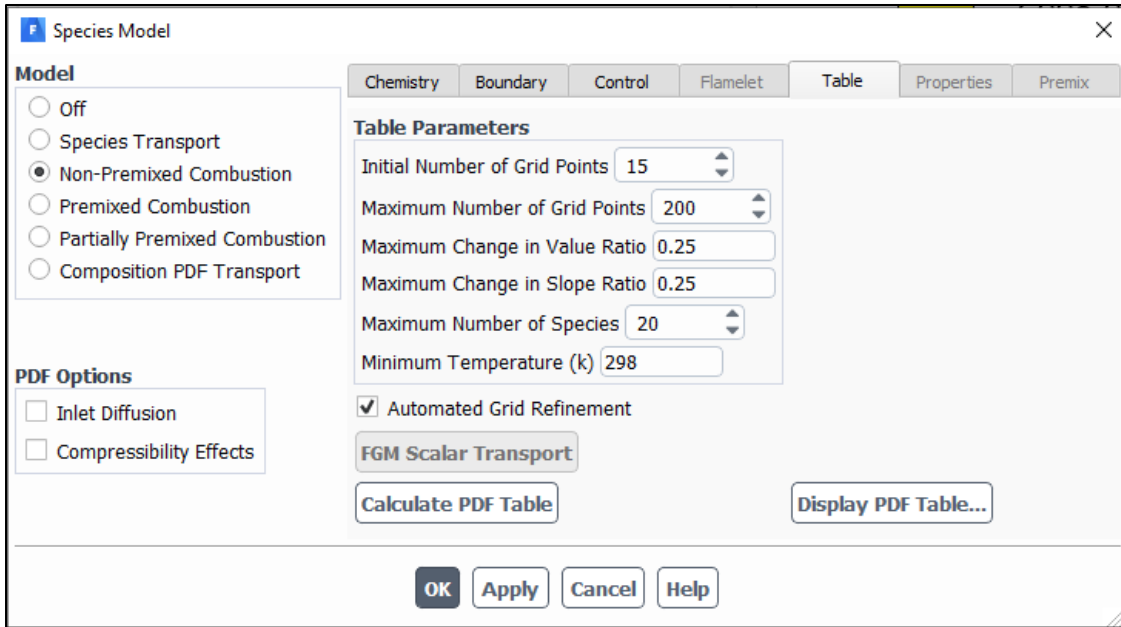


Figure 5-17: Non-Premixed Combustion – Table Parameters

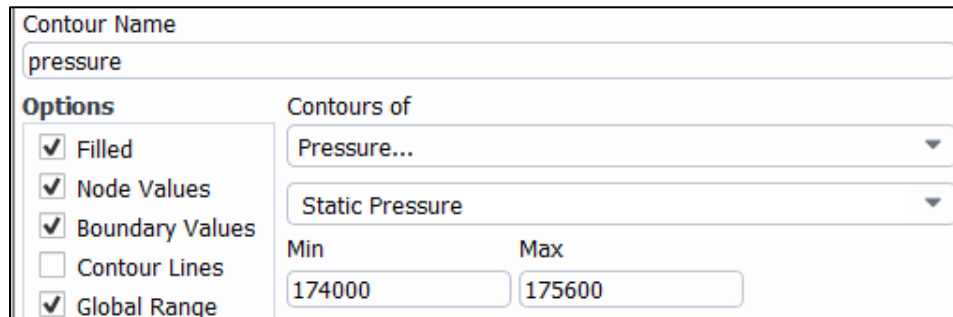


Figure 5-18: Pressure Contour Limits

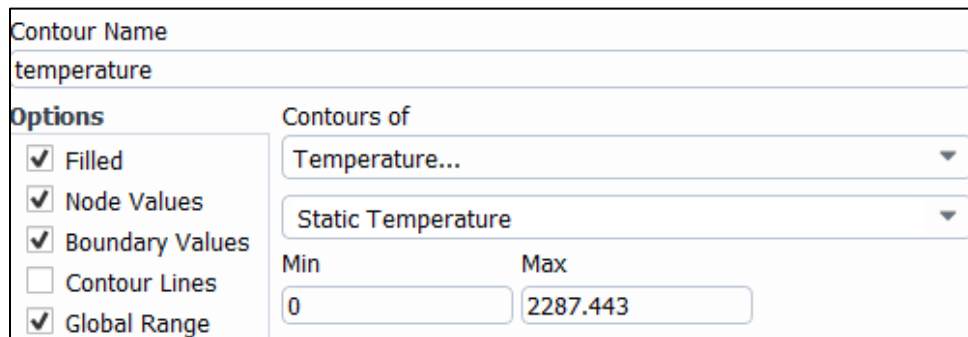


Figure 5-19: Temperature Contour Limits

Contour Name	
velocity	
<b>Options</b>	Contours of
<input checked="" type="checkbox"/> Filled	Velocity...
<input checked="" type="checkbox"/> Node Values	Velocity Magnitude
<input checked="" type="checkbox"/> Boundary Values	Min
<input type="checkbox"/> Contour Lines	Max
<input checked="" type="checkbox"/> Global Range	0
	250

Figure 5-20: Velocity Contour Limits

Viscous Model
✕

**Model**

Inviscid

Laminar

Spalart-Allmaras (1 eqn)

k-epsilon (2 eqn)

k-omega (2 eqn)

Transition k-kl-omega (3 eqn)

Transition SST (4 eqn)

Reynolds Stress (7 eqn)

Scale-Adaptive Simulation (SAS)

Detached Eddy Simulation (DES)

Large Eddy Simulation (LES)

**k-omega Model**

Standard

GEKO

BSL

SST

**k-omega Options**

Low-Re Corrections

**Options**

Viscous Heating

Curvature Correction

Production Kato-Launder

Production Limiter

**Transition Options**

Transition Model none

**Model Constants**

Alpha\*\_inf

Alpha\_inf

Beta\*\_inf

a1

Beta\_i (Inner)

Beta\_i (Outer)

**User-Defined Functions**

Turbulent Viscosity none

**Prandtl and Schmidt Numbers**

Energy Prandtl Number none

Wall Prandtl Number none

Turbulent Schmidt Number none

Figure 5-21: Viscous Model Parameters

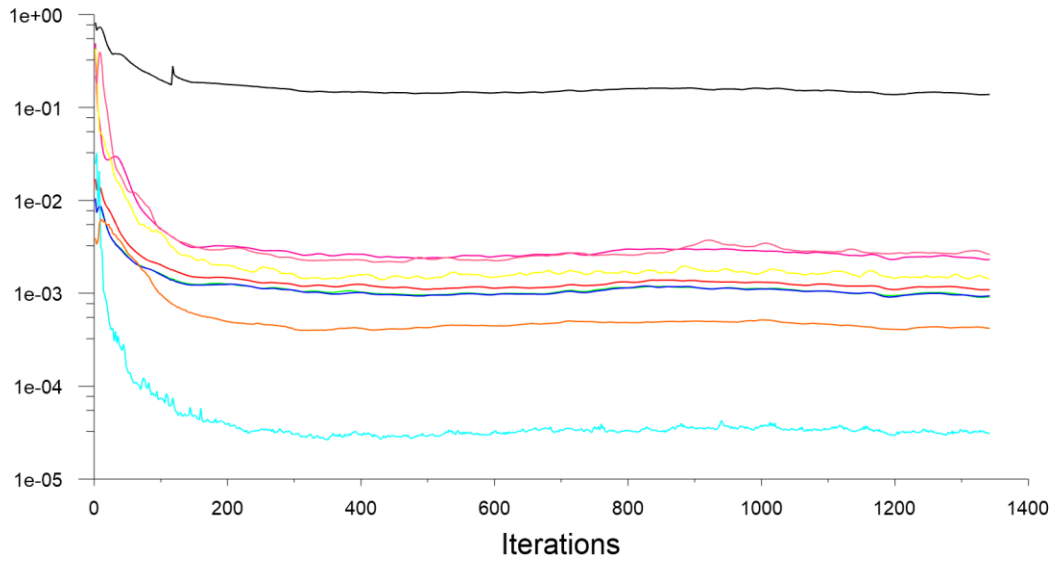


Figure 5-22: Closed Flowpath CFD Model Residuals

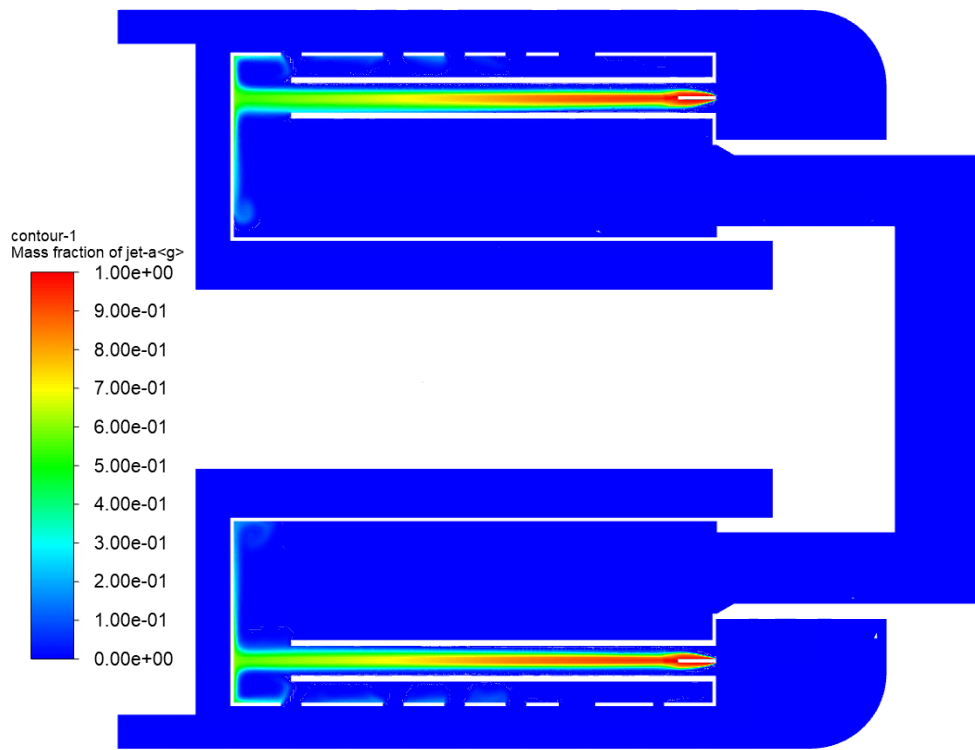


Figure 5-23: Kerosene Fuel Concentration Contour – Baseline Model

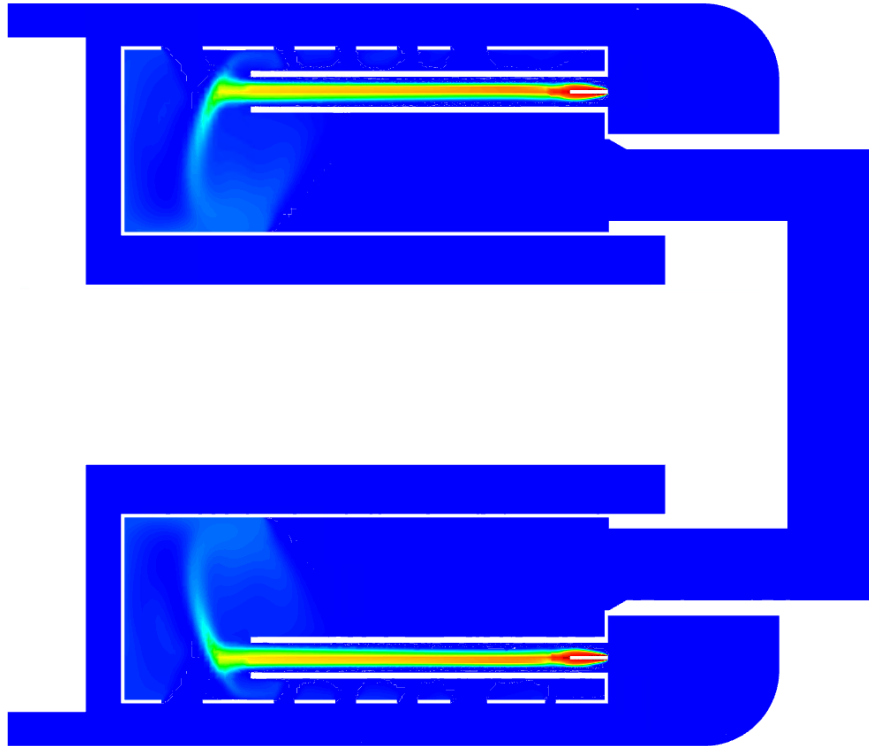


Figure 5-24: Kerosene Fuel Concentration Contour – Open Flowpath Model

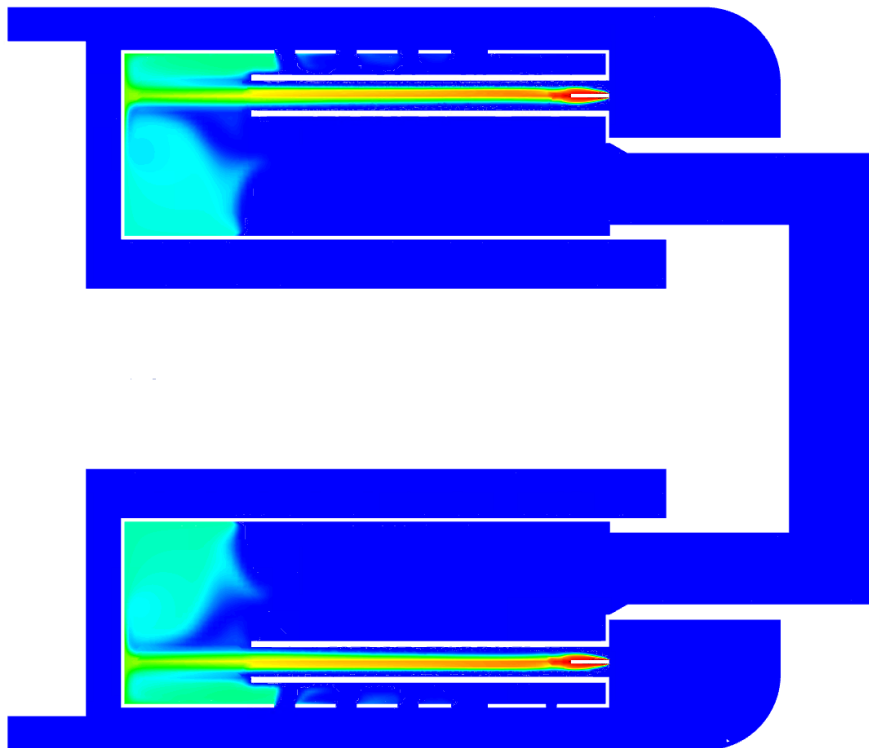


Figure 5-25: Kerosene Fuel Concentration Contour – Closed Flowpath Model

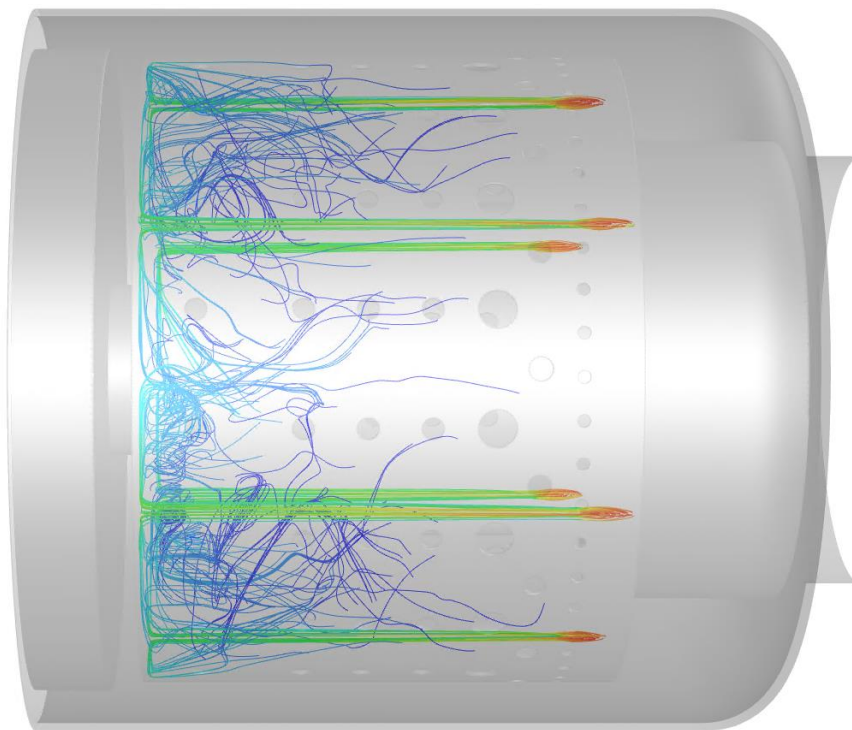


Figure 5-26: Baseline CFD Model Fuel Concentration Pathlines

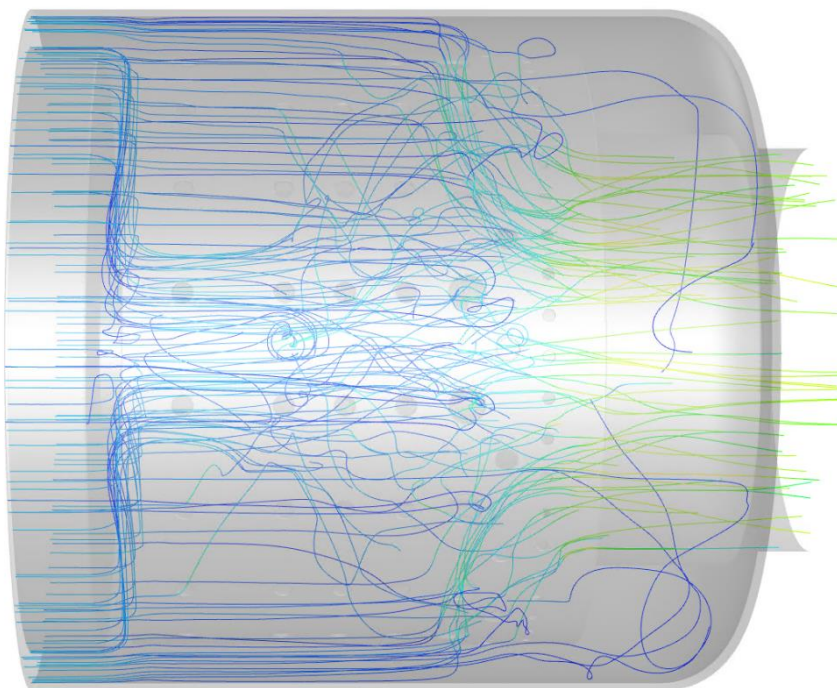


Figure 5-27: Baseline Model Velocity Pathlines

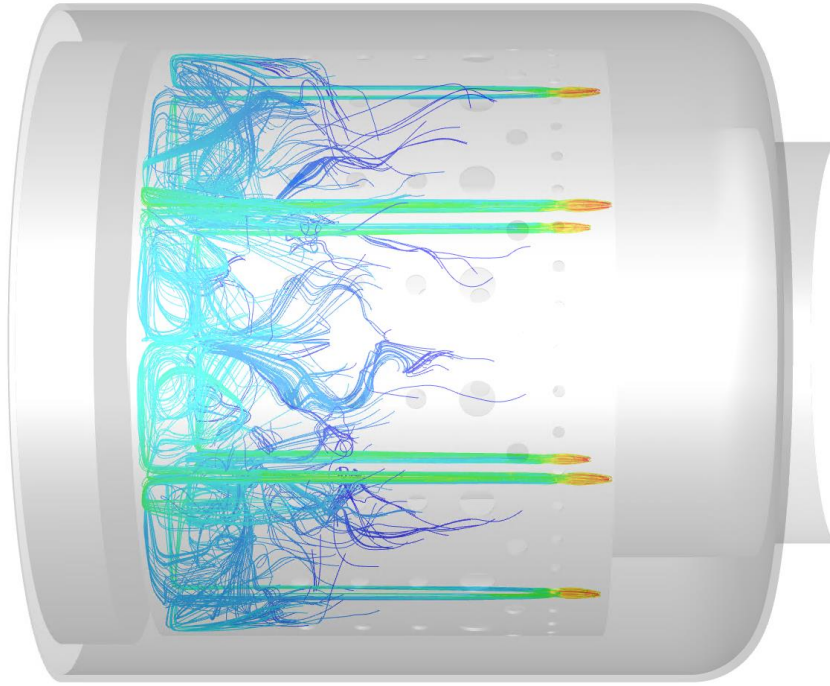


Figure 5-28: Closed Flowpath CFD Model Fuel Concentration Pathlines

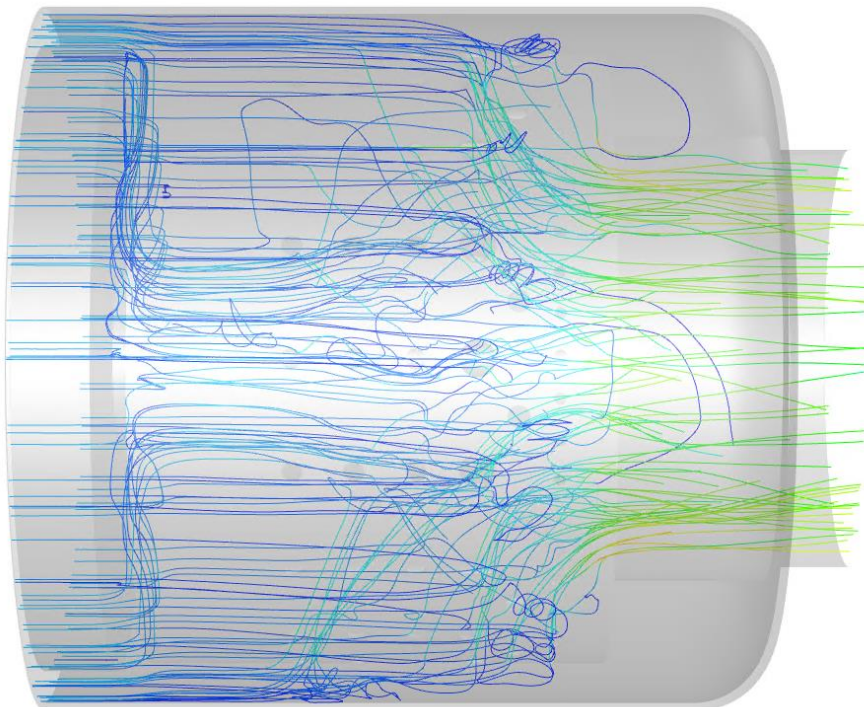


Figure 5-29: Closed Flowpath CFD Model Velocity Pathlines

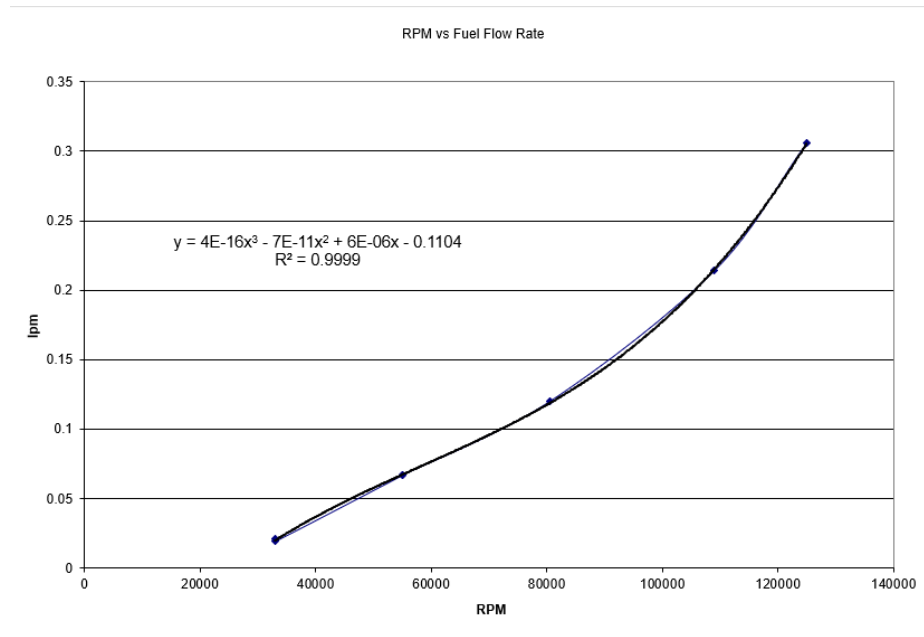


Figure 5-30: RPM vs Fuel Flow Rate - (Campbell, Latimer, & Scholes, 2006)

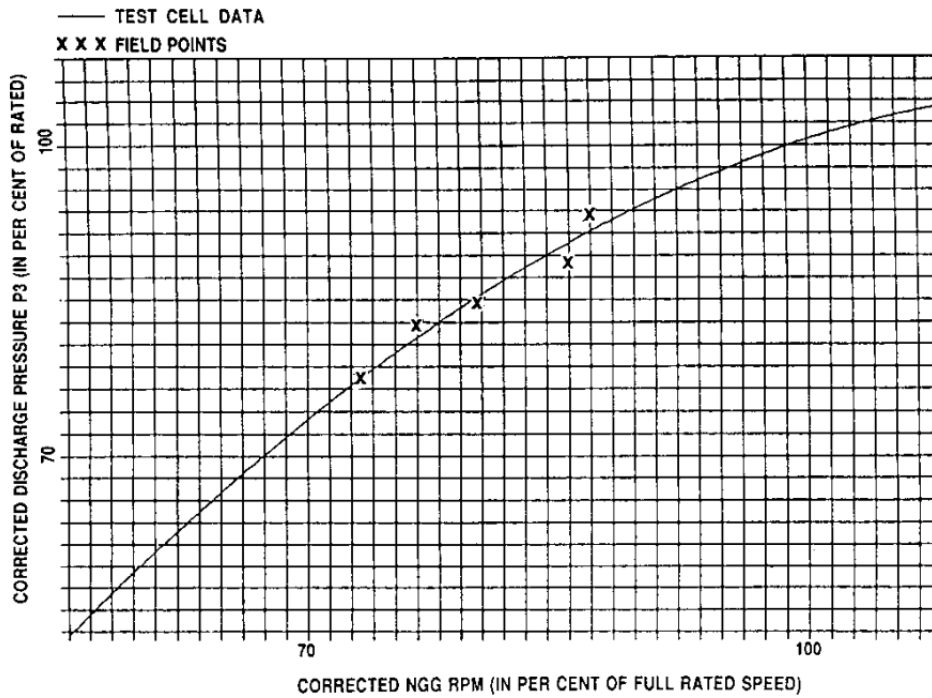


Figure 5-31: Expected Pressure to RPM - (Krampf, 1992)



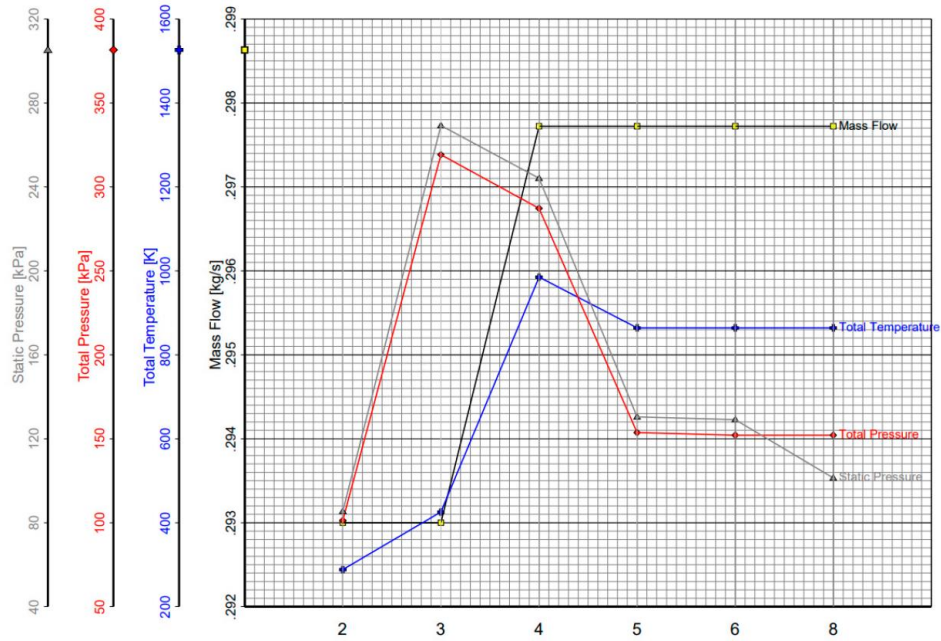


Figure 9. Station properties for the baseline turbojet simulation at 0.13 kN.

Figure 5-32: BMT 120 KS Experimental Run Values - (Large & Pesyridis, 2019)

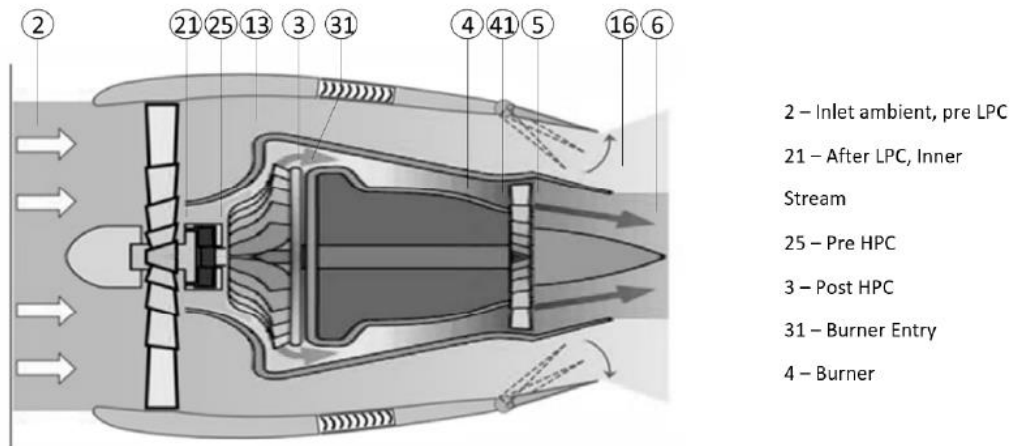


Figure 5-33: BMT 120 KS Data Collection Points - (Large & Pesyridis, 2019)